

Wide-Bandgap Semiconductors: Nanostructures, Defects, and Applications

Guest Editors: Meiyong Liao, Thomas Stergiopoulos, Jose Alvarez,
Surojit Chattopadhyay, and Guihua Zhang





Wide-Bandgap Semiconductors: Nanostructures, Defects, and Applications

Wide-Bandgap Semiconductors: Nanostructures, Defects, and Applications

Guest Editors: Meiyong Liao, Thomas Stergiopoulos,
Jose Alvarez, Surojit Chattopadhyay, and Guihua Zhang



Copyright © 2015 Hindawi Publishing Corporation. All rights reserved.

This is a special issue published in "Journal of Nanomaterials." All articles are open access articles distributed under the Creative Commons Attribution License, which permits unrestricted use, distribution, and reproduction in any medium, provided the original work is properly cited.

Editorial Board

Domenico Acierno, Italy
Katerina Aifantis, USA
Sheikh Akbar, USA
Nageh K. Allam, USA
Margarida Amaral, Portugal
Martin Andersson, Sweden
Raul Arenal, Spain
Ilaria Armentano, Italy
Vincenzo Baglio, Italy
Lavinia Balan, France
Thierry Baron, France
Andrew R. Barron, USA
Reza Bayati, USA
Hongbin Bei, USA
Daniel Bellet, France
Stefano Bellucci, Italy
Enrico Bergamaschi, Italy
Samuel Bernard, France
D. Bhattacharyya, New Zealand
Sergio Bietti, Italy
Giovanni Bongiovanni, Italy
Theodorian Borca-Tasciuc, USA
Mohamed Bououdina, Bahrain
Torsten Brezesinski, Germany
C. Jeffrey Brinker, USA
Christian Brosseau, France
Philippe Caroff, Australia
Victor M. Castaño, Mexico
Albano Cavaleiro, Portugal
Bhanu P. S. Chauhan, USA
Shafiul Chowdhury, USA
Jin-Ho Choy, Korea
Kwang-Leong Choy, UK
Yu-Lun Chueh, Taiwan
Elisabetta Comini, Italy
Giuseppe Compagnini, Italy
David Cornu, France
M. A. Correa-Duarte, Spain
Pantaleo D. Cozzoli, Italy
Shadi A. Dayeh, USA
Luca Deseri, USA
Yong Ding, USA
Philippe Dubois, Belgium
Alain Dufresne, France
Zehra Durmus, Turkey

Joydeep Dutta, Oman
Ali Eftekhari, USA
Jeffrey Elam, USA
Samy El-Shall, USA
Ovidiu Ersen, France
C. Estournès, France
Andrea Falqui, KSA
Matteo Ferroni, Italy
E. Johan Foster, USA
Ilaria Fratoddi, Italy
Wolfgang Fritzsche, Germany
Alan Fuchs, USA
Miguel A. Garcia, Spain
Siddhartha Ghosh, Singapore
P. K. Giri, India
Russell E. Gorga, USA
Jihua Gou, USA
Jean M. Greneche, France
Smrati Gupta, Germany
K. Hamad-Schifferli, USA
S.-P. Hannula, Finland
Michael Harris, USA
Yasuhiko Hayashi, Japan
F. Hernandez-Ramirez, Spain
Michael Z. Hu, USA
Nay Ming Huang, Malaysia
Shaoming Huang, China
David Hui, USA
Zafar Iqbal, USA
Balachandran Jeyadevan, Japan
Xin Jiang, Germany
Rakesh Joshi, Australia
Jeong-won Kang, Korea
Hassan Karimi-Maleh, Iran
Antonios Kelarakis, UK
Alireza Khataee, Iran
Ali Khorsand Zak, Iran
Philippe Knauth, France
Ralph Krupke, Germany
C. Kübel, Germany
Prashant Kumar, UK
Michele Laus, Italy
Eric Le Bourhis, France
Burtrand Lee, USA
Jun Li, Singapore

Meiyong Liao, Japan
Shijun Liao, China
Silvia Licocchia, Italy
Wei Lin, USA
Nathan C. Lindquist, USA
Jun Liu, USA
Z. Lockman, Malaysia
Nico Lovergine, Italy
Jim Low, Australia
Jue Lu, USA
Songwei Lu, USA
Ed Ma, USA
Laura M. Maestro, Spain
Gaurav Mago, USA
Muhamamd A. Malik, UK
Devanesan Mangalaraj, India
Sanjay R. Mathur, Germany
Tony McNally, United Kingdom
Yogendra Mishra, Germany
Paulo Cesar Morais, Brazil
Paul Munroe, Australia
Jae-Min Myoung, Korea
Rajesh R. Naik, USA
Albert Nasibulin, Russia
Toshiaki Natsuki, Japan
Koichi Niihara, Japan
Natalia Noginova, USA
Sherine Obare, USA
Won-Chun Oh, Republic of Korea
Atsuto Okamoto, Japan
Abdelwahab Omri, Canada
Ungyu Paik, Republic of Korea
Piersandro Pallavicini, Italy
Edward A. Payzant, USA
Alessandro Pegoretti, Italy
Ton Peijs, United Kingdom
Oscar Perales-Pérez, Puerto Rico
Jorge Pérez-Juste, Spain
Alexey P. Popov, Finland
Philip D. Rack, USA
Peter Reiss, France
Orlando Rojas, USA
Marco Rossi, Italy
Ilker S. Bayer, Italy
Cengiz S. Ozkan, USA



Sudipta Seal, USA
Shu Seki, Japan
Vladimir Šepelák, Germany
Huaiyu Shao, Japan
Prashant Sharma, USA
Donglu Shi, USA
Bhanu P. Singh, India
Surinder Singh, USA
Vladimir Sivakov, Germany
Ashok Sood, USA
Adolfo Speghini, Italy
Marinella Striccoli, Italy
Xuping Sun, KSA
Ashok K. Sundramoorthy, USA

Angelo Taglietti, Italy
Bo Tan, Canada
Leander Tapfer, Italy
Valeri P. Tolstoy, Russia
Muhammet S. Toprak, Sweden
Ramon Torrecillas, Spain
Achim Trampert, Germany
Takuya Tsuzuki, Australia
Tamer Uyar, Turkey
Bala Vaidhyanathan, UK
Luca Valentini, Italy
Rajender S. Varma, USA
Ester Vazquez, Spain
Antonio Villaverde, Spain

Ajayan Vinu, Australia
Ruibing Wang, Macau
Shiren Wang, USA
Yong Wang, USA
Magnus Willander, Sweden
Ping Xiao, United Kingdom
Zhi Li Xiao, USA
Yangchuan Xing, USA
Doron Yadlovker, Israel
Yoke K. Yap, USA
Kui Yu, Canada
William Yu, USA
Michele Zappalorto, Italy
Renyun Zhang, Sweden

Contents

Wide-Bandgap Semiconductors: Nanostructures, Defects, and Applications, Meiyong Liao, Thomas Stergiopoulos, Jose Alvarez, Surojit Chattopadhyay, and Guihua Zhang
Volume 2015, Article ID 713896, 2 pages

A 3 W High-Voltage Single-Chip Green Light-Emitting Diode with Multiple-Cells Network, W. Wang, Y. Cai, Y. B. Zhang, H. J. Huang, W. Huang, H. O. Li, B. S. Zhang, and H. X. Wang
Volume 2015, Article ID 248191, 4 pages

Density Functional Theory Study on Defect Feature of $\text{As}_{\text{Ga}}\text{Ga}_{\text{As}}$ in Gallium Arsenide, Deming Ma, Xi Chen, Hongbo Qiao, Wei Wang, Wei Shi, and Enling Li
Volume 2015, Article ID 582186, 5 pages

Mechanism and Kinetics Study for Photocatalytic Oxidation Degradation: A Case Study for Phenoxyacetic Acid Organic Pollutant, Kian Mun Lee, Sharifah Bee Abd Hamid, and Chin Wei Lai
Volume 2015, Article ID 940857, 10 pages

A Review on the Low-Dimensional and Hybridized Nanostructured Diamond Films, Hongdong Li, Shaoheng Cheng, Jia Li, and Jie Song
Volume 2015, Article ID 692562, 15 pages

Fabrication and Characterization of Highly Oriented N-Doped ZnO Nanorods by Selective Area Epitaxy, Yang Zhang, Shulin Gu, Kun Tang, Jiandong Ye, Haixiong Ge, Zhengrong Yao, Shunming Zhu, and Youdou Zheng
Volume 2015, Article ID 854074, 9 pages

Enhancement of Two-Dimensional Electron-Gas Properties by Zn Polar ZnMgO/MgO/ZnO Structure Grown by Radical-Source Laser Molecular Beam Epitaxy, Li Meng, Jingwen Zhang, Qun Li, and Xun Hou
Volume 2015, Article ID 694234, 7 pages

Mobility Limitations due to Dislocations and Interface Roughness in AlGaN/AlN/GaN Heterostructure, Qun Li, Jingwen Zhang, Li Meng, Jing Chong, and Xun Hou
Volume 2015, Article ID 903098, 6 pages

Gallium Nitride Electrical Characteristics Extraction and Uniformity Sorting, Shyr-Long Jeng, Chih-Chiang Wu, and Wei-Hua Chieng
Volume 2015, Article ID 478375, 15 pages

Diamond Based Field-Effect Transistors of Zr Gate with SiN_x Dielectric Layers, W. Wang, C. Hu, S. Y. Li, F. N. Li, Z. C. Liu, F. Wang, J. Fu, and H. X. Wang
Volume 2015, Article ID 124640, 5 pages

Editorial

Wide-Bandgap Semiconductors: Nanostructures, Defects, and Applications

**Meiyong Liao,¹ Thomas Stergiopoulos,² Jose Alvarez,³
Surojit Chattopadhyay,⁴ and Guihua Zhang⁵**

¹*Optical and Electronic Materials Unit, National Institute for Materials Science, Namiki 1-1, Tsukuba, Ibaraki 3050044, Japan*

²*Department of Physics, University of Oxford, Clarendon Laboratory, Parks Road, Oxford OX13PU, UK*

³*Laboratoire de Genie Electrique de Paris (LGEP), CNRS UMR 8507, Supelec, Université Paris-Sud, Université Paris 6, 11 rue Joliot Curie, Plateau de Moulon, 91192 Gif-sur-Yvette, France*

⁴*Institute of Biophotonics, National Yang-Ming University, No. 155, Section 2, Li-Nong Street, Taipei 112, Taiwan*

⁵*Research Institute of Science for Safety and Sustainability, National Institute of Advanced Industrial Science and Technology (AIST), Onogawa 16-1, Tsukuba, Ibaraki 3058569, Japan*

Correspondence should be addressed to Meiyong Liao; meiyong.liao@nims.go.jp

Received 6 August 2015; Accepted 6 August 2015

Copyright © 2015 Meiyong Liao et al. This is an open access article distributed under the Creative Commons Attribution License, which permits unrestricted use, distribution, and reproduction in any medium, provided the original work is properly cited.

Nanostructured wide-bandgap semiconductors (NWS), such as III-nitrides, SiC, ZnO, TiO₂, diamond, AlN, and BN, have attracted intensive research attention owing to prospective applications in solid-state lighting, solar cells, power electronics, sensors, spintronics, and MEMS/NEMS. These nanostructured semiconductors exhibit tremendous advantages in terms of power capability, energy conversion efficiency, optical properties, radiation strength, high temperature, and frequency operation. Although great progress has been achieved in the synthesis of the NWS materials and promising device applications have been demonstrated since the new century, much further research in the crystallinity improvement, electronic structure control, impurities doping, and devices design need to be carried out. The growth dynamics and the defect physics of NWS should be better understood to push forward their potential applications.

This special issue is focused on recent research progress in wide-bandgap semiconductors materials including novel growth strategies of NWS materials, the electronic structure tailoring for functionalization, novel devices concepts, devices physics, and applications in various fields.

By using first-principles calculations based on the density functional theory, D. Ma et al. investigated the defects in gallium arsenide. A deep donor level of 0.85 eV below the

conduction band minimum on the gallium arsenide crystal surface was disclosed, while the lowest donor level of the defect inside the gallium arsenide bulk was 0.83 eV. The calculations also predicted that the formation energies of internal and surface defects were around 2.36 eV and 5.54 eV, respectively. They concluded that the formation of defect within the crystal was easier than that on surface. This work would assist in tailoring the electronic structures of gallium arsenide, thus favouring the development of high-performance electronic devices.

Two papers on ZnO are contributed to this issue. One is on thin film ZnO and the other on 1-dimensional ZnO nanorods. L. Meng et al. report 2-dimensional electron-gas (2DEG) properties of a Zn polar ZnMgO/MgO/ZnO structure with low Mg composition layer ($x = 0.05$) grown on a-plane (11–20) sapphire by radical-source laser molecular beam epitaxy. They observed that the insertion of a thin (1 nm) MgO layer between ZnMgO and ZnO layers in the ZnMgO/ZnO 2DEG structures resulted in an increase of the sheet density and affected the electron mobility slightly. The resultant carrier concentration was as high as $1.1 \times 10^{13} \text{ cm}^{-2}$ and the Hall mobility was as high as $3090 \text{ cm}^2/\text{Vs}$ at 10 K and $332 \text{ cm}^2/\text{Vs}$ at RT. The authors also calculated the dependence of carrier sheet density of the 2DEG on ZnMgO

layer thickness, which was consistent with the experiments. Y. Zhang et al. report the high-quality nitrogen-doped ZnO nanorods selectively grown on patterned and bare ZnO templates by the combination of nanoimprint lithography and chemical vapor transport methods. It is encouraging that the grown nanorods were uniform in size and orientation with controllable density and surface-to-volume ratio. They also analysed the structural and optical properties of the nitrogen-doped ZnO nanorods in detail.

Both fundamental and practical researches on III-nitride are presented. The mechanism of dislocations and interface roughness effect on the 2DEG mobility limitation in an AlGaN/AlN/GaN heterostructure is reported theoretically and experimentally by L. Meng et al. They observed that the charge impurities scattering limited the 2DEG mobility at low and moderate temperatures, followed by the dislocation and interface roughness scattering, whereas the polar optical phonon scattering was dominant above 200 K. S.-L. Jeng et al. established a standardized electrical measurement procedure for GaN power transistors, which provided necessary information for designers. In addition, the authors proposed an isolated gate driver detection method for sorting the uniformity of the power transistors from the option of the turn-off characteristic. They provided an equivalent-circuit model for GaN FETs on the basis of the measured electrical characteristics. In order to inhibit the effect of current crowding and to improve the yield of high-voltage single-chip GaN light-emitting diode (LED), W. Wang et al. put forward a parallel and series network structure. Based on this design, a 3W-LED chip of 24 parallel stages was demonstrated at the current of 500 mA with a mm² large area.

The recent work on semiconductor diamond is also shown. W. Wang et al. report a Zr-gate diamond field-effect transistor with SiN_x dielectric layers (SD-FET). The FET utilized the p-type surface conductivity of intrinsic diamond terminated by surface hydrogen. The fabricated FET was normally on with a sheet hole density of $2.17 \times 10^{13} \text{ cm}^{-2}$ and mobility of $24.4 \text{ cm}^2 \cdot \text{V}^{-1} \cdot \text{s}^{-1}$. The drain current density was less than 10 mA/mm. H. Li et al. present a review of the recent progress in three diamond nanostructures, 2-dimensional diamond film, nanostructural surface on diamond, and diamond nanoheterojunction. The future challenges in these topics were addressed.

In addition, controlled growth of Scheelite-type BaMoO₄ microstructures was reported by Y. Yin et al. And K. M. Lee et al. investigated the mechanism and kinetics for photocatalytic oxidation degradation by using ZnO as a photocatalyst.

Despite limited submissions, this special issue covers a wide range of topics from fundamental theoretical calculation, materials growth, and device physics to applications on wide-bandgap semiconductors nanostructures. The importance of wide-bandgap semiconductor is further demonstrated by the 2014 Nobel Laureate in Physics to Professor Isamu Akasaki, Professor Hiroshi Amano, and Professor Shuji Nakamura for their contributions in LEDs based on III-nitrides. We hope that this special issue, launched in August 2014, is timely to the readers for references in the related research fields.

Acknowledgments

The editors would like to sincerely express their thanks to the authors for the submissions to this special issue. We also greatly appreciate the reviewers for their constructive comments on the manuscripts.

*Meiyong Liao
Thomas Stergiopoulos
Jose Alvarez
Surojit Chattopadhyay
Guihua Zhang*

Research Article

A 3 W High-Voltage Single-Chip Green Light-Emitting Diode with Multiple-Cells Network

W. Wang,^{1,2} Y. Cai,² Y. B. Zhang,² H. J. Huang,² W. Huang,³ H. O. Li,³
B. S. Zhang,² and H. X. Wang¹

¹Key Laboratory for Physical Electronics and Devices of the Ministry of Education, Xi'an Jiaotong University, Xi'an, Shaanxi 710049, China

²Key Laboratory of Nanodevices and Applications, Suzhou Institute of Nano-Tech and Nano-Bionics, Chinese Academy of Sciences, Suzhou, Jiangsu 215123, China

³WuXi Jingkai Technology Co., Ltd., Wuxi, Jiangsu 214061, China

Correspondence should be addressed to Y. Cai; ycai2008@sinano.ac.cn

Received 6 March 2015; Revised 27 April 2015; Accepted 27 April 2015

Academic Editor: Meiyong Liao

Copyright © 2015 W. Wang et al. This is an open access article distributed under the Creative Commons Attribution License, which permits unrestricted use, distribution, and reproduction in any medium, provided the original work is properly cited.

A parallel and series network structure was introduced into the design of the high-voltage single-chip (HV-SC) light-emitting diode to inhibit the effect of current crowding and to improve the yield. Using such a design, a $6.6 \times 5 \text{ mm}^2$ large area LED chip of 24 parallel stages was demonstrated with 3 W light output power (LOP) at the current of 500 mA. The forward voltage was measured to be 83 V with the same current injection, corresponding to 3.5 V for a single stage. The LED chip's average thermal resistance was identified to be 0.28 K/W by using infrared thermography analysis.

1. Introduction

The compound semiconductor GaN is a promising material for blue-green light-emitting diodes (LEDs) and construction of white light sources. LEDs have numerous applications [1, 2]; thus they have attracted considerable attention. Commercialized LEDs are now being used in many areas such as general illumination [3], signaling, and back lighting in liquid crystal displays [4]. However, high-power LEDs used in projector, fluorescence microscopy, and general lighting still require much of research effort.

There are several methods proposed to improve LED's performance based on two aspects. One is to enhance the quantum efficiency of GaN materials such as insertion of an AlN interlayer [5], low temperature GaN [6] for stress reduction, patterned sapphire substrates (PSSs) [7], epitaxial lateral overgrowth (ELOG) [8], and some other modified ELOG techniques [9]. Another is to improve the LED's efficiency droop, such as suppression of Auger recombination [10], polarization matched GaN [11], and insertion of electron blocking layer (EBL) [12]. As a common sense, the most direct approach to improve the optical power is to enlarge the chip's

size. Alternating-current light-emitting diodes (AC-LEDs) [13] and high-voltage LEDs (HV-LEDs) [14] with serial connection structure were demonstrated to overcome low light extraction efficiency (LEE), poor current spreading, and serious luminous efficiency droop. However, AC-LEDs waste half of the active area and HV-LEDs are out of work if one of the LED cells becomes open circuit. Furthermore, an even larger area LED needs a special design to make sure that the LED chip has a high product yield. In particular, with the design in this work, the cost of the package for traditional HV-LEDs and AC-LEDs used as module can be reduced. And it will lead to a more compact lighting system for applications.

Recently, we fabricated a high-voltage single-chip large area ($6.6 \times 5 \text{ mm}^2$) green LED with 3 W light output power. In this paper, the electrical and optical properties of this green LED are presented. The 2-dimensional junction temperature distribution was also analyzed.

2. LED Chip Design and Fabrication

A special design of parallel and series network with multiple small LED cells was presented to improve the yield and

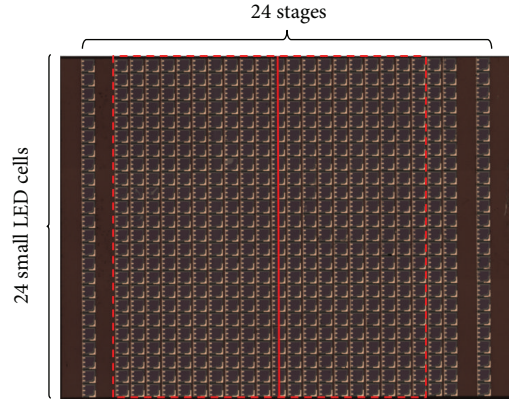


FIGURE 1: The micro photo of a HV-SC LED chip with 24 parallel stages ($6.6 \times 5 \text{ mm}^2$).

overcome the current crowding effect. As shown in Figure 1, the HV-SC LED chip consists of 24 parallel stages connected in series, and each stage has 24 small LED cells in parallel connection. The size of a small LED cell is $200 \times 200 \mu\text{m}^2$.

In this work, the InGaN/GaN LED wafer was acquired commercially from Xiangneng Hualei Optoelectronic Co. Ltd. with a wavelength of 520 nm. After the cleaning of GaN epiwafer, a SiO_2 hard mask layer for isolation region etching and mesa etching was deposited on the p-type GaN layer using plasma-enhanced chemical vapor deposition (PECVD, Oxford System 100). After the SiO_2 mask was patterned, the isolation etching and mesa etching were carried out, respectively, by an inductively coupled plasma (ICP) system (Oxford ICP 180). A sidewall slope of approximately 45° was selected to form on the GaN epiwafer for smooth coverage of interconnect metal. A dielectric layer of 200 nm SiO_2 was then deposited, and the RIE dry etching was carried out to open the dielectric window. After that, an indium tin oxide (ITO) film was deposited and wet-etched to form p-contact. A Ti/Al/Ni/Au multilayer was subsequently evaporated on the epiwafer to form n-contact and interconnection metals. An Al back reflector was sputtered on the back of the sapphire substrate after polishing down to $150 \mu\text{m}$. The chip was mounted on an Al based heat sink by the soldering, and a hemispherical borosilicate glass lens with 13 mm diameters was covered on the chip by KER2500 AB silicone.

3. Results and Discussion

Figure 2 shows the typical I - V characteristics of the fabricated HV-SC LED evaluated by Keithley 4200. The measured forward voltage is 83 V, corresponding to 3.5 V for each parallel stage at 500 mA. A reverse leakage current of 8 nA is measured at -120 V, confirming the advantage of suppressing reverse leakage current in the series connected HV LED chips compared with the single parallel stage, whose reverse current is several microamperes at -5 V.

The optical properties of a HV-SC LED were measured by Everfine HAAS 2000 spectrometer with a large integrating sphere of 1.5 m inner diameter. A fan of ~ 1 W was set

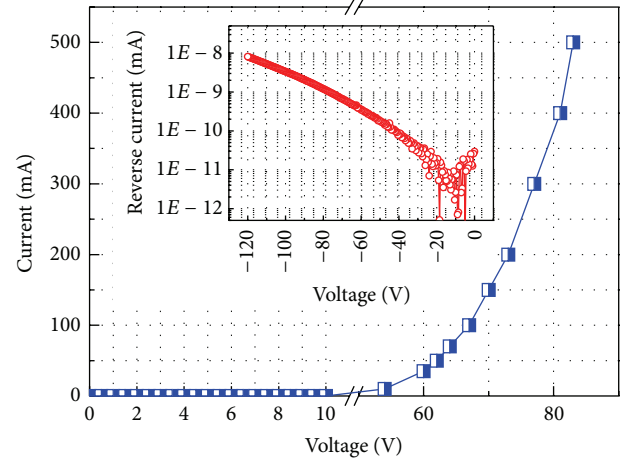


FIGURE 2: Typical I - V characteristics of a HV-SC LED and the reverse current in the inset.

at the back of the device for cooling. Figure 3 presents a luminous photo of the LED driven at 10 mA, and the LOP and external quantum efficiency (EQE) varying with injection current. As shown in Figure 3(b), the green light output power was measured to be 3 W at 500 mA, and the EQE was calculated to be 12.6%, which is 44.2% lower than its peak value of 22.6% at 35 mA. The light output power provided by the wafer suppliers was about 60 mW at the current of 350 mA for the chip size of $30 \times 30 \text{ mil}^2$. The 9% EQE of the HV-SC LED agreed with the reference value of 8.9% calculated by the parameters for the wafers, at the same current density, without lens.

Infrared thermography analysis using QFI InfraScope II was also carried out to display the junction temperature distribution and calculate the average junction temperature. The HV-SC LED chip was mounted on a thermostatic plate with a constant temperature of 23°C by thermal conductive silica gel.

Figure 4 shows the 2D junction temperature distribution on the chip area highlighted by the red dashed line, as indicated in Figure 1. Due to the heat crowding effect, the junction temperature at the center is higher than that at the periphery. The temperature profile along the red line from bottom to top in Figure 1 is plotted in Figure 5. The temperature at the center (T_c) is about 36.8°C , while the temperature at the edge (T_e) is about 30.7°C .

To evaluate the heat dissipation capacity of this large area LED chip, the average thermal resistance ($R_{J_Average}$) and the peak thermal resistance (R_{J_Peak}) should be considered. They can be calculated by the following equation (see [15]):

$$R_{JX} = \frac{T_J - T_a}{P_H}, \quad (1)$$

where R_{JX} , T_J , T_a , and P_H are the thermal resistance, the junction temperature, the ambient temperature, and the heat dissipation power, respectively. T_J was 33.8°C and 36.8°C for $R_{J_Average}$ and R_{J_Peak} , respectively. So, $R_{J_Average}$ and R_{J_Peak} were evaluated to be 0.28 K/W and 0.36 K/W, corresponding

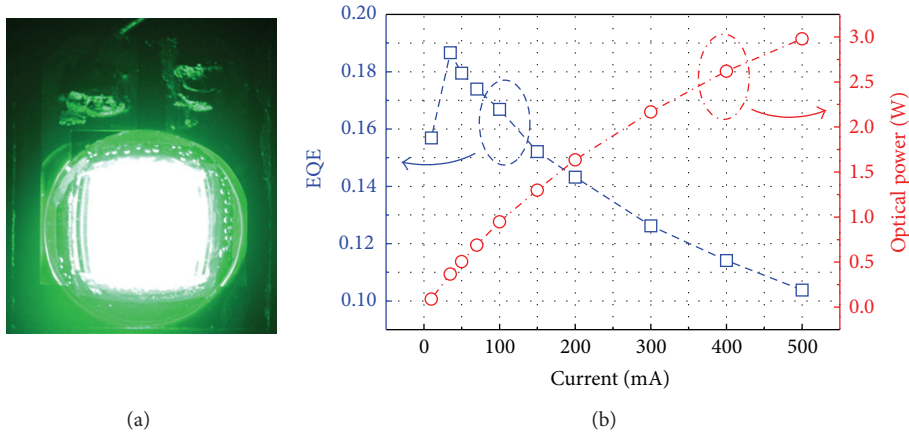


FIGURE 3: (a) The luminous photo of a HV-SC LED with optical lens driven at 10 mA and (b) the LOP and external quantum efficiency (EQE) of the HV-SC LED.

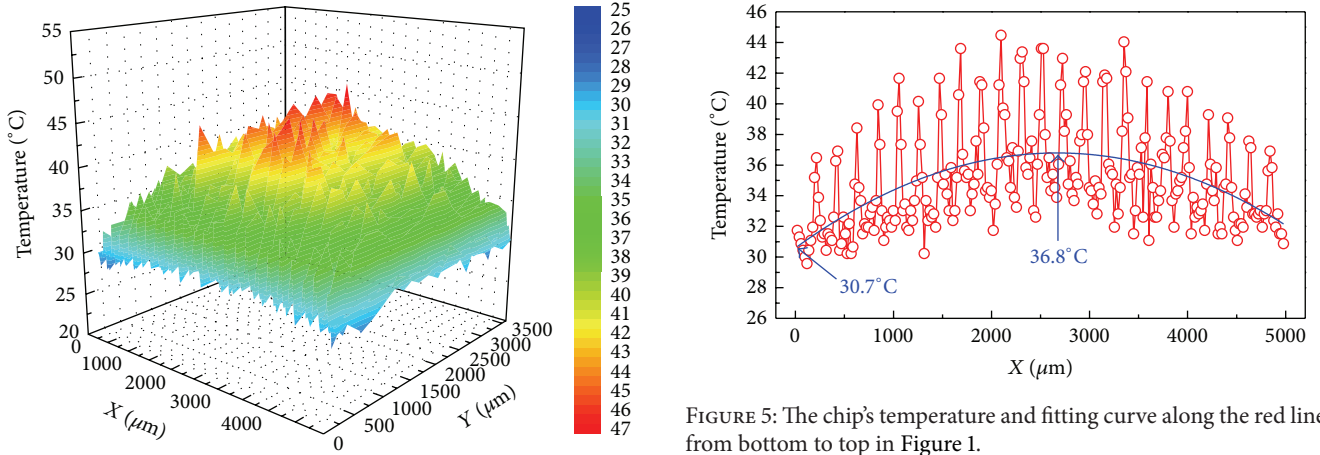


FIGURE 4: 2D junction temperature distribution in the red dashed line highlighted area in Figure 1.

to $R_{J_Peak}/R_{J_Average}$ ratio of 1.29, showing the extent of the heat crowding effect.

For the heat flow through the plate with the constant cross-sectional area, the average thermal resistance can also be calculated by (2), according to the definition

$$R_T = \frac{1}{\kappa} \cdot \frac{L}{A}, \quad (2)$$

where R_T is the average thermal resistance, κ is the thermal conductivity, L is the chip's thickness, and A is the area. The average thermal resistance of the HV-SC chip was calculated to be 0.26 K/W, 0.02 K/W higher than the calculated result because of the heat crowding effect and the additional thermal resistances of the silica gel and the heat sink.

It is well known that the forward current density of an LED strongly depends on the junction temperature, as shown in the following equation (see [16]):

$$J \propto T^{3+\gamma/2} \exp\left(\frac{q(V - IR_s - V_i)}{n_{ideal}kT}\right). \quad (3)$$

FIGURE 5: The chip's temperature and fitting curve along the red line from bottom to top in Figure 1.

So the junction temperature spatial distribution leads to the forward current density spatial distribution. For a junction temperature distribution as shown in Figure 5, the current density at the center of the chip (J_c) should be higher than that at the edge (J_e), implying a current crowding effect. It should be noted that the small LED cells along the red line, as shown in Figure 1, are connected in parallel. The ratio of J_c/J_e represents the extent of the current crowding. In practice, when this ratio $\leq e$ (Euler's number), the device is considered appropriately designed [3].

According to (3), the ratio of J_c/J_e can be expressed as

$$\frac{J_c}{J_e} = \left(\frac{T_c}{T_e}\right)^{3+\gamma/2} \frac{\exp(q(V - I_c R_s - V_i)/n_{ideal}kT_c)}{\exp(q(V - I_e R_s - V_i)/n_{ideal}kT_e)}, \quad (4)$$

where T_c and T_e were found to be 36.8°C and 30.7°C, respectively, in Figure 5. V_i is estimated to be 3.4 V in $\text{In}_{0.2}\text{Ga}_{0.8}\text{N}/\text{GaN}$ QWs [17] and γ is regarded as 2 to evaluate the maximum value of the J_c/J_e ratio. As a result, the ratio of J_c/J_e was estimated less than 1.029, which is much less than e (~ 2.72), indicating no obvious current crowding effect, thus validating the effectiveness of the chip design.

4. Conclusion

In this study, we introduced a parallel and series network structure into the design of a large area high-power LED chip, which suppresses the effect of current crowding and enhances the fabrication yield of the LED chip. We also successfully demonstrated a $6.6 \times 5 \text{ mm}^2$ large area HV-SC green LED array of 24 parallel stages. With a driven current at 500 mA, the forward voltage was measured to be 83 V, 3.5 V for each stage, and 3 W light output power with an EQE of 12.6%. Based on the infrared thermography analysis, the measured average thermal resistance was 0.28 K/W and the self-heating induced current crowding is negligible. Such a high-power, high-voltage LED device has a great potential in RGB solid state lighting.

Conflict of Interests

The authors declare that there is no conflict of interests regarding the publication of this paper.

Acknowledgments

The authors would like to thank the National Natural Science Foundation of China (no. 10990102) and Jiangsu Natural Science Foundation (BK2011173) for partially financially supporting this research.

References

- [1] J. J. Wierer Jr., A. David, and M. M. Megens, "III-nitride photonic-crystal light-emitting diodes with high extraction efficiency," *Nature Photonics*, vol. 3, no. 3, pp. 163–169, 2009.
- [2] S. Nakamura, T. Mukai, and M. Senoh, "Candela-class high-brightness InGaN/AlGaIn double-heterostructure blue-light-emitting diodes," *Applied Physics Letters*, vol. 64, no. 13, pp. 1687–1689, 1994.
- [3] E. F. Schubert, *Light-Emitting Diodes*, Cambridge University Press, New York, NY, USA, 2nd edition, 2006.
- [4] Y. Narukawa, I. Niki, K. Izuno, M. Yamada, Y. Murazaki, and T. Mukai, "Phosphor-conversion white light emitting diode using InGaN near-ultraviolet chip," *Japanese Journal of Applied Physics*, vol. 41, no. 4, pp. L371–L373, 2002.
- [5] A. Dadgar, M. Poschenrieder, J. Bläsing, K. Fehse, A. Diez, and A. Krost, "Thick, crack-free blue light-emitting diodes on Si(111) using low-temperature AlN interlayers and *in situ* Si_xN_y masking," *Applied Physics Letters*, vol. 80, no. 20, pp. 3670–3672, 2002.
- [6] Y. L. Tsai and J. R. Gong, "Improvement in optical properties and surface morphologies of GaN films using low-temperature GaN interlayers," *Journal of Crystal Growth*, vol. 263, no. 1–4, pp. 176–180, 2004.
- [7] S. J. Chang, Y. C. Lin, Y. K. Su et al., "Nitride-based LEDs fabricated on patterned sapphire substrates," *Solid-State Electronics*, vol. 47, no. 9, pp. 1539–1542, 2003.
- [8] P. Vennéguès, B. Beaumont, V. Bousquet, M. Vaille, and P. Gibart, "Reduction mechanisms for defect densities in GaN using one- or two-step epitaxial lateral overgrowth methods," *Journal of Applied Physics*, vol. 87, no. 9, pp. 4175–4181, 2000.
- [9] D. W. Kim, C. H. Jeong, K. N. Kim et al., "High rate sapphire (Al₂O₃) etching in inductively coupled plasmas using axial external magnetic field," *Thin Solid Films*, vol. 435, no. 1–2, pp. 242–246, 2003.
- [10] K. T. Delaney, P. Rinke, and C. G. van de Walle, "Auger recombination rates in nitrides from first principles," *Applied Physics Letters*, vol. 94, no. 19, pp. 191109–191112, 2009.
- [11] M. H. Kim, W. Lee, D. Zhu et al., "Partial polarization matching in GaInN-based multiple quantum well blue LEDs using ternary GaInN barriers for a reduced efficiency droop," *IEEE Journal on Selected Topics in Quantum Electronics*, vol. 15, no. 4, pp. 1122–1127, 2009.
- [12] Y. Y. Zhang, X. L. Zhu, Y. A. Yin, and J. Ma, "Performance enhancement of near-UV Light-emitting diodes with an InAlN/GaN superlattice electron-blocking layer," *IEEE Electron Device Letters*, vol. 33, pp. 994–996, 2012.
- [13] J. P. Ao, H. Sato, T. Mizobuch et al., "Monolithic blue LED series arrays for high-voltage AC operation," *Physica Status Solidi (A)*, vol. 194, pp. 376–379, 2002.
- [14] R.-H. Horng, K.-C. Shen, Y.-W. Kuo, and D.-S. Wu, "Effects of cell distance on the performance of GaN high-voltage light emitting diodes," *ECS Solid State Letters*, vol. 1, no. 5, pp. R21–R23, 2012.
- [15] S. Murata and H. Nakada, "Adding a heat bypass improves the thermal characteristics of a 50 μm spaced 8-beam laser diode array," *Journal of Applied Physics*, vol. 72, no. 6, pp. 2514–2516, 1992.
- [16] E. K. Liu, B. S. Zhu, and J. S. Luo, *The Physics of Semiconductors*, Publishing House of Electronics Industry, Beijing, China, 7th edition, 2014.
- [17] F. Chen and A. N. Cartwright, "Out-of-well carrier screening in a strained In_xGa_{1-x}N/GaN multiple quantum well structure," *Physical Review B*, vol. 68, Article ID 233304, 2003.

Research Article

Density Functional Theory Study on Defect Feature of $\text{As}_{\text{Ga}}\text{Ga}_{\text{As}}$ in Gallium Arsenide

Deming Ma, Xi Chen, Hongbo Qiao, Wei Wang, Wei Shi, and Enling Li

Department of Applied Physics, Xi'an University of Technology, Xi'an 710054, China

Correspondence should be addressed to Deming Ma; xautmdm@163.com

Received 1 September 2014; Accepted 12 January 2015

Academic Editor: Meiyong Liao

Copyright © 2015 Deming Ma et al. This is an open access article distributed under the Creative Commons Attribution License, which permits unrestricted use, distribution, and reproduction in any medium, provided the original work is properly cited.

We investigate the defect feature of $\text{As}_{\text{Ga}}\text{Ga}_{\text{As}}$ defect in gallium arsenide clusters in detail by using first-principles calculations based on the density functional theory (DFT). Our calculations reveal that the lowest donor level of $\text{As}_{\text{Ga}}\text{Ga}_{\text{As}}$ defect on the gallium arsenide crystal surface is 0.85 eV below the conduction band minimum, while the lowest donor level of the $\text{As}_{\text{Ga}}\text{Ga}_{\text{As}}$ defect inside the gallium arsenide bulk is 0.83 eV below the bottom of the conduction band, consistent with gallium arsenide EL2 defect level of experimental value (Ec-0.82 eV). This suggests that $\text{As}_{\text{Ga}}\text{Ga}_{\text{As}}$ defect is one of the possible gallium arsenide EL2 deep-level defects. Moreover, our results also indicate that the formation energies of internal $\text{As}_{\text{Ga}}\text{Ga}_{\text{As}}$ and surface $\text{As}_{\text{Ga}}\text{Ga}_{\text{As}}$ defects are predicted to be around 2.36 eV and 5.54 eV, respectively. This implies that formation of $\text{As}_{\text{Ga}}\text{Ga}_{\text{As}}$ defect within the crystal is easier than that of surface. Our results offer assistance in discussing the structure of gallium arsenide deep-level defect and its effect on the material.

1. Introduction

As a kind of excellent semiconductor material, gallium arsenide is widely used in fast photoelectric devices and integrated circuit substrate [1] and so forth. As a compound semiconductor material, the defect problems of the undoped semi-insulating GaAs (SI-GaAs), in particular, the unique deep-level defects in the SI-GaAs single crystal material, such as EL2 (Ec-0.82 eV) and EL6 (Ec-0.38 eV), which have an important influence on the photoelectric characteristics and the application of materials [2–7], are more complex than those of silicon and germanium. By various theoretical and experimental means, many researchers have studied the microstructures of gallium arsenide EL2 deep-levels. For example, Lagowski et al. put forward isolated As_{Ga} antisite defect structure type [8], Wager and van Vechten put forward $\text{V}_{\text{Ga}}\text{As}_{\text{Ga}}\text{V}_{\text{Ga}}$ ternary complex defect structure type [9], Zou et al. put forward $\text{As}_{\text{Ga}}\text{V}_{\text{As}}\text{V}_{\text{Ga}}$ ternary complex defect structure type [10, 11], and Morrow proposes the possible $\text{As}_{\text{Ga}}\text{V}_{\text{Ga}}$ defect structures [12]. Wosinski et al. pointed out that EL2 is not isolated defects [13]. The steady and metastable energy levels of EL2 in semi-insulating GaAs were studied by Kabiraj and Ghosh [14]. Ternary complex defect model of EL2 defect

has been studied by using first-principles by Li et al. [7], and EL2 and EL6 defects and correlations of clusters have been preliminarily discussed by Zhao and Wu [15]. These results have a certain role in promoting of the features and applications of gallium arsenide materials. On the basis of the above study on gallium arsenide clusters and defects preliminary [16–19], in this paper, the $\text{As}_{\text{Ga}}\text{Ga}_{\text{As}}$ defect and its features have been studied by first-principles based on density functional theory (DFT), which gives out another kind of microstructure of gallium arsenide EL2 deep-level defects and offers assistance in the discussion of defect features of gallium arsenide deep-level and application of materials.

2. Computational Methods

Our total energy and electronic structure calculations were carried out within a revised Heyd-Scuseria-Ernzerhof (HSE06) range-separated hybrid functional as implemented in VASP code [20, 21]. In the HSE06 approach, the screening parameter $\mu = 0.2 \text{ \AA}^{-1}$ and the Hartree-Fock (HF) mixing parameter $\alpha = 25\%$ which meant 25% HF exchange with 75% GGA of Perdew, Burke, and Ernzerhof (PBE) [22]

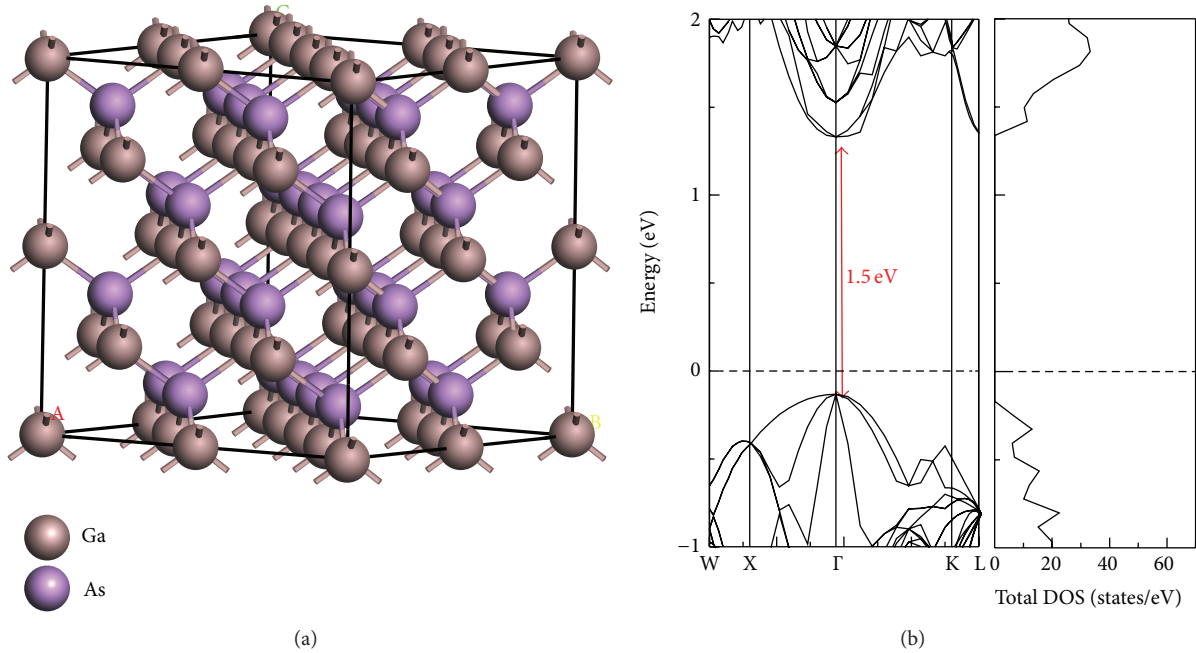


FIGURE 1: (a) Supercell structure model of perfect GaAs. (b) Band structure and the total DOS of perfect GaAs. The Fermi energy is set to zero.

exchange were chosen to well reproduce the experimental band gap (~ 1.43 eV) of GaAs. The core-valence interaction was described by the frozen-core projector augmented wave (PAW) method [23, 24]. The electronic wave functions were expanded in a plane wave basis with a cut-off of 300 eV. A $3 \times 3 \times 3$ k-point mesh within Monkhorst-Pack scheme [25] was applied to the Brillouin-zone integrations in total energy calculations. The internal coordinates in the defective supercells were relaxed to reduce the residual force on each atom to less than $0.02 \text{ eV} \cdot \text{\AA}^{-1}$. All defect calculations were spin-polarized. In the calculation, firstly, defect structure models in various conditions were optimized and then static self-consistent calculation to the ground state structure was conducted and, finally, the corresponding band structure and density of states (DOS) were obtained.

3. Results and Discussions

3.1. The Properties of Perfect GaAs. Figure 1(a) shows the perfect GaAs supercell structure model. Figure 1(b) shows the calculated band structure and total density of states (DOS) of the perfect GaAs supercell structure model.

As can be seen from Figure 1(b), the perfect GaAs has a direct band gap structure, and its band gap is 1.5 eV at the Γ point, which is very close to the experimental value (1.43 eV), implying that the selected parameters are reasonable.

3.2. Surface Doping $\text{As}_{\text{Ga}}\text{Ga}_{\text{As}}$ Defect. Figure 2(a) shows the supercell structure model of GaAs (001) surface doping $\text{As}_{\text{Ga}}\text{Ga}_{\text{As}}$ complex defect. The crystal thickness and vacuum thickness are 8.24 \AA and 20.00 \AA , respectively. The length

of the base vectors A and B is for both 15.99 \AA , whereas the length of the base vector C is 28.24 \AA . Furthermore, vector angles α , β , and γ are all 90° . Figure 2(b) shows the band structure and the total DOS of the GaAs (001) surface $\text{As}_{\text{Ga}}\text{Ga}_{\text{As}}$ complex defect model.

As can be seen from Figure 2(b), the lowest donor defect level of the $\text{As}_{\text{Ga}}\text{Ga}_{\text{As}}$ defect on the gallium arsenide crystal surface is 0.85 eV below the bottom of the conduction band, being consistent with gallium arsenide EL2 defect level of experimental value ($E_c - 0.82$ eV), which suggests that $\text{As}_{\text{Ga}}\text{Ga}_{\text{As}}$ defect is one of the possible microstructures of gallium arsenide EL2 deep-level defects, and the formation energy of $\text{As}_{\text{Ga}}\text{Ga}_{\text{As}}$ defect is 5.54 eV.

One can note that the existence of $\text{As}_{\text{Ga}}\text{Ga}_{\text{As}}$ defect changes the band structure and the total DOS of GaAs. This leads to the formation of dangling bond between the neighbors of defects. As a result, the matching surface states can exchange their positions with holes and electrons of the gallium arsenide materials, which affected the photoelectric properties of GaAs materials directly.

3.3. Internal Doping $\text{As}_{\text{Ga}}\text{Ga}_{\text{As}}$ Defect. The supercell structure model of the internal deep layer doping $\text{As}_{\text{Ga}}\text{Ga}_{\text{As}}$ defect is displayed in Figure 3(a). The distance between the $\text{As}_{\text{Ga}}\text{Ga}_{\text{As}}$ defect and the upper interface is 5.65 \AA . Figure 3(b) shows the supercell structure model of the internal shallow layer doping $\text{As}_{\text{Ga}}\text{Ga}_{\text{As}}$ defect, and the distance between the $\text{As}_{\text{Ga}}\text{Ga}_{\text{As}}$ defect and the upper interface is 2.83 \AA . Figures 4(a) and 4(b) show the corresponding band structure and total DOS, respectively.

As can be seen from Figure 4, the band structure and DOS of internal $\text{As}_{\text{Ga}}\text{Ga}_{\text{As}}$ defect are insensitive to its position.

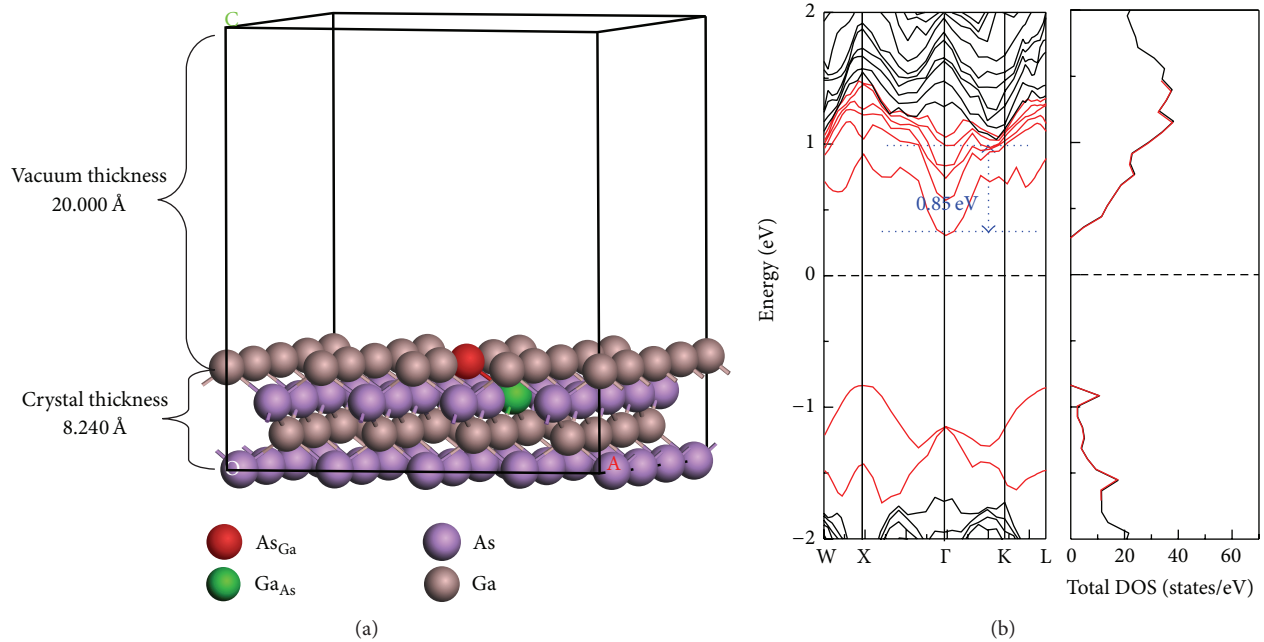


FIGURE 2: (a) Supercell structure model of the surface double antisite $\text{As}_{\text{Ga}}\text{Ga}_{\text{As}}$ defect. (b) The band structure and the total DOS of GaAs (001) surface with double antisite $\text{As}_{\text{Ga}}\text{Ga}_{\text{As}}$ defect.

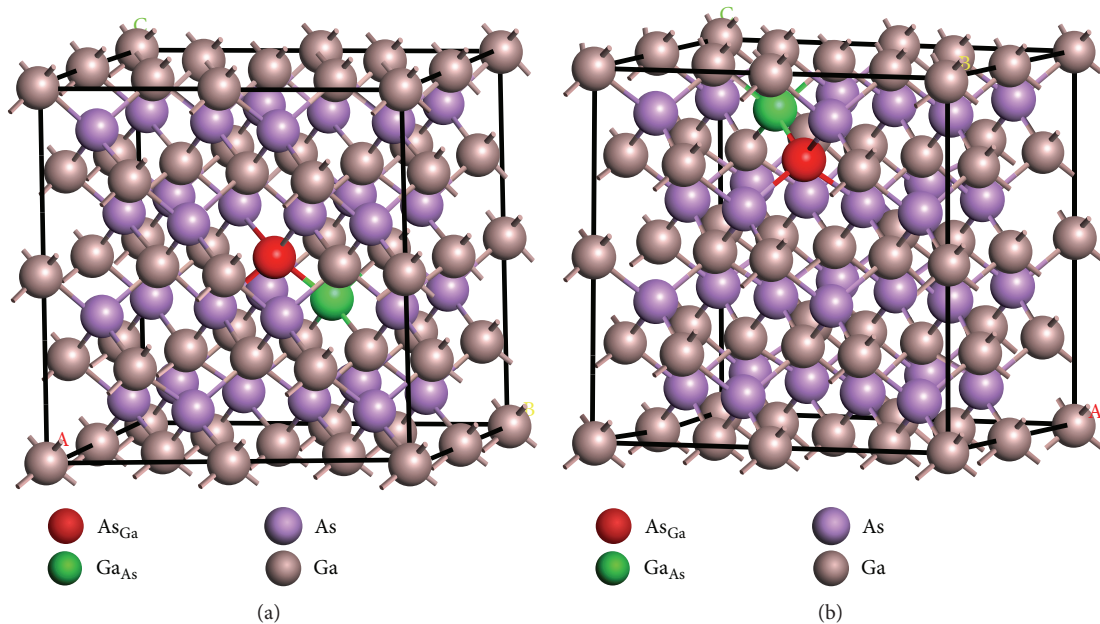


FIGURE 3: Supercell structure model of internal double antisite $\text{As}_{\text{Ga}}\text{Ga}_{\text{As}}$ defects. (a) Between the $\text{As}_{\text{Ga}}\text{Ga}_{\text{As}}$ defects and the upper interface the distance is 5.653 Å. (b) The distance between the $\text{As}_{\text{Ga}}\text{Ga}_{\text{As}}$ defects and the upper interface is 2.827 Å.

The lowest donor defect level is below the bottom of the conduction band 0.83 eV, being consistent with gallium arsenide EL2 defect level of experimental value ($E_c - 0.82$ eV). This suggests that internal $\text{As}_{\text{Ga}}\text{Ga}_{\text{As}}$ defect is one of possible gallium arsenide EL2 deep-level defects. Meanwhile, it increases donor level and acceptor level of defects, changes the total DOS of materials, and affects the photoelectric properties

of GaAs materials directly, when comparing with the band structure of perfect GaAs as shown in Figure 1(b). The results indicate that the formation energy of internal $\text{As}_{\text{Ga}}\text{Ga}_{\text{As}}$ defect is 2.36 eV, showing an independent-position character. Note that the internal $\text{As}_{\text{Ga}}\text{Ga}_{\text{As}}$ defect is more stable than the surface $\text{As}_{\text{Ga}}\text{Ga}_{\text{As}}$ one, suggesting that formation of $\text{As}_{\text{Ga}}\text{Ga}_{\text{As}}$ deep-level defects in the crystal is easier than that on surface.

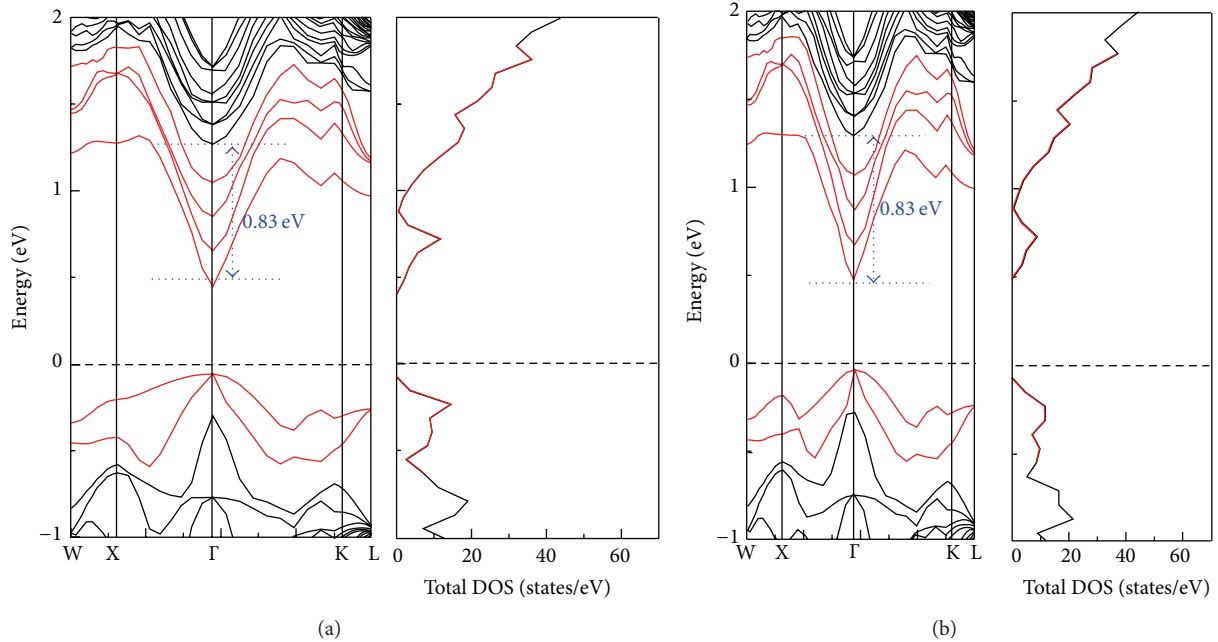


FIGURE 4: The band structure and the total DOS of GaAs with internal double antisite $\text{As}_{\text{Ga}}\text{Ga}_{\text{As}}$ defects. (a) The distance is 5.653 Å between the deep $\text{As}_{\text{Ga}}\text{Ga}_{\text{As}}$ defects and the upper boundary. (b) The distance is 2.827 Å between the shallow $\text{As}_{\text{Ga}}\text{Ga}_{\text{As}}$ defects and the upper boundary.

4. Conclusions

In this paper, we have carried out the $\text{As}_{\text{Ga}}\text{Ga}_{\text{As}}$ deep-level defect in gallium arsenide by using first-principles calculations based on hybrid density functional theory. Our results show that the lowest donor defect level on the gallium arsenide surface is 0.85 eV below the bottom of the conduction band, while the lowest donor defect level of the $\text{As}_{\text{Ga}}\text{Ga}_{\text{As}}$ defect inside the gallium arsenide crystal is 0.83 eV below the bottom of the conduction band, consistent with gallium arsenide EL2 defect level of experimental value ($E_c - 0.82$ eV). The $\text{As}_{\text{Ga}}\text{Ga}_{\text{As}}$ defect is one of the microstructures of the EL2 deep-level defects in gallium arsenide. We also found that the band structure and density of states of internal $\text{As}_{\text{Ga}}\text{Ga}_{\text{As}}$ defect have no relationship with its position and the formation energy of internal $\text{As}_{\text{Ga}}\text{Ga}_{\text{As}}$ defect is 3.16 eV, smaller than that of the defect on surface, suggesting that the formation of $\text{As}_{\text{Ga}}\text{Ga}_{\text{As}}$ deep-level defects within the crystal is easier than that of surface relatively. The existence of $\text{As}_{\text{Ga}}\text{Ga}_{\text{As}}$ defect increases donor level and acceptor level of defects and changes the total DOS of materials and atoms around the defect form the dangling bond. Consequently, the resulting surface states can exchange their positions with holes and electrons of the gallium arsenide materials, which affects the photoelectric properties of GaAs materials directly.

Conflict of Interests

The authors declare that there is no conflict of interests regarding the publication of this paper.

Acknowledgments

This work was supported by the National Natural Science Foundation of China (Grant nos. 50837005, 11304245), the Provincial Natural Science Special Foundation of Shaanxi in China (12JK0952), the Foundation of Shaanxi Key Science and Technology Innovation Team in China (2014KTC-13), the Shaanxi International Cooperation Project (2012KW-04), the Dr. Startup Foundation of the Xi'an University of Technology in China (108-211003), and the Features Research Foundation of the Xi'an University of Technology in China (108-211302).

References

- [1] M. J. Howes and D. V. Morgan, *Gallium Arsenide: Materials, Devices, and Circuits*, Wiley Series in Solid State Devices and Circuits, John Wiley & Sons, 1985.
- [2] M. Pavlović and U. V. Desnica, "Improvement in semi-insulating GaAs material quality: a comparative study of defects with deep levels," *Japanese Journal of Applied Physics*, vol. 37, part 1, p. 4687, 1998.
- [3] U. V. Desnica, M. Skowronski, and M. C. Cretella, "Comment on 'Pair of local vibration mode absorption bands related to EL2 defects in semi-insulating GaAs' [Appl. Phys. Lett. 5 0, 1666 (1987)]," *Applied Physics Letters*, vol. 52, article 760, 1988.
- [4] U. V. Desnica and B. Šantić, "Trap-induced photoconductivity in semi-insulating GaAs," *Journal of Applied Physics*, vol. 67, p. 1408, 1990.
- [5] B. Šantić, D. I. Desnica, B. G. Petrović, and U. V. Desnica, "Quenching and enhancement of photoconductivity in semi-insulating GaAs," *Solid State Communications*, vol. 74, no. 8, pp. 847–850, 1990.

- [6] U. V. Desnica, "Persistent photocurrents in semi-insulating gallium arsenide," *Radiation Effects and Defects in Solids*, vol. 83, p. 111, 1989.
- [7] D. Li, M. Yang, Y. Cai, S. Zhao, and Y. Feng, "First principles study of the ternary complex model of EL2 defect in GaAs saturable absorber," *Optics Express*, vol. 20, no. 6, pp. 6258–6266, 2012.
- [8] J. Lagowski, H. C. Gatos, J. M. Parsey, K. Wada, M. Kaminska, and W. Walukiewicz, "Origin of the 0.82-eV electron trap in GaAs and its annihilation by shallow donors," *Applied Physics Letters*, vol. 40, no. 4, article 342, 1982.
- [9] J. F. Wager and J. A. van Vechten, "Atomic model for the EL2 defect in GaAs," *Physical Review B*, vol. 35, no. 5, pp. 2330–2339, 1987.
- [10] Y. X. Zou, G. Y. Wang, S. Benakki, A. Goltzene, and C. Schwab, "Comment on 'atomic model for the EL2 defect in GaAs,'" *Physical Review B*, vol. 38, pp. 10953–10955, 1988.
- [11] G. Y. Wang, Y. X. Zou, S. Benakki, A. Goltzene, and C. Schwab, "Identification of paramagnetic As_{Ga} and optical EL2 centers in semi-insulating gallium arsenide," *Journal of Applied Physics*, vol. 63, no. 8, pp. 2595–2602, 1988.
- [12] R. A. Morrow, "Model of EL2 formation in GaAs," *Journal of Applied Physics*, vol. 70, no. 11, pp. 6782–6789, 1991.
- [13] T. Wosinski, A. Makosa, and Z. Witzak, "Transformation of native defects in bulk GaAs under ultrasonic vibration," *Semiconductor Science and Technology*, vol. 9, no. 11, article 2047, 1994.
- [14] D. Kabiraj and S. Ghosh, "'EL2' revisited: observation of metastable and stable energy levels of EL2 in semi-insulating GaAs," *Applied Physics Letters*, vol. 87, Article ID 252118, 2005.
- [15] Z. Y. Zhao and F. M. Wu, "Investigation on a relation between EL2 group and EL6 group in SI-GaAs," *Journal of Functional Materials and Devices*, vol. 2, p. 32, 1996.
- [16] D. Ma, W. Shi, E. Li, L. Hou, and Y. Dai, "Structure and photoelectron energy spectrum of Ga_2As_n ion clusters," *Acta Optica Sinica*, vol. 29, pp. 1032–1037, 2009 (Chinese).
- [17] D. M. Ma, H. B. Qiao, W. Shi, E. L. Li, Y. H. Ma, and W. Wang, "First-principles study on stability and photoelectron spectroscopy of Ga_nAs_2 ($n=1-9$) clusters," *Spectrochimica Acta A: Molecular and Biomolecular Spectroscopy*, vol. 118, pp. 533–537, 2014.
- [18] D. M. Ma, H. B. Qiao, and E. L. Li, "Density functional theory study on stability and defect feature of Ga-rich Ga_nAs ($n=1-9$) clusters," *Chinese Journal of Atomic and Molecular Physics*, vol. 31, pp. 223–228, 2014.
- [19] D. M. Ma, H. B. Qiao, W. Shi, and E. L. Li, "Effect of the VAsVGa complex defect doping on properties of the semi-insulating GaAs," *Journal of Applied Physics*, vol. 115, no. 15, Article ID 153703, 2014.
- [20] G. Kresse and J. Furthmüller, "Efficiency of ab-initio total energy calculations for metals and semiconductors using a plane-wave basis set," *Computational Materials Science*, vol. 6, no. 1, pp. 15–50, 1996.
- [21] G. Kresse and J. Furthmüller, "Efficient iterative schemes for ab initio total-energy calculations using a plane-wave basis set," *Physical Review B: Condensed Matter and Materials Physics*, vol. 54, Article ID 11169, 1996.
- [22] J. P. Perdew, K. Burke, and M. Ernzerhof, "Generalized gradient approximation made simple," *Physical Review Letters*, vol. 77, no. 18, pp. 3865–3868, 1996.
- [23] P. E. Blöchl, "Projector augmented-wave method," *Physical Review B*, vol. 50, no. 24, pp. 17953–17979, 1994.
- [24] G. Kresse and D. Joubert, "From ultrasoft pseudopotentials to the projector augmented-wave method," *Physical Review B: Condensed Matter and Materials Physics*, vol. 59, no. 3, pp. 1758–1775, 1999.
- [25] H. J. Monkhorst and J. D. Pack, "Special points for Brillouin-zone integrations," *Physical Review B: Solid State*, vol. 13, no. 12, pp. 5188–5192, 1976.

Research Article

Mechanism and Kinetics Study for Photocatalytic Oxidation Degradation: A Case Study for Phenoxyacetic Acid Organic Pollutant

Kian Mun Lee, Sharifah Bee Abd Hamid, and Chin Wei Lai

Nanotechnology & Catalysis Research Centre (NANOCAT), 3rd Floor, Block A, Institute of Postgraduate Studies (IPS), University of Malaya, 50603 Kuala Lumpur, Malaysia

Correspondence should be addressed to Sharifah Bee Abd Hamid; sharifahbee@um.edu.my

Received 13 April 2015; Revised 23 May 2015; Accepted 25 May 2015

Academic Editor: Thomas Stergiopoulos

Copyright © 2015 Kian Mun Lee et al. This is an open access article distributed under the Creative Commons Attribution License, which permits unrestricted use, distribution, and reproduction in any medium, provided the original work is properly cited.

Photocatalysis is a rapidly expanding technology for wastewater treatment, including a wide range of organic pollutants. Thus, understanding the kinetics and mechanism of the photocatalytic oxidation (PCO) for degradation of phenoxyacetic acid (PAA) is an indispensable component of risk assessment. In this study, we demonstrated that the central composite design (CCD) coupled with response surface methodology (RSM) was successfully employed to probe the kinetics and mechanism of PCO degradation for PAA using an efficient zinc oxide (ZnO) photocatalyst. In our current case study, four independent factors such as ZnO dosage, initial concentration of PAA, solution pH, and reaction time on the PCO degradation for PAA were examined in detail. Based on our results obtained from RSM analyses, an efficient pathway leading to the high degradation rate (>90%) was applying 0.4 g/L of ZnO dosage with 16 mg/L of concentration of PAA at pH 6.73 for 40 minutes. The experimental results were fitted well with the derived response model with $R^2 = 0.9922$. This study offers a cost-effective way for probing our global environmental water pollution issue.

1. Introduction

Lately, global warming poses one of the most serious threats to the global environment ever faced in human history, especially water pollution. One of the major water pollutants is the use of pesticides and herbicides in agricultural fields that created severe environmental issue, which are considered a wide variety of persistent organic pollutants introduced into the natural water resources or wastewater treatment systems. In fact, the release of the persistent organic structure with toxicity property may cause negative effects on the environment and human health as the persistent organic structure compounds are very toxic and chemically stable and resist biodegradation [1–4]. The control of persistent organic pollutants in our natural water resources or wastewater treatment systems is an important issue. It is a well-known fact that PAA is a parent molecule for herbicides and pesticides for weed control. In particular, the discharge of this PAA effluent into the natural water resources or

wastewater treatment systems is undesirable. This is due to PAA possess various bioactivities, including anticancer, antitumor, analgesic, anti-inflammatory, inhibition of plant growth process and antimicrobial, which are harmful to human health [5–7]. Thus, PAA was selected as the model pollutant in our kinetics and mechanism study of direct oxidation organics in order to create a green and healthy living environment for our next generation.

In recent years, advanced oxidation processes (AOPs) system has attracted great interest from science community as the most promising way to solve the environmental problems, especially getting rid of residual dyes pollutants and mineralization and detoxification of various organic pollutants from wastewater stream [8–11]. In this manner, AOPs system is considered to be an ideal green environmental solution to realize our green economy future. In the field of photocatalysis today, ZnO-mediated heterogeneous photocatalyses have received increased interest due to their capability in degrading numerous kinds of contaminants

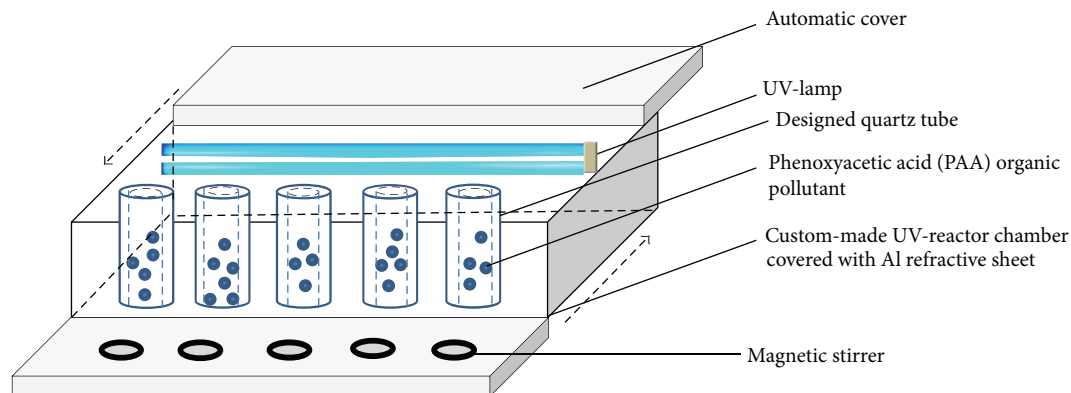


FIGURE 1: Experimental setup for the photocatalytic degradation of PAA.

into carbon dioxide and water [12–14]. Furthermore, ZnO catalysts emerged as the leading candidate in photocatalysis and appeared as a potential photocatalyst due to low cost, easy availability, excellent chemical stability, nontoxicity in nature, and high initial rate of activities [15, 16]. Moreover, ZnO is relatively cheaper and is able to absorb a wide range of UV spectrum compared to that of titanium dioxide (TiO_2) [17].

Several researchers have reported the removal of PAA from aqueous media by utilizing the titanium dioxide as the photocatalyst through conventional study [4, 18, 19]. However, an obvious hindrance to the widespread use of TiO_2 as a photocatalyst in this way is that it is time consuming and not cost-effective as more experiments need to be carried out in PAA removal if changing one parameter while fixing other processing parameters at constant value. Making intuitive guesses on their optimum processing parameters is more or less impossible, and a focused research on the area is a very challenging task. In this case study, response surface methodology (RSM) was applied in optimizing photocatalytic oxidation of various organics. This method is more practical by taking into account the interactive effects among the process parameters and could determine the optimal experimental conditions accurately with minimum labours [20, 21].

To the best of our knowledge, PAA removal using ZnO photocatalyst is still lacking at current stage. The optimization of PAA via multivariate approach has been developed in our case study. In this work, central composite design coupled with response surface study was adopted to optimize four process parameters, namely, ZnO loading, initial concentration of PAA, solution pH, and reaction time on the photocatalytic degradation of PAA. The kinetics and mineralization of PAA will be investigated and its possible photocatalytic degradation mechanism was proposed.

2. Experimental

2.1. Materials. Phenoxyacetic acid ($\text{C}_8\text{H}_8\text{O}_3$, 99% purity) was obtained from Sigma Aldrich. Zinc oxide (ZnO, 99% purity) was obtained from Merck. NaOH and HNO_3 obtained from Merck were used to adjust the pH of the reaction medium. All reagents were of analytical grade and were used

without further purification. Deionized water was used for the preparation of all aqueous solutions.

2.2. Photocatalytic Degradation of Phenoxyacetic Acid.

100 mg/L PAA solution was prepared by dissolving 0.05 g of powder in 500 mL of deionized water. The solutions used in the photodegradation process were prepared by diluting the stock solution to the desired concentration. Typically, a certain amount of the ZnO photocatalyst was loaded into 100 mL of PAA with known concentration in a quartz vessel. The experiments were carried out in a batch reactor as shown in Figure 1. This suspended solution was allowed to equilibrate for 15 minutes in the dark at room temperature ($28 \pm 2^\circ\text{C}$). Then a 96 W UV lamp ($\lambda = 365 \text{ nm}$) was switched on to initiate the photocatalytic degradation process. The reaction medium was agitated and was bubbled with air throughout the experiment to maintain homogeneous environment. The aliquot was then filtered by a $0.22 \mu\text{m}$ Nylon filter to remove the catalyst particles. Prior to analysis, a calibration curve was constructed using a series of standard solutions with known concentrations ($R^2 = 0.9990$). The concentration of PAA from the PCO experiments was determined by a Perkin Elmer Lambda 35 UV-Vis spectrophotometer at the λ_{max} of 269 nm. The percentage of degradation was determined using

$$\% \text{Degradation} = \frac{C_0 - C_t}{C_0} \times 100, \quad (1)$$

where C_0 is the initial concentration of PAA in mg/L and C_t is the concentration of PAA in mg/L at the end of experiment. The degree of mineralization was determined from Total Organic Carbon (TOC) analysis (in-house, based on HACH method).

2.3. Response Surface Methodology.

A central composite design (CCD) with four factors and five coded levels was adopted in the optimization study. Table 1 depicts the experimental ranges and levels of the process parameters. In the present study, the amount of ZnO loaded (A), initial concentration of PAA (B), solution pH (C), and reaction time (D) were selected as the independent variables.

TABLE 1: Independent variables and experimental range for degradation of PAA.

Parameters	Unit	Symbol	Range				
			-2	-1	0	+1	+2
ZnO loading	g/L	A	0.20	0.30	0.40	0.50	0.60
Initial concentration of PAA	mg/L	B	10.00	15.00	20.00	25.00	30.00
Solution pH		C	5.00	6.00	7.00	8.00	9.00
Reaction time	min	D	10.00	20.00	30.00	40.00	50.00

The percentage degradation of PAA (R) was selected as the output dependent variable. Other factors such as stirring rate, temperature, light intensity, and oxygen supply were held constant. The response variable was fitted by a highly structured and flexible second-order model:

$$R = \beta_o + \sum_{j=1}^k \beta_j x_j + \sum_{j=1}^k \beta_{jj} x_j^2 + \sum_{i < j=2}^k \beta_{ij} x_i x_j, \quad (2)$$

where R is the predicted degradation percentage of PAA (%), β_o is the constant term, β_j is the linear coefficients, β_{jj} is the quadratic coefficients, β_{ij} is the coefficient of the interaction parameters, and x_i and x_j represent the coded values of the independent variables [22–24]. The optimization study was performed using Design Expert software version 8.0.6 from Stat Ease Inc., USA.

3. Results and Discussion

3.1. Multivariate Regression Analysis. A total of 30 sets of batch experiments were carried out via CCD based on response surface methodology to investigate the interaction between the main and studied operational factors. Table 2 shows the experimental and predicted values of photocatalytic degradation of PAA under designed conditions. The adequacy of the model was further evaluated through analysis of variance (ANOVA) statistics (F -test, t -test, adjusted R^2 , and lack-of-fit) and the results are depicted in Table 3 [22]. The ANOVA of the derived response model indicates that the model is highly significant, as the F -value is 135.49 with p value < 0.0001 . This implies that there is only 0.01% chance that a Model F -value could occur due to noise. The lack-of-fit F -value of 1.75 confirms that the lack-of-fit is not significant. There is a 27.96% chance that a lack-of-fit F -value could occur because of noise. The nonsignificant lack-of-fit suggests that the model is precise enough for model prediction. The low coefficient of variation of 3.17 revealed high precision of the model and the experiment results are reliable. Meanwhile, the significance of the model is supported by its R^2 value of 0.9922 and adjusted R^2 value of 0.9848. The R^2 value should be close to 1, which implies that the experimental data fitted well with the model [25]. Adequate precision measures the signal to noise ratio, where a ratio greater than 4 is desirable. In this model, the value of 36.091 indicates an adequate signal, which can be used to navigate the design space. The coefficient of regression model and its significance for photocatalytic degradation of PAA is shown in Table 4.

In the photodecomposition of PAA, the operational parameters of the quadratic polynomial model terms of

B , C , D , A^2 , B^2 , C^2 , and D^2 are highly significant as their p value is less than 0.0001. Other model terms, namely, AC , AD , BC , BD , and CD , are insignificant as their p value is greater than 0.1000. It should be noted that the initial concentration of PAA has high negative effect compared to the positive effect of solution pH and reaction time. This suggested that the concentration of PAA plays a significant role in the photocatalytic decomposition of PAA [26]. Based on the experimental results presented in Table 4, a second-order polynomial equation was derived as shown in

$$\begin{aligned} R = & 82.74 - 2.07A - 10.38B + 4.30C + 6.69D \\ & + 1.73AB + 0.53AC - 0.18AD + 0.069BC \\ & - 0.15BD - 0.14CD - 10.42A^2 - 3.56B^2 \\ & - 6.43C^2 - 2.08D^2, \end{aligned} \quad (3)$$

where R is the percentage degradation of PAA and A , B , C , and D are terms for the coded values of amount of ZnO loaded, initial concentration of PAA, solution pH, and reaction time, respectively. The correlation between the experimental data against the values predicted by the response for the photodecomposition of PAA is shown in Figure 2. It can be seen that the values obtained via experimental approach were in good agreement with the predictive results ($R^2 = 0.9922$), indicating that the model is adequate to explain the experimental ranges. Subsequently, residuals analysis (difference between the actual values and predictive values) was carried out to examine the adequacy of the model, as inadequate fit would give inaccurate or misleading results [27, 28]. The plot of normal probability versus studentized residuals is illustrated in Figure 3. From Figure 3, all the residuals fall near to a straight line, indicating nonnormality of the experimental data [29]. In the plot of studentized residuals against predicted responses (Figure 4), all the points are randomly scattered within ± 3.00 , implying that the model is adequate to explain the relationship between the studied operational parameters and the degradation efficiency of PAA [30].

3.2. Response Surface Analysis. Figure 5 shows the interaction effects of amount of ZnO loaded, initial concentration of PAA, pH of the solution, and irradiation duration on the degradation efficiency of PAA. From the contour plot, it can be seen that the removal of PAA increased with increasing ZnO loaded up to 0.4 g/L and then gradually decreased at higher loadings. When the amount of ZnO increases above its optimum mass, the penetration of UV light into the reaction

TABLE 2: Central composite design with predictive values and their experimental results.

Standard	Point type	Experimental parameters				PAA degradation	
		ZnO loading (g/L)	Initial concentration of PAA (mg/L)	Solution pH	Reaction time (min)	Experimental (%)	Predictive (%)
1	Factorial	0.30	15.00	6.00	20.00	63.13	63.58
2	Factorial	0.50	15.00	6.00	20.00	54.68	55.27
3	Factorial	0.30	25.00	6.00	20.00	40.72	39.52
4	Factorial	0.50	25.00	6.00	20.00	35.59	38.14
5	Factorial	0.30	15.00	8.00	20.00	71.73	71.27
6	Factorial	0.50	15.00	8.00	20.00	63.36	65.60
7	Factorial	0.30	25.00	8.00	20.00	45.64	47.49
8	Factorial	0.50	25.00	8.00	20.00	47.66	48.21
9	Factorial	0.30	15.00	6.00	40.00	78.24	77.90
10	Factorial	0.50	15.00	6.00	40.00	68.37	68.88
11	Factorial	0.30	25.00	6.00	40.00	52.58	53.24
12	Factorial	0.50	25.00	6.00	40.00	50.47	51.14
13	Factorial	0.30	15.00	8.00	40.00	85.22	85.03
14	Factorial	0.50	15.00	8.00	40.00	76.71	78.12
15	Factorial	0.30	25.00	8.00	40.00	61.03	60.64
16	Factorial	0.50	25.00	8.00	40.00	58.74	60.65
17	Axial	0.20	20.00	7.00	30.00	44.12	45.22
18	Axial	0.60	20.00	7.00	30.00	40.58	36.92
19	Axial	0.40	10.00	7.00	30.00	89.82	89.27
20	Axial	0.40	30.00	7.00	30.00	49.76	47.75
21	Axial	0.40	20.00	5.00	30.00	49.09	48.43
22	Axial	0.40	20.00	9.00	30.00	67.53	65.63
23	Axial	0.40	20.00	7.00	10.00	62.77	61.04
24	Axial	0.40	20.00	7.00	50.00	88.65	87.81
25	Center	0.40	20.00	7.00	30.00	80.16	82.74
26	Center	0.40	20.00	7.00	30.00	83.22	82.74
27	Center	0.40	20.00	7.00	30.00	83.05	82.74
28	Center	0.40	20.00	7.00	30.00	81.55	82.74
29	Center	0.40	20.00	7.00	30.00	85.02	82.74
30	Center	0.40	20.00	7.00	30.00	83.41	82.74

TABLE 3: ANOVA for the response surface quadratic model.

Source	Sum of squares	DF	Mean square	F value	p value	
Model	7981.60	14	570.11	135.49	<0.0001	Significant
Residual	63.12	15	4.21			
Lack-of-fit	49.07	10	4.91	1.75	0.2796	Not significant
Pure error	14.05	5	2.81			
	$R^2 = 0.9922$		Adj. $R^2 = 0.9848$			
	C.V. = 3.17		Adeq. precision = 36.091			

medium was reduced due to screening effect [31]. The decrement in the photodegradation efficiency may also result from the particle agglomeration, which reduces the active sites on the ZnO catalysts that have been exposed to UV illumination [32]. It is obvious that the degradation percentage decreased as the initial concentration of PAA increased. This is based

on the fact that, as the concentration of PAA increases, the demand of oxidizing species such as $\cdot\text{OH}$ and $\cdot\text{O}_2^-$ also increases in order to photodegrade more molecules of PAA that adsorbed on the catalyst surface. However, the number of hydroxyl radicals available on the catalyst surface is insufficient to photodegrade PAA at higher concentrations as

TABLE 4: Coefficient of regression model and its significance.

Factor	Coefficient estimate	Degree of freedom	Standard error	F value	95% confidence interval low	95% confidence interval high	p value
Intercept	82.74	1	0.84	—	80.95	84.52	—
A	-2.07	1	0.42	24.55	-2.97	-1.18	0.0002
B	-10.38	1	0.42	614.58	-11.27	-9.49	<0.0001
C	4.30	1	0.42	105.44	3.41	5.19	<0.0001
D	6.69	1	0.42	255.43	5.80	7.58	<0.0001
AB	1.73	1	0.51	11.39	0.64	2.82	0.0042
AC	0.53	1	0.51	1.05	-0.57	1.62	0.3216
AD	-0.18	1	0.51	0.12	-1.27	0.91	0.7332
BC	0.069	1	0.51	0.018	-1.02	1.16	0.8942
BD	-0.15	1	0.51	0.088	-1.24	0.94	0.7712
CD	-0.14	1	0.51	0.074	-1.23	0.95	0.7895
A ²	-10.42	1	0.39	707.31	-11.25	-9.58	<0.0001
B ²	-3.56	1	0.39	82.46	-4.39	-2.72	<0.0001
C ²	-6.43	1	0.39	269.23	-7.26	-5.59	<0.0001
D ²	-2.08	1	0.39	28.11	-2.91	-1.24	<0.0001

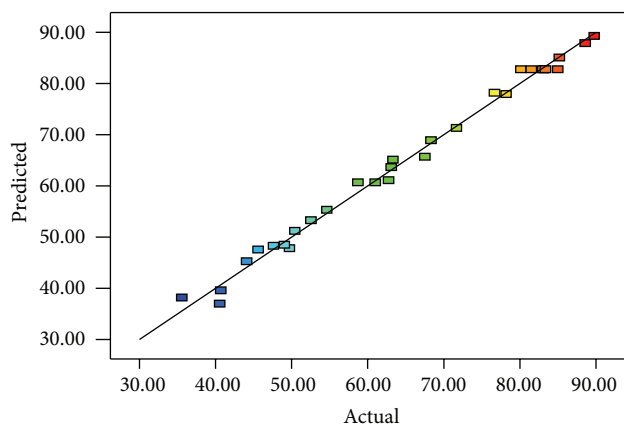


FIGURE 2: Predicted versus experimental values for photocatalytic degradation of PAA.

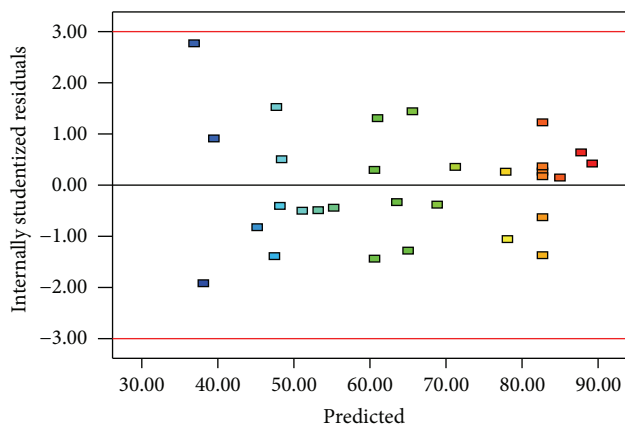


FIGURE 4: Plot of the residuals against the predicted response.

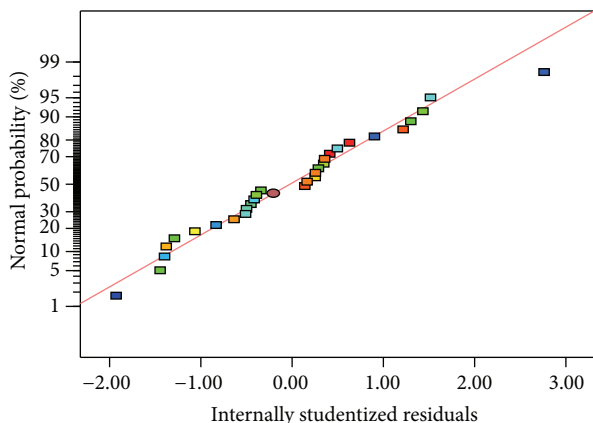


FIGURE 3: Normal probability plots of the residuals.

the amount of catalyst loaded, light intensity, and irradiation duration are fixed [33]. The rapid formation of degraded products during the photocatalytic reaction may compete for the hydroxyl radicals at higher concentration of PAA, which reduces the photodegradation efficiency as well [34]. It has been reported that the pH of the reaction medium has an impact on the electrostatic interaction between a catalyst surface, solvent molecules, substrate, and charged radicals formed during the photodegradation process [35]. The protonation and deprotonation of PAA molecules and ZnO catalyst surface could occur either in acidic or in alkaline conditions. Therefore, the ZnO surface is positively charged below 9.0 and the surface of PAA is negatively charged above 3.12 (pK_a of PAA = 3.12). Hence, optimum photodegradation efficiency was observed at $pK_a < pH < pH_{zpc}$. This is due to the electrostatic interaction enhancement between the positively charged ZnO surface and the negatively

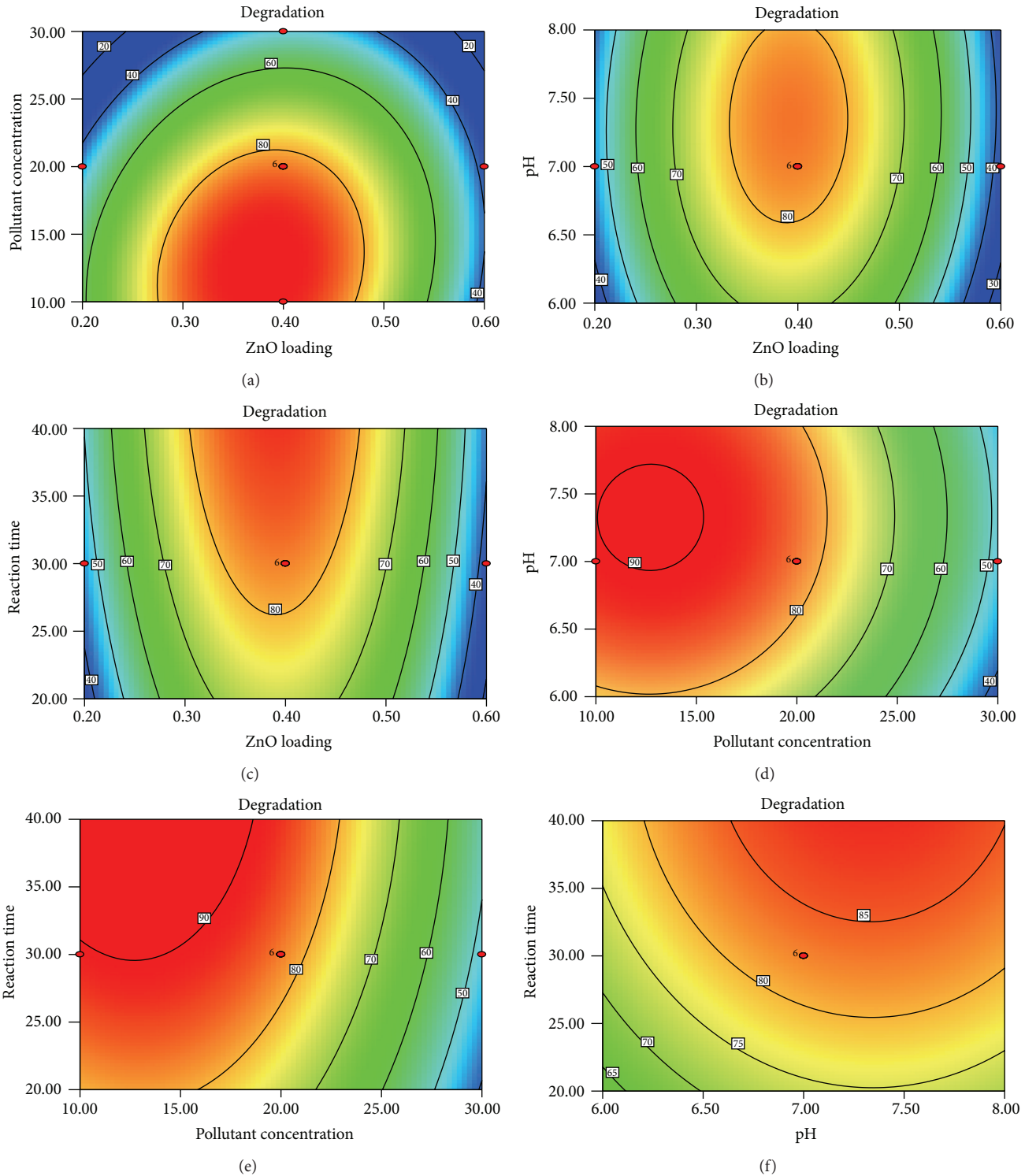


FIGURE 5: Interaction effects between studied parameters on the photodecomposition of PAA.

charged of PAA, which increased the photodegradation efficiency [36, 37]. The duration of exposure to UV irradiation also played a significant role in photodegrading PAA. The percentage of degradation increased with longer exposure duration, due to more photoinduced holes, and hydroxyl radicals will be generated, which facilitates the removal of PAA molecules [38].

3.3. Model Verification and Confirmation Test. The goal of a photocatalytic degradation reaction is to achieve greater degradation efficiency. Table 5 lists the optimization goal of each of the studied independent variables. Consequently, 5 sets of experiments were carried out to verify the derived response surface model according to the Design Expert software and the experimental and predictive results were

TABLE 5: The optimization goals of photocatalytic degradation of PAA.

Independent variables	Goal	Lower limit	Upper limit	Importance
ZnO loading (g/L)	In the range	0.30	0.50	3
Initial concentration of PAA (mg/L)	In the range	15.00	25.00	3
Solution pH	In the range	6.00	8.00	3
Reaction time (min)	In the range	20.00	40.00	3

TABLE 6: Comparison between experimental and predictive values for model verification.

Run	ZnO loading (g/L)	Initial concentration of PAA (mg/L)	Initial solution pH	Reaction time (min)	Experimental (%)	Predictive (%)
1	0.40	17.00	7.93	39.00	89.54	90.13
2	0.40	17.00	7.12	36.00	90.36	90.45
3	0.40	19.00	7.21	39.00	90.15	89.92
4	0.40	16.00	6.73	40.00	92.29	91.47
5	0.40	15.00	7.01	32.00	90.78	90.49

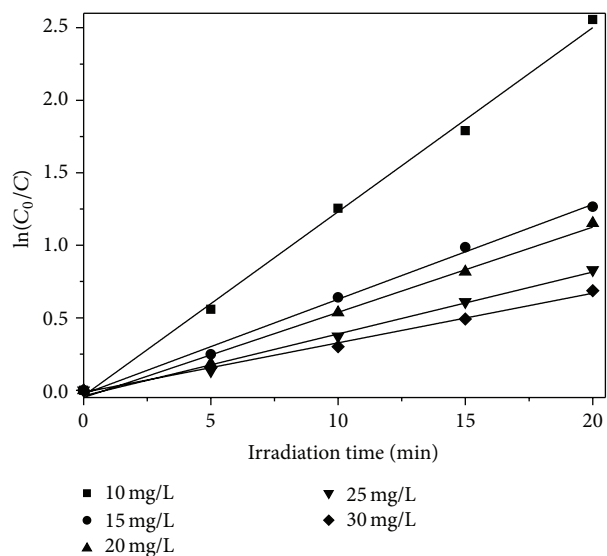


FIGURE 6: Kinetic plot of PAA by ZnO photocatalyst under UV-A irradiation.

shown in Table 6. As shown in Table 6, the experimental values were very close to the results predicted by the response surface software, which indicated that the developed model was reliable in optimizing the photocatalytic degradation of PAA.

3.4. Kinetics Analysis and Total Organic Carbon Removal of PAA. The Langmuir-Hinshelwood (L-H) kinetic model was used to describe the photocatalytic degradation rate of PAA by plotting the graph of $\ln(C/C_0)$ versus time, t , at different concentrations [39]:

$$\ln \frac{C_0}{C} = k_1 t, \quad (4)$$

where C_0 is the initial concentration of PAA (mg/L), C is the PAA concentration after irradiation at time, t , and k_1 is the pseudo-first-order rate constant. The pseudo-first-order rate constant was determined from the slope of the straight line (Figure 6). It is noteworthy that PAA with

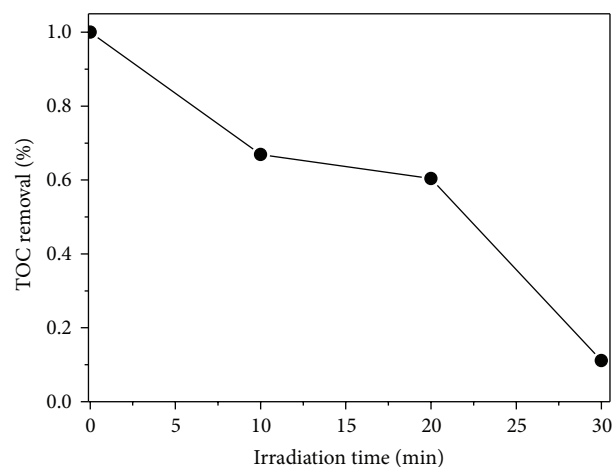


FIGURE 7: Effect of ZnO photocatalyst and UV irradiation on TOC removal in the photocatalytic degradation of PAA.

the lowest concentration (10 mg/L) exhibits the highest reaction rate (0.127 min^{-1}), which is about 2 times greater than that of 20 mg/L PAA. The reaction rate is decreased at higher concentrations. Figure 7 shows that 90% TOC removal was achieved on the photocatalytic degradation of PAA with ZnO photocatalysts under UV-A irradiation over 30 min, indicating photomineralization of PAA under UV/ZnO system.

3.5. Proposed Photocatalytic Degradation of PAA by UV/ZnO System. The photocatalytic reactions were initiated when the ZnO particle absorbs photons from UV or visible light. Upon the absorption of light, the electrons in the valence band (VB) of ZnO are promoted to the conduction band (CB), forming a positive hole in the valence band (h_{VB}^+). The photo-generated holes and electrons are able to induce oxidation-reduction reaction of the PAA molecules. However, the rapid recombination of the electron-hole pairs which dissipates in the form of heat will slow down the photocatalytic degradation process. The presence of oxygen in the aqueous solution helps in forming the superoxide radicals (O_2^-), which will

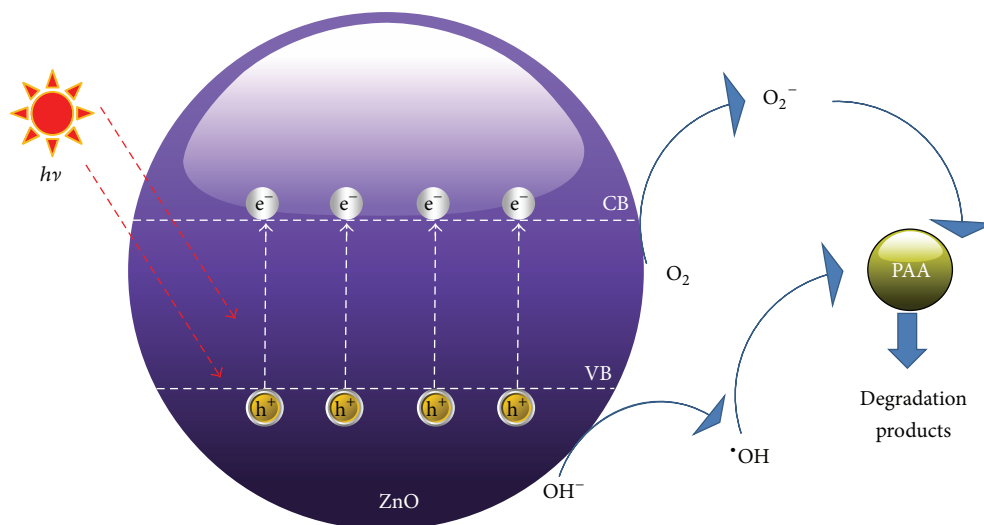
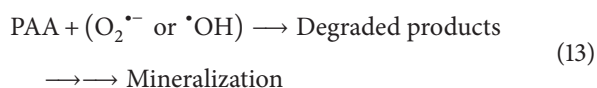
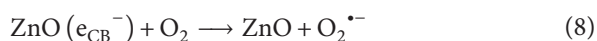
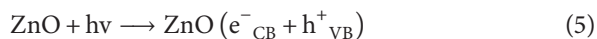


FIGURE 8: Schematic diagram of PCO of PAA by ZnO photocatalyst under UV irradiation.

then further protonate to hydroperoxyl radicals (HOO^\bullet). Both superoxide and hydroperoxyl radicals act as electron scavengers to trap the electrons from the conduction band of ZnO, which in turn delay the recombination process. The superoxide and hydroxyl radicals will then react with the PAA molecules and lead to the partial or complete mineralization of PAA ((5)–(13)) [40–42]. The schematic diagram of PCO of PAA by ZnO photocatalyst under UV irradiation was shown in Figure 8. Consider



4. Conclusion

In summary, the PCO of PAA was carried out by ZnO photocatalyst under UV-A irradiation. Modelling of PAA photodegradation was performed via CCD coupled with RSM. The derived response surface model successfully optimized four process parameters, namely, amount of ZnO loaded, initial concentration of PAA, pH of the solution, and irradiation duration. More than 90% of PAA was degraded

under optimized conditions of 0.04 g ZnO loaded, 16 mg/L PAA, and solution pH of 6.73 in 40 minutes. In this study, the initial concentration of PAA was the most significant factor that affects the photodegradation of PAA.

Conflict of Interests

The authors declare that there is no conflict of interests regarding the publication of this paper.

Acknowledgment

The authors would like to thank University of Malaya for funding this research work under University of Malaya Research Grant (UMRG: RP022-2012A).

References

- [1] H. Mestankova, B. Escher, K. Schirmer, U. von Gunten, and S. Canonica, "Evolution of algal toxicity during (photo)oxidative degradation of diuron," *Aquatic Toxicology*, vol. 101, no. 2, pp. 466–473, 2011.
- [2] S. Sanches, M. T. Barreto Crespo, and V. J. Pereira, "Drinking water treatment of priority pesticides using low pressure UV photolysis and advanced oxidation processes," *Water Research*, vol. 44, no. 6, pp. 1809–1818, 2010.
- [3] C. Tizaoui, K. Mezughi, and R. Bickley, "Heterogeneous photocatalytic removal of the herbicide clopyralid and its comparison with UV/H₂O₂ and ozone oxidation techniques," *Desalination*, vol. 273, no. 1, pp. 197–204, 2011.
- [4] S. P. Kamble, S. B. Sawant, and V. G. Pangarkar, "Photocatalytic mineralization of phenoxyacetic acid using concentrated solar radiation and titanium dioxide in slurry photoreactor," *Chemical Engineering Research and Design*, vol. 84, no. 5, pp. 355–362, 2006.
- [5] H. M. Badawi, "DFT versus Møller-Plesset conformational profile and vibrational assignments of non-planar phenoxyacetic

- acid and 2,3,4,5,6- pentafluorophenoxyacetic acid,” *Journal of Molecular Structure*, vol. 977, no. 1–3, pp. 67–71, 2010.
- [6] H. M. Badawi and W. Förner, “Analysis of the infrared and Raman spectra of phenylacetic acid and mandelic (2-hydroxy-2-phenylacetic) acid,” *Spectrochimica Acta—Part A: Molecular and Biomolecular Spectroscopy*, vol. 78, no. 3, pp. 1162–1167, 2011.
- [7] M. Shanthi and S. Kabilan, “Substituent and solvent effects on electronic spectra of some substituted phenoxyacetic acids,” *Spectrochimica Acta, Part A: Molecular and Biomolecular Spectroscopy*, vol. 67, no. 2, pp. 479–482, 2007.
- [8] K. Li, P. Zhang, L. Ge et al., “Concentration-dependent photodegradation kinetics and hydroxyl-radical oxidation of phenicol antibiotics,” *Chemosphere*, vol. 111, pp. 278–282, 2014.
- [9] M. Sánchez-Polo, M. M. A. Daiem, R. Ocampo-Pérez, J. Rivera-Utrilla, and A. J. Mota, “Comparative study of the photodegradation of bisphenol A by HO•, SO₄•⁻ and CO₃•⁻/HCO₃• radicals in aqueous phase,” *Science of the Total Environment*, vol. 463–464, pp. 423–431, 2013.
- [10] E. G. L. Oliveira, J. J. Rodrigues Jr., and H. P. de Oliveira, “Influence of surfactant on the fast photodegradation of rhodamine B induced by TiO₂ dispersions in aqueous solution,” *Chemical Engineering Journal*, vol. 172, no. 1, pp. 96–101, 2011.
- [11] I. Kim and H. Tanaka, “Photodegradation characteristics of PPCPs in water with UV treatment,” *Environment International*, vol. 35, no. 5, pp. 793–802, 2009.
- [12] R. C. Pawar, H. Kim, and C. S. Lee, “Defect-controlled growth of ZnO nanostructures using its different zinc precursors and their application for effective photodegradation,” *Current Applied Physics*, vol. 14, no. 4, pp. 621–629, 2014.
- [13] M. B. Akin and M. Oner, “Photodegradation of methylene blue with sphere-like ZnO particles prepared via aqueous solution,” *Ceramics International*, vol. 39, no. 8, pp. 9759–9762, 2013.
- [14] P. Shukla, I. Fatimah, S. Wang, H. M. Ang, and M. O. Tadé, “Photocatalytic generation of sulphate and hydroxyl radicals using zinc oxide under low-power UV to oxidise phenolic contaminants in wastewater,” *Catalysis Today*, vol. 157, no. 1–4, pp. 410–414, 2010.
- [15] S. Anandan, N. Ohashi, and M. Miyauchi, “ZnO-based visible-light photocatalyst: band-gap engineering and multi-electron reduction by co-catalyst,” *Applied Catalysis B: Environmental*, vol. 100, no. 3–4, pp. 502–509, 2010.
- [16] A. Rezaee, H. Masoumbeigi, R. D. C. Soltani, A. R. Khataee, and S. Hashemiyani, “Photocatalytic decolorization of methylene blue using immobilized ZnO nanoparticles prepared by solution combustion method,” *Desalination and Water Treatment*, vol. 44, no. 1–3, pp. 174–179, 2012.
- [17] M. A. Behnajady, N. Modirshahla, and R. Hamzavi, “Kinetic study on photocatalytic degradation of C.I. Acid Yellow 23 by ZnO photocatalyst,” *Journal of Hazardous Materials*, vol. 133, no. 1–3, pp. 226–232, 2006.
- [18] H. K. Singh, M. Saquib, M. M. Haque, M. Muneer, and D. W. Bahnemann, “Titanium dioxide mediated photocatalysed degradation of phenoxyacetic acid and 2,4,5-trichlorophenoxyacetic acid, in aqueous suspensions,” *Journal of Molecular Catalysis A: Chemical*, vol. 264, no. 1–2, pp. 66–72, 2007.
- [19] M. Trillas, J. Peral, and X. Domènech, “Photocatalyzed degradation of phenol, 2,4-dichlorophenol, phenoxyacetic acid and 2,4-dichlorophenoxyacetic acid over supported TiO₂ in a flow system,” *Journal of Chemical Technology and Biotechnology*, vol. 67, no. 3, pp. 237–242, 1996.
- [20] R. Das, S. Sarkar, and C. Bhattacharjee, “Photocatalytic degradation of chlorhexidine—a chemical assessment and prediction of optimal condition by response surface methodology,” *Journal of Water Process Engineering*, vol. 2, pp. 79–86, 2014.
- [21] A. H. Abdullah, H. J. M. Moey, and N. A. Yusof, “Response surface methodology analysis of the photocatalytic removal of Methylene Blue using bismuth vanadate prepared via polyol route,” *Journal of Environmental Sciences*, vol. 24, no. 9, pp. 1694–1701, 2012.
- [22] S.-P. Sun and A. T. Lemley, “p-Nitrophenol degradation by a heterogeneous Fenton-like reaction on nano-magnetite: process optimization, kinetics, and degradation pathways,” *Journal of Molecular Catalysis A: Chemical*, vol. 349, no. 1–2, pp. 71–79, 2011.
- [23] R. H. Myers and D. C. Montgomery, *Response Surface Methodology: Process and Product Optimization Using Designed Experiments*, John Wiley & Sons, New York, NY, USA, 2nd edition, 2002.
- [24] V. A. Sakkas, M. A. Islam, C. Stalikas, and T. A. Albanis, “Photocatalytic degradation using design of experiments: a review and example of the Congo red degradation,” *Journal of Hazardous Materials*, vol. 175, no. 1–3, pp. 33–44, 2010.
- [25] S. Chatterjee, A. Kumar, S. Basu, and S. Dutta, “Application of response surface methodology for methylene blue dye removal from aqueous solution using low cost adsorbent,” *Chemical Engineering Journal*, vol. 181–182, pp. 289–299, 2012.
- [26] C. Sahoo and A. K. Gupta, “Optimization of photocatalytic degradation of methyl blue using silver ion doped titanium dioxide by combination of experimental design and response surface approach,” *Journal of Hazardous Materials*, vol. 215–216, pp. 302–310, 2012.
- [27] R. Meng and X. Yu, “Investigation of ultrasound assisted regeneration of Ni-bentonite with response surface methodology (RSM),” *Applied Clay Science*, vol. 54, no. 1, pp. 112–117, 2011.
- [28] Y. J. Wen and Y. H. Wu, “Optimizing adsorption of Co(II) and Ni(II) by 13× molecular sieves using response surface methodology,” *Water, Air, and Soil Pollution*, vol. 223, no. 9, pp. 6095–6107, 2012.
- [29] F. Shahrezaei, Y. Mansouri, A. A. L. Zinatizadeh, and A. Akhbari, “Process modeling and kinetic evaluation of petroleum refinery wastewater treatment in a photocatalytic reactor using TiO₂ nanoparticles,” *Powder Technology*, vol. 221, pp. 203–212, 2012.
- [30] R. D. C. Soltani, A. Rezaee, A. R. Khataee, and M. Safari, “Photocatalytic process by immobilized carbon black/ZnO nanocomposite for dye removal from aqueous medium: optimization by response surface methodology,” *Journal of Industrial and Engineering Chemistry*, vol. 20, no. 4, pp. 1861–1868, 2014.
- [31] B. Gao, P. S. Yap, T. M. Lim, and T.-T. Lim, “Adsorption-photocatalytic degradation of Acid Red 88 by supported TiO₂: effect of activated carbon support and aqueous anions,” *Chemical Engineering Journal*, vol. 171, no. 3, pp. 1098–1107, 2011.
- [32] K. Hayat, M. A. Gondal, M. M. Khaled, S. Ahmed, and A. M. Shemsi, “Nano ZnO synthesis by modified sol gel method and its application in heterogeneous photocatalytic removal of phenol from water,” *Applied Catalysis A: General*, vol. 393, no. 1–2, pp. 122–129, 2011.
- [33] C. Lu, Y. Wu, F. Mai et al., “Degradation efficiencies and mechanisms of the ZnO-mediated photocatalytic degradation of Basic Blue 11 under visible light irradiation,” *Journal of Molecular Catalysis A: Chemical*, vol. 310, no. 1–2, pp. 159–165, 2009.
- [34] U. I. Gaya and A. H. Abdullah, “Heterogeneous photocatalytic degradation of organic contaminants over titanium dioxide:

- a review of fundamentals, progress and problems,” *Journal of Photochemistry and Photobiology C: Photochemistry Reviews*, vol. 9, no. 1, pp. 1–12, 2008.
- [35] M. Kosmulski, “pH-dependent surface charging and points of zero charge: III. Update,” *Journal of Colloid and Interface Science*, vol. 298, no. 2, pp. 730–741, 2006.
- [36] H. Zhu, R. Jiang, Y. Fu et al., “Effective photocatalytic decolorization of methyl orange utilizing TiO₂/ZnO/chitosan nanocomposite films under simulated solar irradiation,” *Desalination*, vol. 286, pp. 41–48, 2012.
- [37] C. Wang, J. Zhao, X. Wang et al., “Preparation, characterization and photocatalytic activity of nano-sized ZnO/SnO₂ coupled photocatalysts,” *Applied Catalysis B: Environmental*, vol. 39, no. 3, pp. 269–279, 2002.
- [38] M. Fathinia, A. R. Khataee, M. Zarei, and S. Aber, “Comparative photocatalytic degradation of two dyes on immobilized TiO₂ nanoparticles: effect of dye molecular structure and response surface approach,” *Journal of Molecular Catalysis A: Chemical*, vol. 333, no. 1–2, pp. 73–84, 2010.
- [39] K. V. Kumar, K. Porkodi, and F. Rocha, “Langmuir-Hinshelwood kinetics—a theoretical study,” *Catalysis Communications*, vol. 9, no. 1, pp. 82–84, 2008.
- [40] P. V. L. Reddy, K.-H. Kim, and H. Song, “Emerging green chemical technologies for the conversion of CH₄ to value added products,” *Renewable and Sustainable Energy Reviews*, vol. 24, pp. 578–585, 2013.
- [41] D. Zhang, X. Liu, and X. Wang, “Growth and photocatalytic activity of ZnO nanosheets stabilized by Ag nanoparticles,” *Journal of Alloys and Compounds*, vol. 509, no. 15, pp. 4972–4977, 2011.
- [42] A. Fujishima, X. Zhang, and D. A. Tryk, “TiO₂ photocatalysis and related surface phenomena,” *Surface Science Reports*, vol. 63, no. 12, pp. 515–582, 2008.

Review Article

A Review on the Low-Dimensional and Hybridized Nanostructured Diamond Films

Hongdong Li, Shaoheng Cheng, Jia Li, and Jie Song

State Key Lab of Superhard Materials, Jilin University, Changchun 130012, China

Correspondence should be addressed to Hongdong Li; hdli@jlu.edu.cn

Received 30 April 2015; Accepted 1 July 2015

Academic Editor: Jose Alvarez

Copyright © 2015 Hongdong Li et al. This is an open access article distributed under the Creative Commons Attribution License, which permits unrestricted use, distribution, and reproduction in any medium, provided the original work is properly cited.

In the last decade, besides the breakthrough of high-rate growth of chemical vapor deposited single-crystal diamonds, numerous nanostructured diamond films have been rapidly developed in the research fields of the diamond-based sciences and industrial applications. The low-dimensional diamonds of two-dimensional atomic-thick nanofilms and nanostructural diamond on the surface of bulk diamond films have been theoretically and experimentally investigated. In addition, the diamond-related hybrid nanostructures of n-type oxide/p-type diamond and n-type nitride/p-type diamond, having high performance physical and chemical properties, are proposed for further applications. In this review, we first briefly introduce the three categories of diamond nanostructures and then outline the current advances in these topics, including their design, fabrication, characterization, and properties. Finally, we address the remaining challenges in the research field and the future activities.

1. Introduction

Diamond has been deeply investigated and widely applied in numerous fields because of its unique properties of wide band gap, high thermal conductivity, hardness, good chemical stability, chemical inertness, high temperature stability, inherent biocompatibility, and so forth, which make it suitable for use in various high performance optoelectronic devices. In addition to conventional bulk diamond crystals (e.g., chemical vapor deposited (CVD) single crystal diamonds and polycrystalline diamond films), the fabrication and properties of diamond-related nanostructures have attracted a significant amount of interest [1]. Designing new nanostructures of diamond and exploiting novel properties become an important hot topic in current researches. With increasing the interest of two-dimensional (2D) graphene in the recent decade since 2004 [2], the atomic-thickness 2D diamond nanofilms without and with surface functional terminations have emerged [3–7]. These nanofilms have smaller band gaps and varying magnetic properties with respect to those of the bulk diamond, which are strongly dependent on layer number (n) and surface functionalizations. This new category of diamond has been constructed, though the most researches are based on theoretical calculations thus far. The other

low-dimensional nanodiamonds (e.g., nanowires, nanopits, and nanotips) have been experimentally generated by “top-down” approach [8, 9] on the surface of bulk single-crystal diamonds and/or polycrystalline diamond films and show some excellent optical, electronic, and biological properties. The third category of heterojunction structures consists of various nanosized semiconducting materials and bulk polycrystalline diamond films (single-crystal diamonds), which are favorable for achieving high performance optoelectronic devices. The nanosized materials are generally of n-type metallic compounds (such as zinc oxide ZnO [10, 11], titania TiO₂ [12], and gallium nitride GaN [13]) deposited on the p-type diamond. In this review, we discuss and summarize the recent developments of fabrications, characterizations, properties, and potential applications based on the above three diamond-related topics. These works in the recent 10 years will be beneficial to the future development of diamond material with more novel structures and better properties for applications.

2. Two-Dimensional Diamond Nanofilms

In recent decades, besides the conventional bulk carbonaceous materials (i.e., graphite, diamond, and disordered

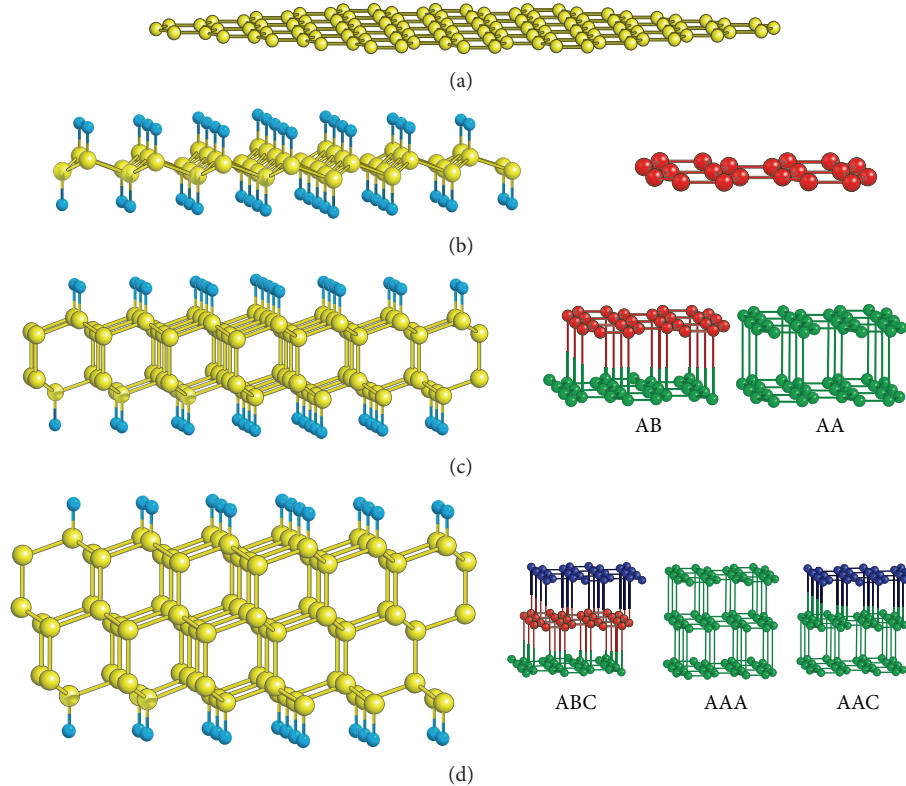


FIGURE 1: Atomic geometry of the studied two-dimensional (2D) carbon nanofilms: (a) graphene; (b) graphane; (c) diamane of two layers; and (d) diamane of three layers. Carbon (hydrogen) atoms are marked with yellow (blue). For each diamane, possible stacking sequences of carbon layers are presented on the right side [19].

carbon), various new nanostructures (such as fullerene [14], carbon nanotubes [15], graphene [2], and diamond clusters [16]) have appeared in the family of carbon. In 2007, full hydrogenation on both sides of graphene (with C_xH_x), referred to as “graphane,” was theoretically predicted [5], and this configuration with buckling feature is similar to that of hydrogenated diamond (111) planes. Chernozatonskii et al. considered a C_2H nanostructure [6] based on bilayer graphene to constitute a 2D hydrogenated (111) diamond film with a thickness of less than 1 nm, which is called “diamane.” It was theoretically demonstrated that C_2H diamane is more stable than CH graphane. Both hydrogenated diamond-like films (graphane and diamane) have relatively wide band gaps narrower than that of bulk diamond within 1 eV [5, 17, 18]. These early works open up a new research area of low dimensional diamond. Figure 1 shows the atomic geometry of the 2D carbon nanofilms [19]. The authors summarized the calculated formation energy and band gap width of different hydrocarbon structures as a function of hydrogen content.

Zhu et al. investigated the layer number (n) dependent formation and electronic properties of hydrogenated 2D diamond nanofilms originated from few-layer graphene [3]. The band gap monotonically decreases with the increasing thickness (i.e., n), reflecting a quantum confinement effect (Figure 2(a)). Due to the presence of hydrogen passivated surface, the tunable gaps are localized in a region lower than that of bulk diamond. Based on building blocks of C_{35} and C_{84}

with octahedral morphology, Li and Zhao [7] described the structurally optimized few-layer (six-layer) 2D diamond-related nanostructure (nanoflake) having a diamond matrix covered with graphite fragments. As shown in Figure 3, the two outmost layers were delaminated and partially graphitized having a nonsymmetrical reconstruction. It revealed that the stability of these 2D diamond nanofilms generally requires termination with functional groups or reconstructive sp^2 -carbon surface.

Different from the previous first-principles calculations based on few-layer graphene and building blocks of carbon clusters, Li et al. [4] performed n -dependent structural optimization of 2D diamond nanofilms (Figure 4) beginning from the original diamond (111) layers without termination of foreign atoms, cleaved from bulk cubic diamond with single-dangling-bond surface. At $n \leq 5$, the films are relaxed into a few graphene layers, whereas for $6 \leq n \leq 11$, a gradient-graphite-diamond-like (GGDL) structure with gradient changes of interplanar spacing and buckling feature is predicted. A threshold $n = 12$ is determined to realize the thinnest two-dimensional (111)-oriented diamond film. For $n \geq 12$, the diamond phase is energetically stabilized. The effects of semihydrogenation (SH) and full hydrogenation (FH) on the structural evolution and properties of 2D diamond nanofilms were further investigated [20]. Both of the hydrogenation processes play an important role in stabilizing the 2D diamond structures. Interestingly, for the SH cases,

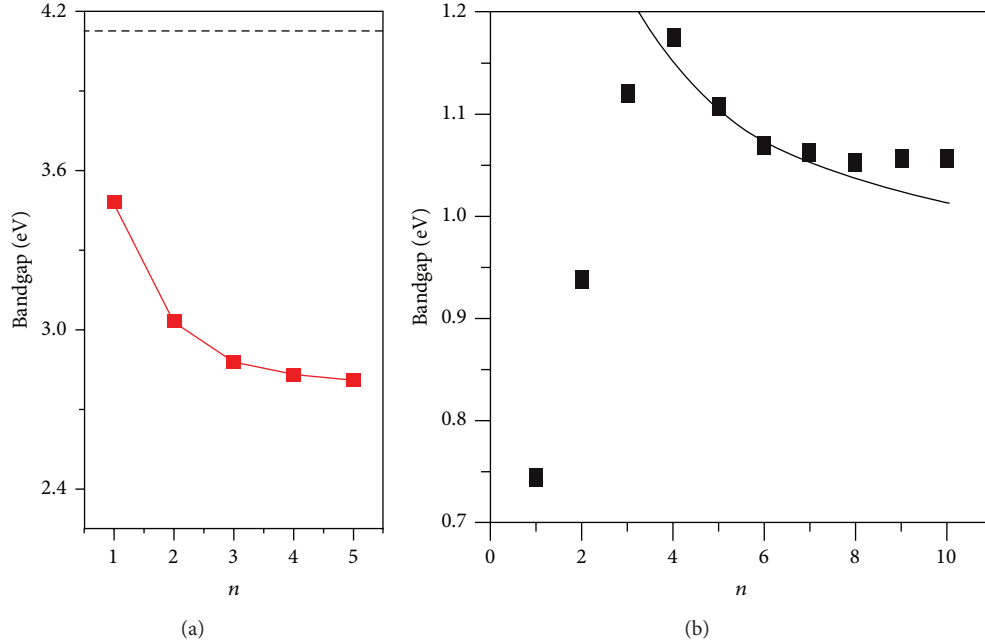


FIGURE 2: (a) Band gaps of fully hydrogenated two-dimensional (2D) cubic diamond nanofilms as a function of layer number (n). The dashed line corresponds to the band gap of bulk diamond [3]. (b) Band gaps of semihydrogenated 2D diamond nanofilms as a function of n . The solid line represents the fitted curve [20].

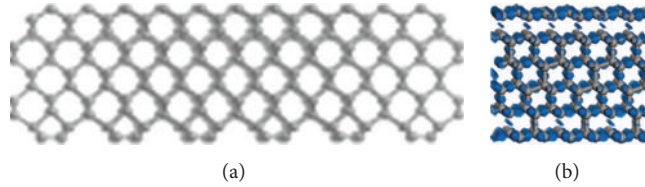


FIGURE 3: The initial structure (a) and the deformation electron density picture (b) for the two-dimensional (2D) diamond nanoflakes with 6 layers after structural geometry optimization generated from cuboctahedral nanodiamond C_{142} as the building block [7].

the spin-related band gaps are in an infrared region of 0.74–1.17 eV (Figure 2(b)), and a ferrimagnetism characteristic is presented determined by the unpaired electrons on the outmost 3 layers on nonhydrogenated side (Figure 5) which are strongly dependent on n . Layer-by-layer partial density of states (PDOS) revealed that the carbons with dangling bonds near the surface determine the tuning electronic and magnetic properties of 2D diamond nanofilms [4, 20].

For the novel ultrathin diamond nanofilms, it is desirable to know how defects and dopants can tune the corresponding electronic properties. Fyta [21] recently theoretically investigated the electronic structure of diamane by introducing dopants of boron, nitrogen, sulfur atoms, and defects of nitrogen vacancy (NV) with different charged states. As a general remark (summarized in Table 1), adding dopants or defects closes the energy gap of ideal diamane films as these provide available electronic states within that gap. The amount of band gap reduction is associated with the chosen dopants or the charge state of the NV defect. Adding a dopant with a large size mismatches to the lattice and leads to a tendency to stabilize the doping atoms at surface, and, accordingly, the electrons are localized around the dopant

TABLE 1: Bond lengths (in Å), the HOMO-LUMO gap (E_g , in eV), and the relative difference (in %) of this gap with respect to that of the ideal diamane film (E_g^0) for different diamane films [21].

Structure	$r_b^{(1,2)}$	$r_b^{(1,3)}$	$r_b^{(1,4)}$	$r_b^{(1,5)}$	$r_b^{(CH)}$	E_g	$\Delta E_g/E_g^0$
diam	1.550	1.534	1.532	1.533	1.126	4.05	
N-diam	1.554	1.523	1.523	1.523	1.136	3.99	1.5
B-diam	1.613	1.620	1.620	1.563	1.130	3.71	8.4
S-diam	2.901	1.793	1.792	1.792	1.130	1.40	65.4
NV ⁰ -diam		1.452	1.457	1.452	1.144	0.67	83.4
NV ⁻ -diam		1.447	1.447	1.447	1.151	0.61	84.9
NV ⁺ -diam		1.458	1.457	1.459	1.140	0.95	76.5
vac-diam		1.536	1.624	1.536	1.117	1.40	65.4

site. Furthermore, the spins of these NV centers in diamane close to the surface could prove much more efficiency than NV center in bulk diamond in nanomagnetic resonance imaging (nano-MRI) applications. The results are relevant to potential applications of diamane films in nanoelectronics.

Besides the calculations, finding a possible fabrication route of scaled 2D diamond nanofilms is more necessary for

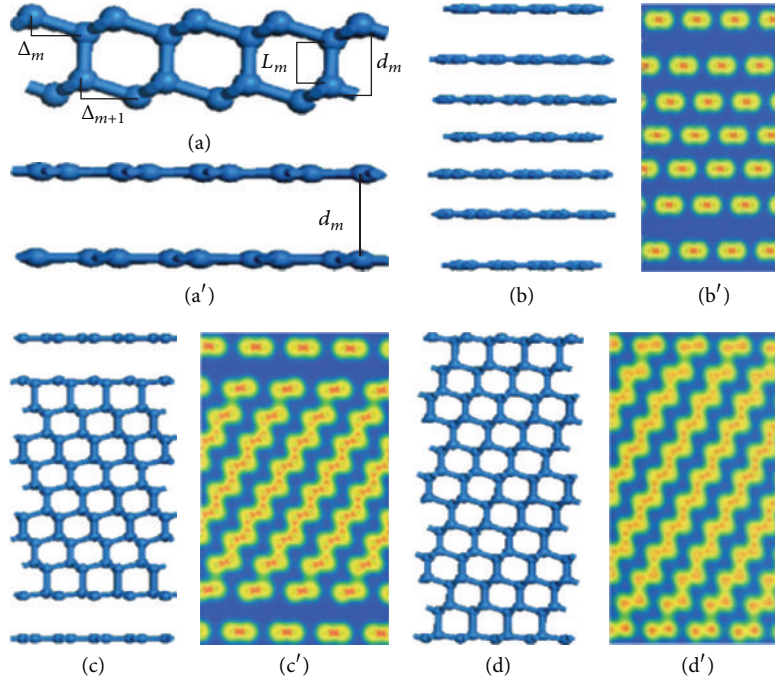


FIGURE 4: Structural evolution from original two-dimensional (2D) atomically few layer diamonds. The side views of the optimized configurations and the corresponding electronic charge density features for the cases of $n = 2$ (a, a'), $n = 7$ (b, b'), $n = 11$ (c, c'), and $n = 12$ (d, d'), respectively. The thicknesses are normalized [4].

the practical application. Li et al. [4, 20] pointed out possible routes to experimentally realize the freestanding layered 2D diamond by laser ablation from bulk diamond and/or find these nanosized diamond layers from ball milling and detonation products. CVD technique is a suitable method to obtain mass products of the atomically thin diamond films. To obtain the hydrogenated diamond films, treating in H_2 ambient (at high temperature and/or in H_2 plasma) for 2D pure nanofilms or transition from hydrogenated few-layer graphene under high pressure might be feasible. Through the first-principles density functional theory calculations, Odkhuu et al. [22] investigated the transformation of a few layers of graphene (with hydrogenation or fluorination on the outer surface of the top graphene layer) into sp^3 -bonded thin overlayers (also named as diamond-like layer) on metallic surfaces (Co, Ni, and Cu) (Figure 6). Strong hybridization between the sp^3 dangling bonds orbitals and the metallic surface d_z^2 orbitals stabilizes the sp^3 -bonded carbon layers. And, it was speculated that the metal/ sp^3 carbon interfaces might be a new candidate for superconductivity study. The computational results suggest a route to experimental realization of large-area ultrathin sp^3 -bonded carbon films on metal surfaces.

Most recently, Kvashnin et al. [23] further theoretically demonstrated that few-layer graphene can undergo phase transformation into thin diamond film under reduced or no pressure, if the process is facilitated by hydrogenation of the surfaces. Such a “chemically induced phase transition” is inherently nanoscale phenomenon, when the surface conditions directly affect thermodynamics, and the transition

pressure depends greatly on film thickness. The role of finite diameter of graphene flakes and possible formation of the diamond films with the (110) surface was described. Later, Antipina and Sorokin [24] used H, H_2 , F, F_2 , H_2O , and NH_3 as the adsorbates to produce high-quality films of diamond from few-layer graphene at different temperatures and pressures by ab initio calculations. The functionalized cubic or hexagonal diamond films with specific surface would show well-defined properties.

Summarily, the above results underline the strong differences of the structures and properties of those atomically thick 2D diamond nanofilms compared to bulk diamond, and these should have implications in various potential nanoelectrical applications.

3. Nanostructural Surface of Bulk Diamond Film

As diamond is an important material for its outstanding properties in many aspects, fabrication of micro/nanodiamond (films) is essential to enhance the intrinsic properties and to find new properties for fully realizing the potentials of diamond in numerous research fields. The designs of forming diamond micrometer- and nano-structures generally include two approaches of “bottom-up” and “top-down”. In this review, we focus on the “top-down” method that has widely been applied because of its controllability, variety, and large area. Up to now, various top-down nanofabrication techniques have been explored for well-designed diamond nanostructures [8, 9, 25–37].

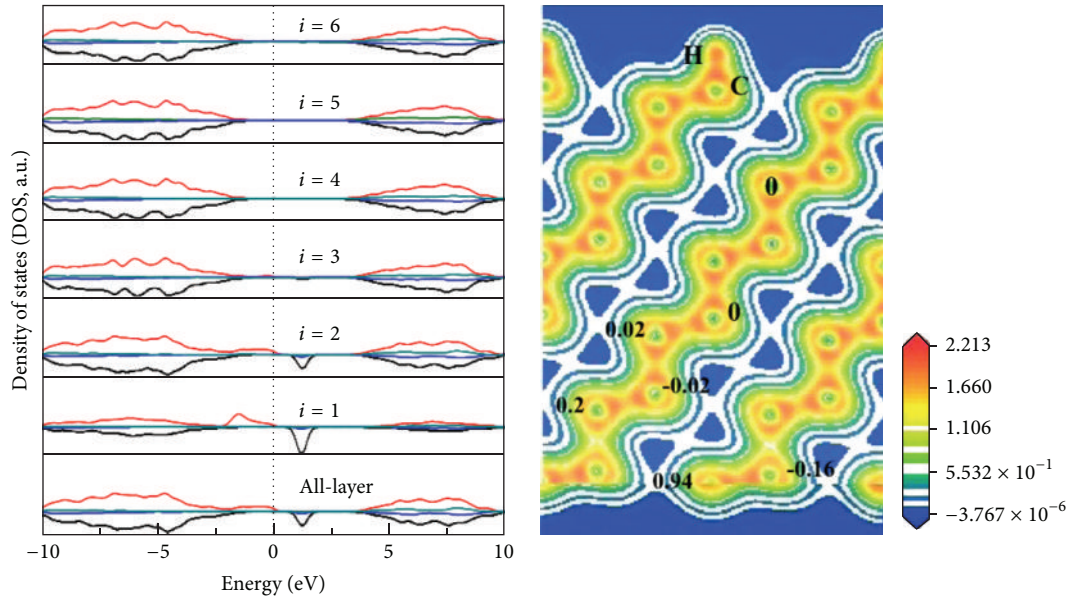


FIGURE 5: Partial density of states (PDOS) and spin density picture of the calculated semihydrogenated two-dimensional (2D) diamond nanofilm with $n = 6$. Layer-by-layer PDOS ($i = 1$ to 6) are taken from the outmost layer on one side to the opposite side in turn. The red (green) and black (blue) lines are corresponding PDOS of p (s)-orbital electrons with spin-up and spin-down, respectively. The Fermi level is set to 0 eV. The intensities of the total and partial DOS are normalized. The pictures of spin density are labeled with the corresponding magnetic moments around the atoms [20].

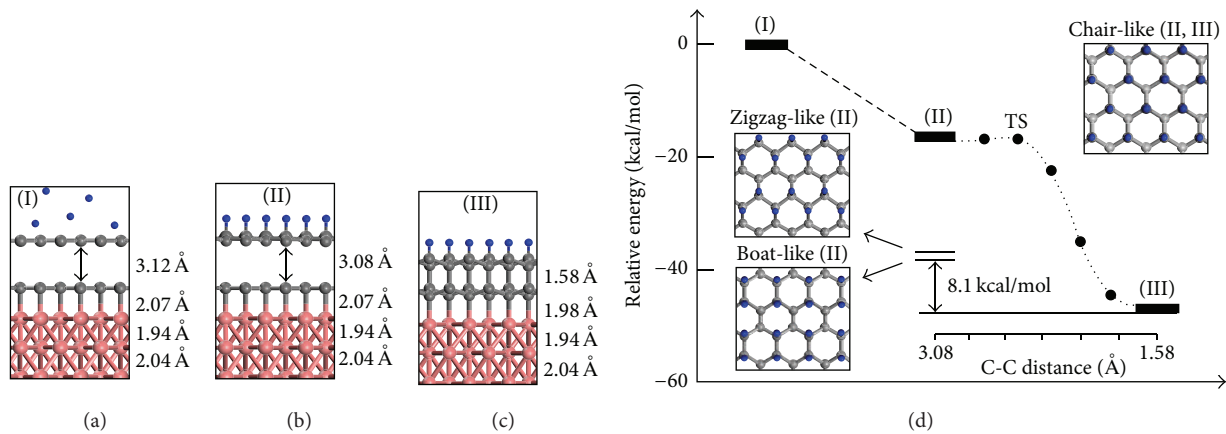


FIGURE 6: The energetics of conversion of bilayer graphene into sp^3 carbon film on metal surface. For details see [22].

In 1997, Shiomi [8] realized nanosized columnar structure from polycrystalline diamond films by reactive ion etching (RIE) in O_2/CF_4 plasma and the examined electron field emission characteristics were improved, which triggered activities of fabricating nanostructures on diamond films. Masuda et al. (in 2000 [9]) introduced ordered through-hole anodic porous alumina membranes employed on top of both undoped and boron-doped p-type CVD diamond films and then fabricated nanohoneycomb diamond film using a radio-frequency driven (at 13.56 MHz) oxygen plasma etching treatment (Figure 7). Fine structures with a high degree of ordering can be obtained over large areas ($\sim 1 \text{ cm}^2$) controlled by changing the geometrical structure of the porous alumina membrane mask. The through holes in the masks have

high aspect ratios (depth-to-diameter) compared to those used in conventional lithography. Using the nanohoneycomb diamond as electrodes, it is found that the capacitance values increased depending on the pore dimensions, and a film of pore diameter 400 nm and pore depth $3 \mu\text{m}$ exhibited a 400-fold increase in the capacitance ($3.91 \times 10^{-3} \text{ F cm}^{-2}$) in comparison to an as-deposited surface film (Figure 7(c)) [25].

By depositing gold nanodots as etching masks on the as-grown polycrystalline nanodiamond (ND) and microdiamond (MD) films, Zou et al. (in 2008 [26]) fabricated high-density uniform diamond nanopillar arrays by employing bias-assisted RIE in a hydrogen/argon plasma (Figure 8). The formation of nanopillar structure is associated with the directional physical etching/sputtering by ion bombardment

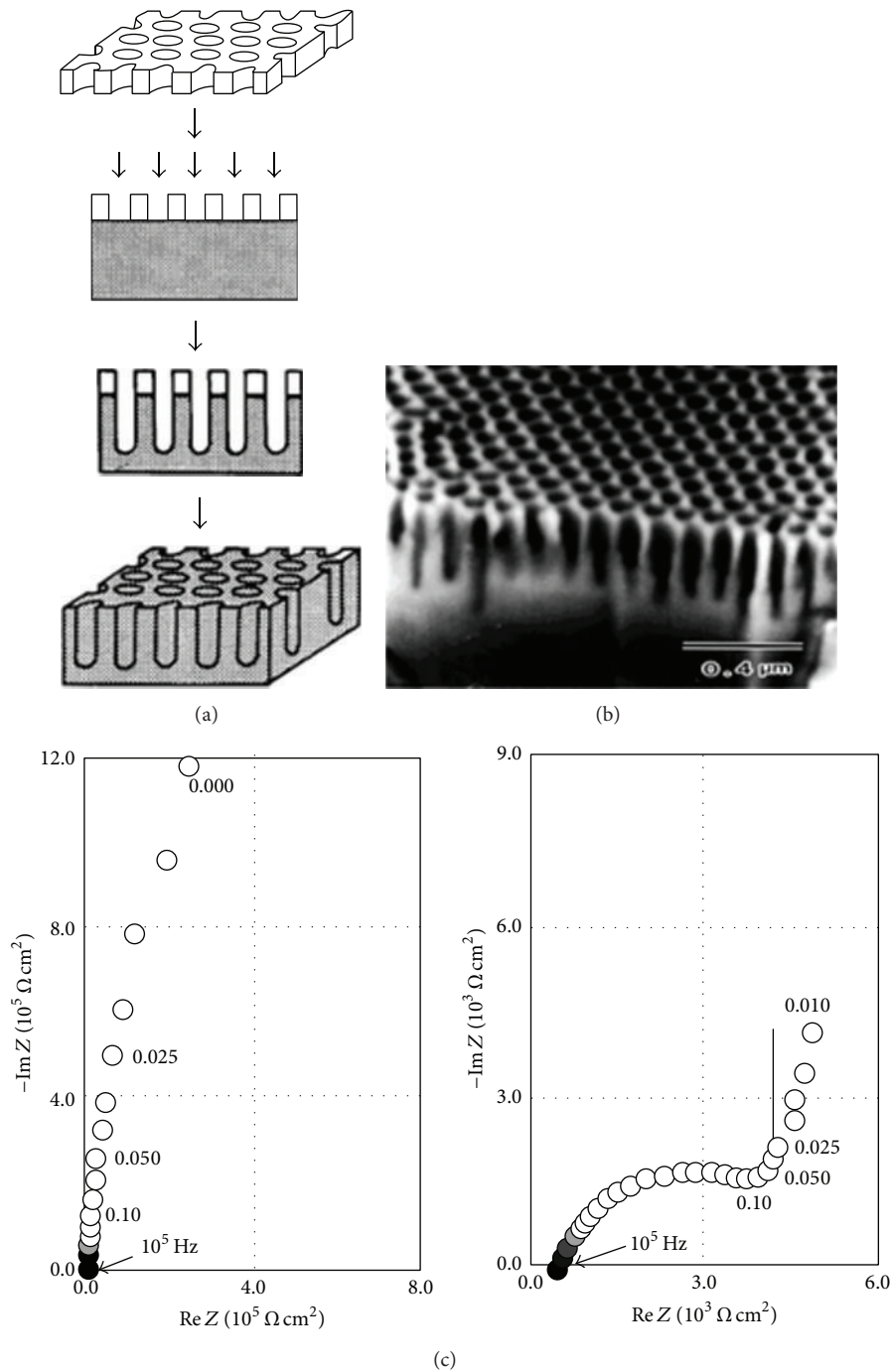


FIGURE 7: (a) Schematic diagram of the fabrication procedure for the diamond nanohoneycomb. (b) Cross-sectional view of the diamond nanohoneycomb. (c) Complex-plane plots of the impedance for electrodes of as-deposited diamond (left) and pore types 400 nm \times 3 μ m (right), at 10.4 V versus Ag/AgCl [9, 25].

and selective chemical etching of sp^2 carbons by reactive hydrogen atoms and ions. The density and geometry of these nanopillars were determined by the initial structure of diamond films and reactive ion etching conditions. These nanopillars have potential applications in high performance diamond-based biomedical and chemical sensors and in mechanical and thermal management.

Using the similar nanoassembled Au nanoparticles (NPs) as the mask, another type of hybrid structure of Au-NP/diamond-nanopit has been fabricated on single-crystal diamond by oxygen plasma etching (Figure 9(a)) [27–29], where the diamond-nanopits are different to diamond nanopillars and/or nanowires arrays generated from polycrystalline diamond films having abundant grain boundaries

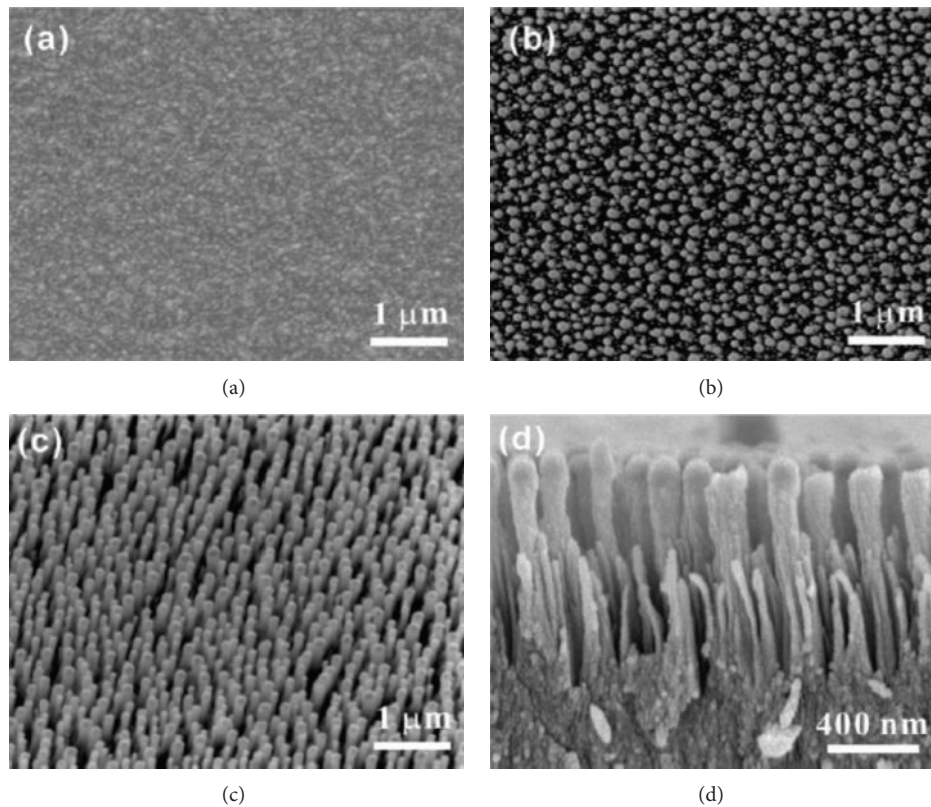


FIGURE 8: SEM morphologies showing (a) the nanocrystalline diamond film with a flat surface, (b) the gold nanodots formed on the nanocrystalline diamond surface, and (c) nanocrystalline diamond film with nanopillar array collected by sample tilting and (d) from the cross section [26].

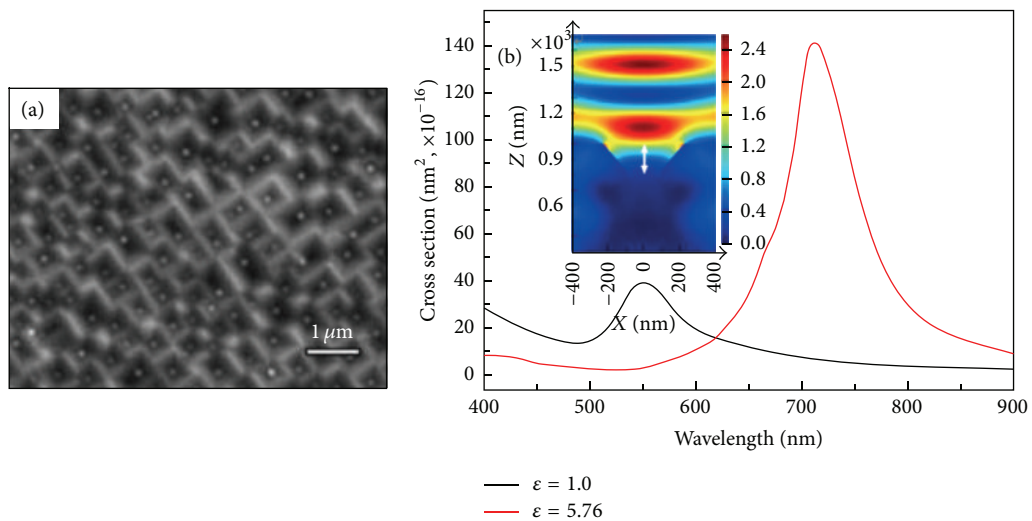


FIGURE 9: (a) The planar SEM image of the surface of single crystal diamond after oxygen plasma etching for 60 s having nanopits infilled with Au nanoparticles. (b) Calculated LSPR scattering cross section spectra of a semiellipsoidal Au NP placed in air (dark) and on diamond (red), showing the resonance peaks at 550 nm (in air) and 718 nm (on diamond). The inset of (b) reveals the cross-sectional electric field intensity ($|E|^2$) distribution in a diamond-nanopit [27, 28].

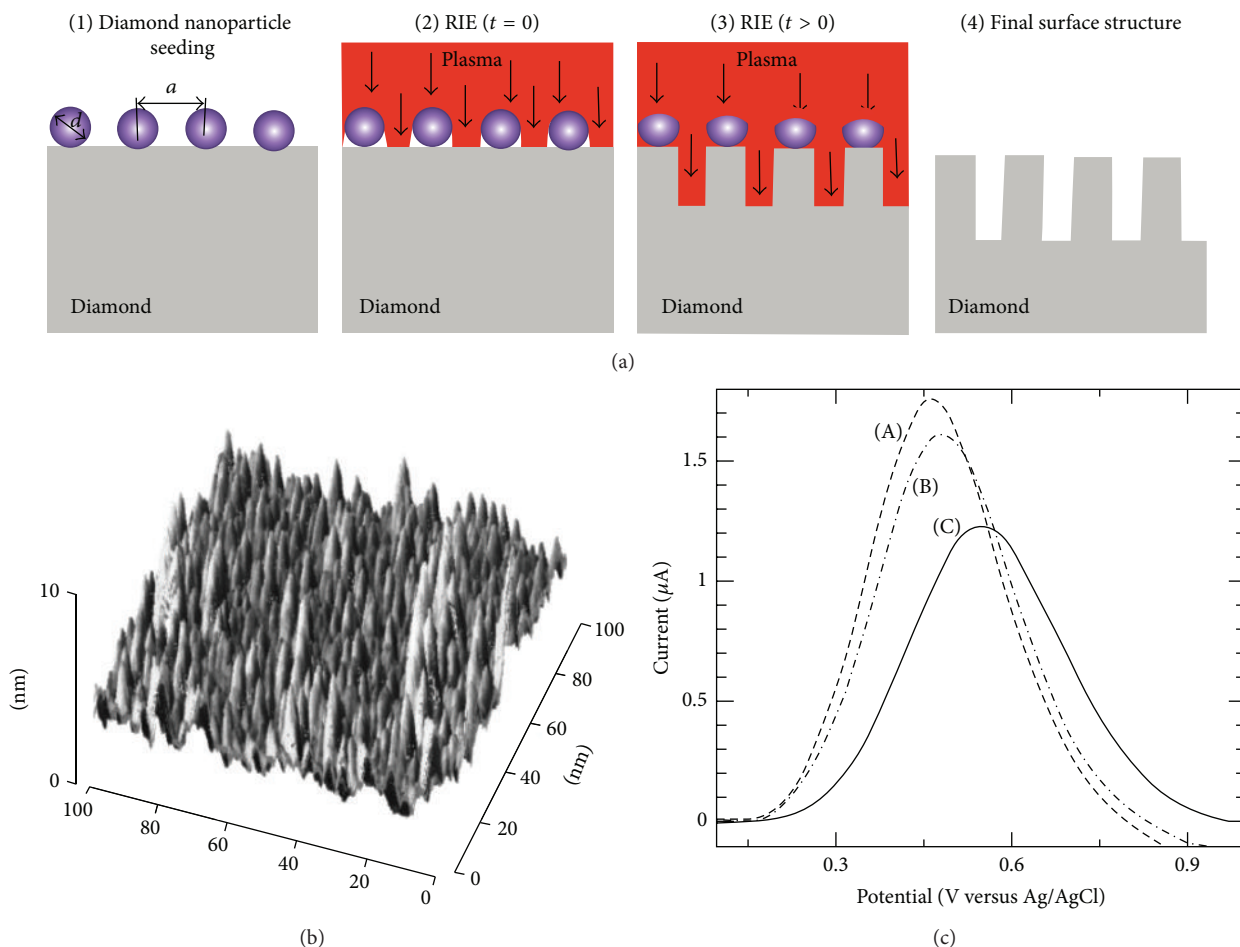


FIGURE 10: (a) Schematic plots of fabrication of diamond nanowires by a reactive ion etching (RIE). (b) Typical AFM image of the fabricated diamond nanowires. (c) Differential pulse voltammograms of 1.0 mM $\text{Fe}(\text{CN})_6^{3-/4-}$ in pH 7.4 phosphate buffer as detected on diamond nanowires after marker ss-DNA immobilization (curve (A)), after exposure to single-based mismatched DNA (10 nM; curve (B)), and after exposure to complementary target DNA (10 nM; curve (C)) [30, 31].

[26]. The three-dimensional finite-difference time-domain (FDTD) simulations revealed strong localized surface plasmon resonance (LSPR) scattering and enhanced electric field exhibited by this hybrid nanoassembled-metal/diamond-nanopit (Figure 9(b)). Experimentally, with excitations at 633 and 830 nm close to the calculated LSPR wavelength, the photoluminescence (PL) intensities of the peak at 738 nm originating from the single-photon source of silicon vacancy (SiV) centers in diamond were significantly enhanced by factors of ~ 100 and ~ 50 , respectively, with respect to that from normal Si-doped diamond without the hybrid structure [27]. This structure could also realize a larger surface enhanced Raman scattering (SERS) enhancement factor [28]. Because of the unique advantages of diamond, the diamond-nanopit structure can serve as a robust structural template for fabricating various membranes with pyramid-structured surface [29].

The other strategy of mask is using diamond nanoparticles [30–32]. By depositing diamond nanoparticles and following a RIE in an O_2/CF_4 gas mixture, Yang et al. [30] realized diamond nanowires on boron-doped single-crystalline

CVD diamond films after a top-down procedure (Figure 10). As an electrode, the active area of diamond nanowires has been significantly enhanced. Furthermore, the tip-modified diamond nanowires are promising with respect to biosensor applications. When used as DNA sensor, the sensitivity is about 100 to 1000 times better, compared to published data available in the literature, where comparable DNA strands have been used with comparable redox mediator molecules on planar gold electrodes, gold nanowires, and diamond [31]. Based on the similar method, Lu et al. fabricated vertically aligned diamond nanoneedles on polycrystalline diamond nanofilms [32]. Gas sensing measurements with the diamond nanoneedles were performed at room temperature for both reducing (NH_3) and oxidizing (NO_2) gases. Due to the increased surface area-to-volume ratio and nanotip effect of the diamond nanoneedles, great enhancements of chemical sensing ability and sensitivity were presented compared with the unmodified nanodiamond films.

The development of a robust light source that emits one photon at a time will allow new technologies such as secure communication through quantum cryptography.

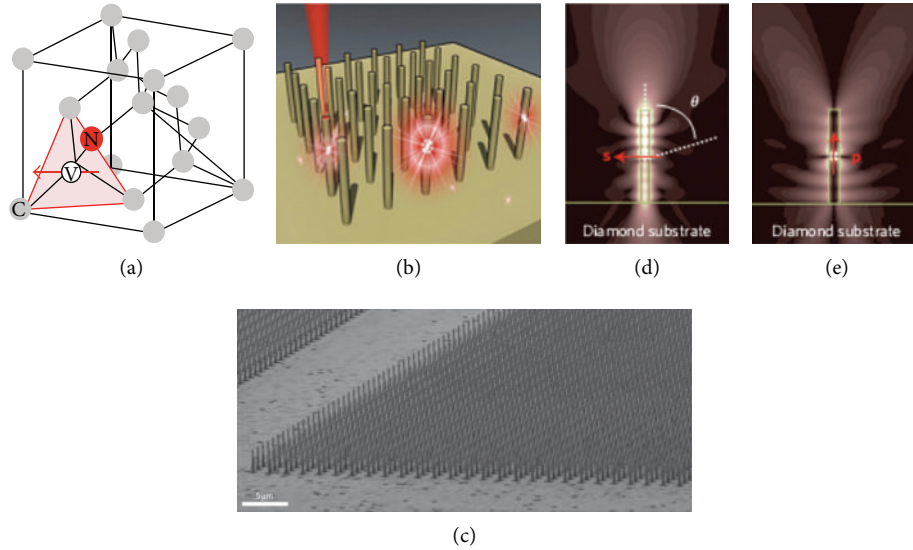


FIGURE 11: Single-photon source based on an NV centre in a diamond nanowire. For details see [34].

Luminescent centers in diamond (e.g., nitrogen vacancy (NV) centers) have recently emerged as a stable source offering spin quantum bits with optical readout. Hausmann et al. [33] and Babinec et al. [34] demonstrated a single-photon source composed of a NV center in a diamond nanowire on the (100) crystal plane (Figure 11), which produces ten times greater flux than bulk diamond devices, while using ten times less power. The diamond nanowires were fabricated from a mask patterned diamond crystal by RIE with oxygen plasma. This result, as well as that for SiV enhancement [27], enables a new class of devices for photonic and quantum information processing based on nanostructured diamond and could have a broader impact in nanoelectromechanical systems (NEMS), sensing, and scanning probe microscopy.

For further investigating the advanced single-photon properties of NV center, Jiang et al. [35] developed an overlay patterning method for fast, designable, and controllable fabrication of various three-dimensional (3D) diamond micro/nanostructures on (100) plane with focused-ion-beam (FIB) milling. Diamond solid immersion lens and nanopillar with NV center placed at the designed location could enable efficient single-photon collection by overcoming the total internal reflection at the diamond/air interface. The enhancements of about tenfold of the single photons collection rate, well-reserved long electron spin dephasing time, and single-photon emission properties have been obtained. In 2014, Neu et al. [36] fabricated nanophotonic structures of diamond nanopillars on (111)-oriented single-crystalline CVD diamond. The authors demonstrated that this crystal orientation offers optimal coupling of NV center emission to the nanopillar mode and might thus be advantageous over previous approaches with (100) crystal orientation. High saturated fluorescence count rates around 10^6 counts per second were realized based on these nanopillars.

Combining procedures of carbon ion implantation, photolithography, and electron beam lithography and RIE, Liao et al. [37] designed and fabricated the suspended single-crystal

diamond nanowires with well-controlled dimensions in batches for NEMS (Figure 12). All-single-crystal diamond NEM switches were demonstrated using these nanowires with high reproducibility, high controllability, repeated switching, and no stiction. Diamond switches not only overcome the stiction and abrasion problems in existing electromechanical switches, but also circumvent the shallow doping problem. The concept and technology in this work would be helpful for promoting the rapid developments of the next generation of high performance NEMS.

4. Diamond-Related Nanoheterojunction

Combining oxide or nitride semiconductors with diamond substrates attracts great attention mainly motivated by the lack of efficient p-type doping in the oxides (nitrides) and n-type doping in diamond, respectively. The complementary configuration of these wide band gap materials with p-type boron-doped diamond and n-type oxides (ZnO , TiO_2) and n-type nitrides (GaN , AlN) has been most widely studied recently [10–13, 38–53]. Generally, growth of oxides and nitrides films on diamond remains challenging due to the high difference in the thermal expansion coefficients and large lattice mismatch (leading to structural imperfections) and relatively less efficient performance of devices. Compared with continuous bulk films, the low-dimensional structures (e.g., nanorods, nanowires, and nanotubes) with a high ratio of surface to volume, defect-free, and enhanced quantum effect are expected to yield much better structural quality and do not suffer from thermal mismatch on diamond, consequently improving the performances of the hybridized structural devices. In this part, we focus on three structures of $\text{ZnO}/\text{diamond}$, $\text{TiO}_2/\text{diamond}$, and $\text{GaN}/\text{diamond}$, where the oxides and nitrides are of nanosized feature.

ZnO is an important semiconductor having unique properties of wide direct wide band gap (3.37 eV) and large

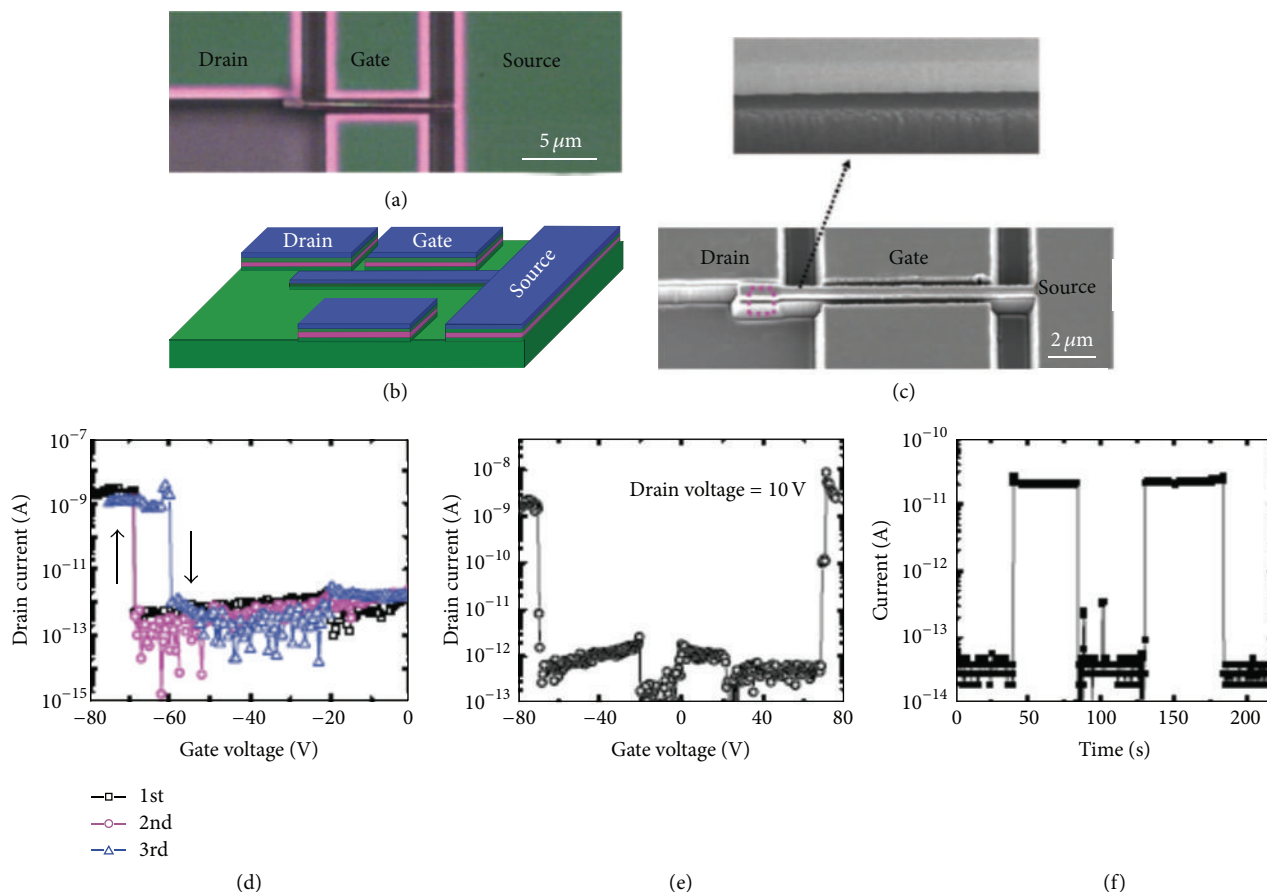


FIGURE 12: (a) Optical image of all-single-crystal diamond 3T-NEM switch in ON state. The dimensions of the cantilever are $14 \mu\text{m}$ in length and 400 nm in width. The gate-source gap is 400 nm . (b) Schematic diagram of the switch. (c) SEM image of the switch viewed at a titled angle of 20° . (d) Repeated and hysteresis switching behavior of the device controlled by the gate voltage. (e) Gate voltage-drain current dependence of a similar switch. (f) Time dependence of the switch at a gate voltage of 75 V and a drain voltage of 5 V [37].

exciton binding energy (60 meV) at room temperature. The combined structures of diamond and ZnO have been paid more attention to fabricate semiconductor heterojunctions [52]. Previously, the existing form of ZnO was generally performed as film deposited on diamond wafer [53]. In recent decade, ZnO-related nanostructures and the corresponding nanooptoelectronic devices have been extensively studied [54]. The heterojunctions based on ZnO nanostructures were generally grown on silicon [55], GaN [56], sapphire [57], and diamond [11, 39, 41]. Experimentally, the performances of the diamond-related biosensor electrodes have been significantly improved by modifying ZnO nanorods (NRs) (Figure 13) synthesized using the sol-gel method [10]. Li's group reported the growth of ZnO NRs on CVD diamond by thermal vapor transport [11, 38–40] and hydrothermal methods [41]. Using the former method, in the initial growth status, the semispherical ZnO nuclei were preferably deposited near the growth steps on the terraces and the boundaries of diamond grains. With increasing the growth time, the [0001] orientated ZnO nanorods with large aspect ratio appeared and further covered the whole diamond film, as shown in Figure 14. Furthermore, the epitaxial relation between the (0001) ZnO and (111) diamond is proposed following

$(0001)[11\bar{2}0] \text{ ZnO} // (111)[\bar{1}\bar{1}0] \text{ diamond}$ or $(0001)[10\bar{1}0] \text{ ZnO} // (111)[1\bar{1}0] \text{ diamond}$ [39, 42], while the relation between the (0001) ZnO and (100) diamond is mainly of $(0001)[0001] \text{ ZnO} // (101)[101] \text{ diamond}$ [39].

As doped and/or unintentionally doped ZnO is generally n-type semiconductor and p-type diamond is easy to be realized by boron doping, the hybrid n-ZnO NRs/p-diamond heterojunctions have been constructed [11, 39]. For a n-ZnO NRs/p-diamond heterojunction with degenerated p-type diamond (heavily B-doped diamond having a higher carrier concentration at $10^{20}/\text{cm}^3$ order of magnitude) especially, a negative differential resistance (NDR) phenomenon was evidently presented in the corresponding I - V plot (Figure 15), which can be attributed to the tunneling current in the structure [39]. Since both diamond and ZnO are important high-temperature semiconductor materials, the temperature-dependent electrical properties of the n-ZnO NRs/p-diamond heterojunctions were studied and the corresponding parameters varied at different temperatures [11]. At relatively high temperature, the ohmic behavior and the carrier injection has been improved. And at higher voltages, the injected current of the heterojunction follows the trap-free space-charge-limited current (SCLC) law with

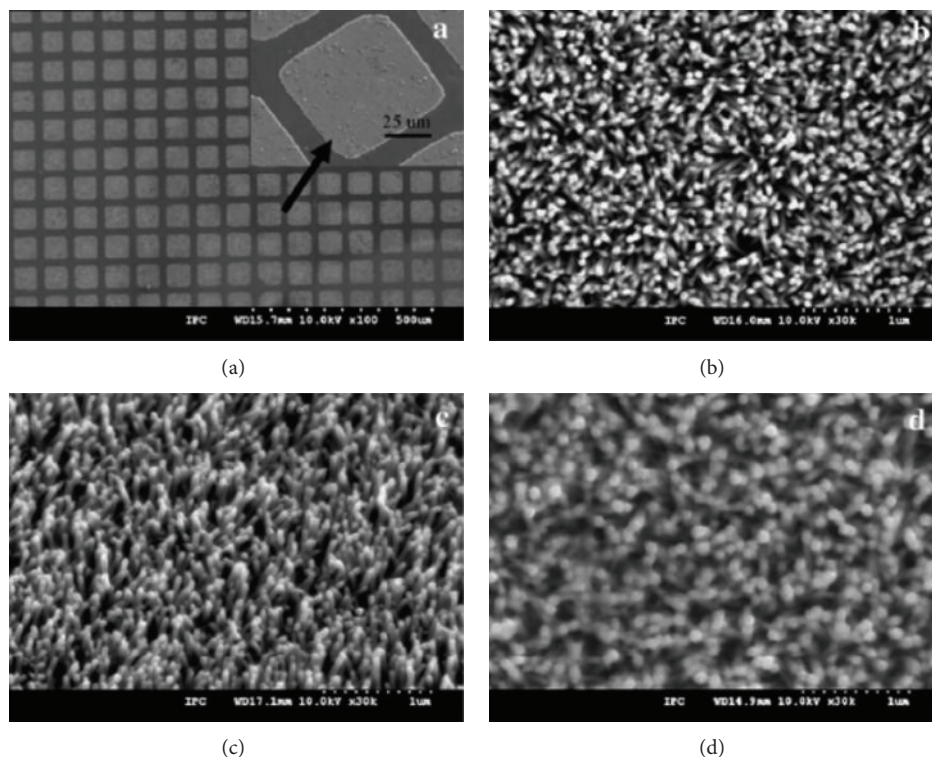


FIGURE 13: SEM images of (a) the ZnO nanorod microarrays on boron-doped nanodiamond thin film surfaces (the inset shows the enlarged image of a square-shaped ZnO nanorod array), (b) top view of ZnO nanorod arrays, and (c) tilt view of ZnO nanorod arrays and (d) functional ZnO nanorod arrays [10].

the exponent close to 2 because the traps states will be filled by larger thermally activated carriers. These results emphasize the suitability for fabricating n-ZnO/p-diamond-based high frequency, high power, and high temperature optoelectronic nanodevices.

Another important metal oxide of TiO_2 has attracted considerable attention because it is especially suitable for applications in the fields of photocatalytic degradation of pollutants, hydrogen generation from photoelectrocatalytic water splitting, dye-sensitized solar cells, and so forth [58]. The applications of TiO_2 as photocatalysts are encumbered to a certain extent by the relatively low quantum yield that is normally caused due to rapid recombination of photogenerated electrons and holes. In order to enhance the quantum yield, a heterojunction structure has been further introduced because the heterojunction could provide a potential driving force (the internal electrostatic potential in the space charge region) to reduce the recombination of photogenerated charge carriers. Highly efficient photocatalysts have been realized by n-type anatase TiO_2 film joined to CVD p-type boron-doped diamond (BDD) [43, 44], which has unique properties of wide electrochemical potential window, long-term response stability, high level of mechanical strength, and chemical corrosion resistance. Compared with continuous TiO_2 films, low-dimensional TiO_2 structures (e.g., nanotubes, nanorods), which possess a high ratio of surface to volume and provide a convenient way for photogenerated carriers to transfer to the reaction surfaces, lead to improved photocatalytic efficiency [45,

46]. In [47, 48], TiO_2 nanoparticles (nanotubes) have been deposited on BDD film by a spin coating method for applications in electrochemical reactivity (electro- and bioelectrocatalysis). By a liquid phase deposition (LPD) method using a ZnO nanorod template, the vertical anatase TiO_2 nanotube (TiNT) arrays were directly grown on a CVD BDD film, and the fabricated n-type TiNT/p-type BDD (n-TiNT/p-BDD) heterojunctions showed highly efficient photocatalytic activities for the decomposition of azo dye C.I. reactive yellow 15 (RY15) [12]. The increased ability to separate photogenerated charge carriers by the pn junction (n-TiNT/p-BDD) would enhance the photocatalytic activity. Additionally, the TiNT array structure provides more active positions for the photocatalytic processes exposed to UV light, and the loose TiNTs are favorable for permitting more UV light to reach the BDD side through TiNTs with respect to the case of TiO_2 film on BDD.

In 2015, different to depositing TiO_2 on diamond, Siuzdak et al. [49] reported on novel composite nanostructure of thin BDD films (thickness of $\sim 200\text{--}500$ nm) grown on top of as-fabricated TiO_2 nanotubes (Figure 16). The nanostructures made of BDD-modified TiO_2 nanotubes showed an increase in activity and performance when used as electrodes in electrochemical environments. The substantial improvement of electrochemical performance and the excellent rate capability could be attributed to the synergistic effect of TiO_2 treatment in CH_4/H_2 plasma and the high electrical conductivity of BDD layers.

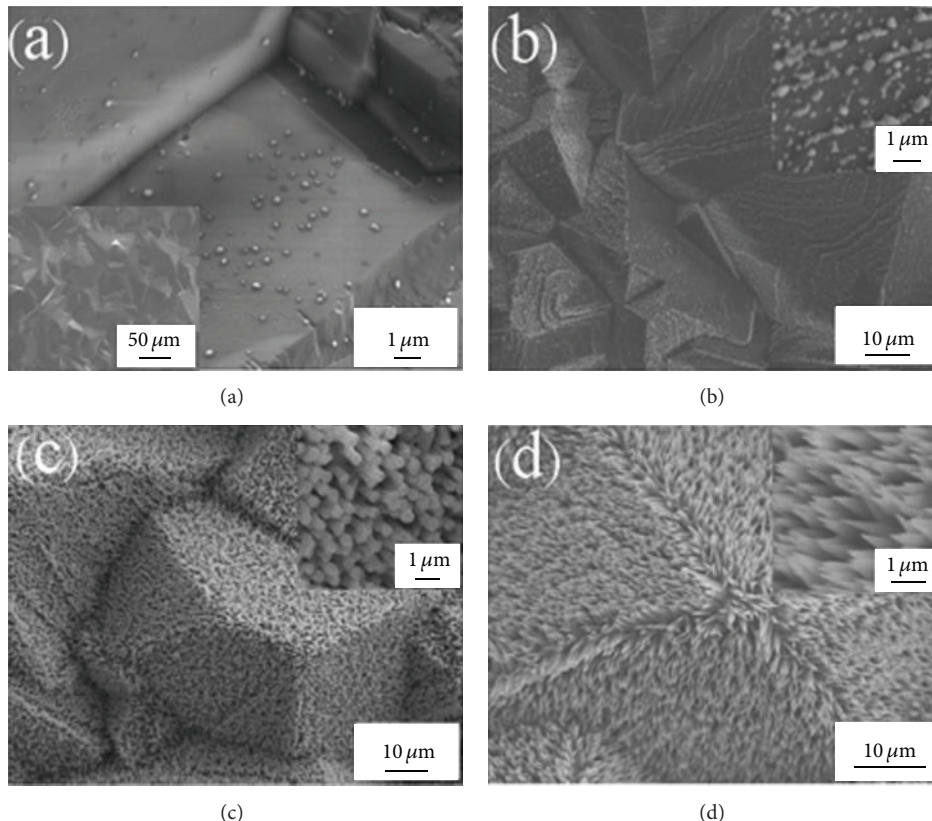


FIGURE 14: SEM images of ZnO nanostructures synthesized on microcrystalline diamond films for 0.5 min (a), 2 min (b), and 5 min ((c) and (d)). The inset of (a) is the image of bird's-eye view. The insets of (b)–(d) are the high-magnitude images of ZnO NRs [40].

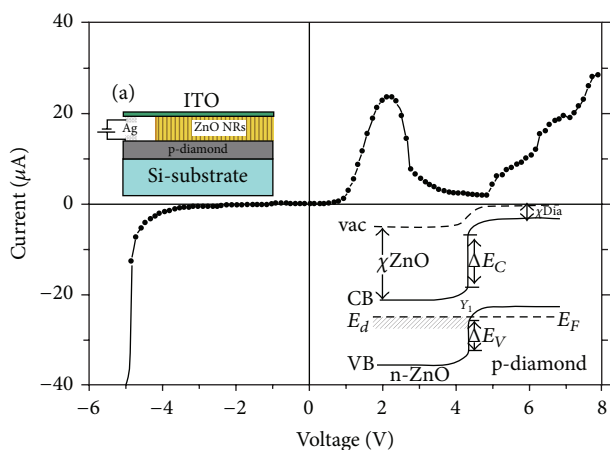


FIGURE 15: I - V characteristic of the n-ZnO NR/p-diamond heterojunction constructed with degenerated p-diamond, showing a negative differential resistance phenomenon. The insets are the schematic diagram of the pn heterojunction (upper left) and the energy band diagram of the heterojunction at thermal equilibrium (lower right) [39].

In recent years, the field of GaN-based nanowires (NWs) has made substantial progress as a possible alternative to planar structures for light-emitting diodes, laser diodes,

sensing applications, photovoltaics, and catalysis. Schuster et al. [13, 50, 51] reported on the fabrication, characterization, and properties of the low-dimensional GaN structures on diamond, which provide important information for realizing high performance optoelectronic nanodevices in the UV-spectral range and the electrical control of NV centers in diamond. By plasma-assisted molecular beam epitaxy, the self-assembled epitaxial GaN NWs with an excellent crystalline quality were vertically grown catalyst-free on (111) single crystal diamond (Figure 17). A strong and sharp excitonic emission in the PL spectrum reveals excellent optical properties superior to state-of-the-art GaN NWs on silicon substrates [13]. The position-controlled growth of GaN NWs on diamond substrates with the help of structured titanium masks was demonstrated, and a transition from a nanowire toward a nanotube growth mode was observed [50]. The controlled fabrication of GaN nanotube arrays will be of interest for applications benefiting from a high surface-to-volume ratio. Furthermore, the authors addressed the different aspects of GaN nanowire doping (Si and Mg) [51]. The GaN NWs density and strains state, distributions of dopant concentration and charge carriers, and optical properties related to the doping in NWs have been investigated. The results help to understand and control the mechanisms of doping in GaN nanostructures on diamond to intentionally tailor their electric and optical properties for device fabrication.

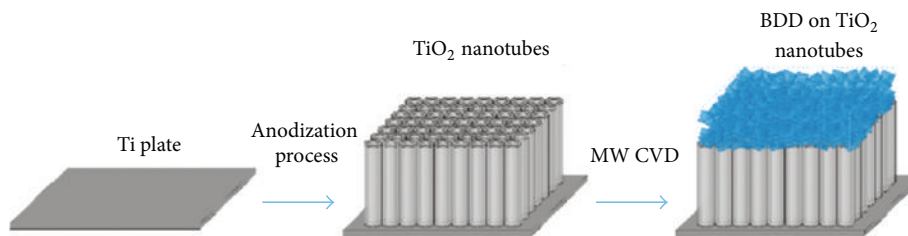


FIGURE 16: Formation scheme of composite TiO₂ nanotube/boron-doped diamond (BDD) electrodes [49].

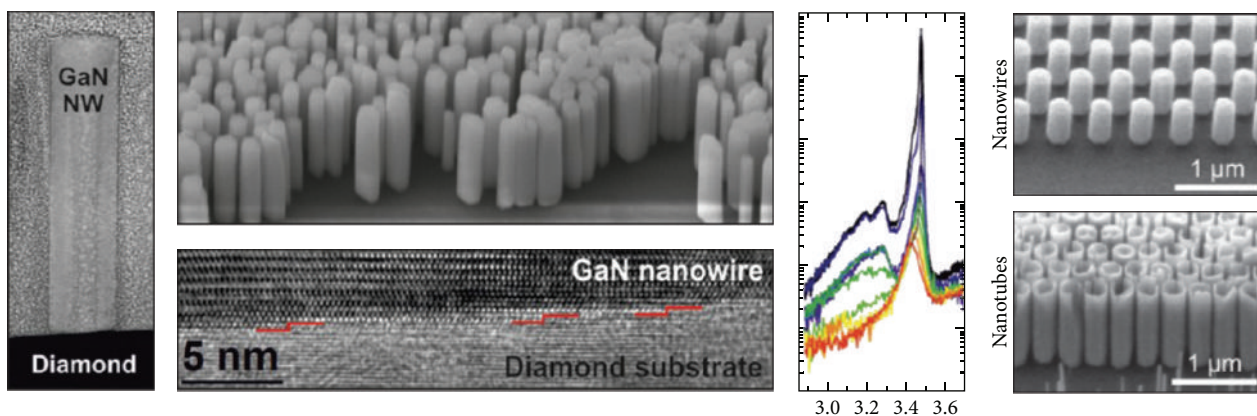


FIGURE 17: From left to right: cross-section high-angle annular dark-field STEM of an exemplary GaN NW on diamond substrate; tilted-view SEM images of as-grown GaN NWs on diamond (top), HRTEM image of the interface region (bottom); temperature-dependent PL spectra of GaN NWs on diamond with typical NBE shift due to band gap shrinkage [13]; selective area grown GaN NW arrays without (top) and with a hole (bottom) [50].

5. Conclusion and Outlook

In this review, we gave a very recent overview of diamond-related nanostructures, especially including the three types developed in the current decade. The atomically thick 2D few-layer diamond nanofilms with and without varying surface functionalization have been theoretically predicted, and the corresponding optimized structures and the electronic and magnetic properties are calculated showing differences from that of bulk diamond. The challenge of those 2D nanofilms is to find a feasible route to experimentally realize in large sizes (e.g., more than tens and hundreds of micrometers) for practical application. Some possible approaches have been mentioned in the text. As for the nanostructural surface of diamond films, which are generally obtained by top-down approach following various etching processes (with designed mask patterns), great achievements have been made in plasmonic enhancement, single-photon source, electron field emission, and biologic sensing for the potential applications. The technologies of feasibility, low cost, large scale, high accurate controllability, and novel structures are quite desirable to be developed to meet the growing demand. The heterostructures combined of nanosized n-type oxides (nitrides) and bulk p-type diamond have been experimentally fabricated to overcome the lattice mismatch, lack of efficient p-type doping in the oxides and nitrides and n-type doping in diamond, and structural imperfections in the interface region. However, depositing high

quality and highly orientated nanosized oxides (nitrides) on (100)-oriented diamond, which is of high quality grown by CVD process, is difficult to be realized due to the large lattice mismatch between the hexagonal/tetragonal oxides (nitrides) and the cubic (100) diamond facet. Suitable buffer layer and/or optimized growth conditions (e.g., temperature, bias enhanced nucleation, and/or pretreated substrate) should be provided to achieve the goal. In short, this review reveals the current key issues, opportunities, and challenges facing present and future researches on diamond material with various nanostructures for advancing in commercial applications.

Conflict of Interests

The authors declare that there is no conflict of interests regarding the publication of this paper.

Acknowledgment

This work was supported by the National Natural Science Foundation of China (NSFC) (Grant no. 51472105).

References

- [1] D. M. Gruen, O. A. Shenderova, and A. Y. Vul, *Synthesis, Properties and Applications of Ultrananocrystalline Diamond*, vol. 192 of *NATO Science Series*, Springer Netherlands, 2005.

- [2] K. S. Novoselov, A. K. Geim, S. V. Morozov et al., "Electric field effect in atomically thin carbon films," *Science*, vol. 306, no. 5696, pp. 666–669, 2004.
- [3] L. Y. Zhu, H. Hu, Q. Chen, S. D. Wang, J. L. Wang, and F. Ding, "Formation and electronic properties of hydrogenated few layer graphene," *Nanotechnology*, vol. 22, no. 18, Article ID 185202, 2011.
- [4] H. D. Li, J. Li, Z. G. Wang, and G. T. Zou, "Layer number-dependent structural evolution of two-dimensional diamond films," *Chemical Physics Letters*, vol. 550, pp. 130–133, 2012.
- [5] J. O. Sofo, A. S. Chaudhari, and G. D. Barber, "Graphane: a two-dimensional hydrocarbon," *Physical Review B—Condensed Matter and Materials Physics*, vol. 75, no. 15, Article ID 153401, 2007.
- [6] L. A. Chernozatonskii, P. B. Sorokin, A. G. Kvashnin, and D. G. Kvashnin, "Diamond-like C_2H nanolayer, diamane: simulation of the structure and properties," *JETP Letters*, vol. 90, no. 2, pp. 134–138, 2009.
- [7] L. S. Li and X. Zhao, "Transformation between different hybridized bonding structures in two-dimensional diamond-based materials," *The Journal of Physical Chemistry C*, vol. 115, no. 45, pp. 22168–22179, 2011.
- [8] H. Shiomi, "Reactive ion etching of diamond in O_2 and CF_4 plasma, and fabrication of porous diamond for field emitter cathodes," *Japanese Journal of Applied Physics*, vol. 36, no. 12, pp. 7745–7748, 1997.
- [9] H. Masuda, M. Watanabe, K. Yasni, D. Tryk, T. Rao, and A. Fujishima, "Fabrication of a nanostructured diamond honeycomb film," *Advanced Materials*, vol. 12, no. 6, pp. 444–447, 2000.
- [10] J. W. Zhao, D. H. Wu, and J. F. Zhi, "A novel tyrosinase biosensor based on bifunctional ZnO nanorod microarrays on the nanocrystalline diamond electrode for detection of phenolic compounds," *Bioelectrochemistry*, vol. 75, no. 1, pp. 44–49, 2009.
- [11] D. D. Sang, H. D. Li, S. H. Cheng, Q. L. Wang, Q. Yu, and Y. Z. Yang, "Electrical transport behavior of n-ZnO nanorods/p-diamond heterojunction device at higher temperatures," *Journal of Applied Physics*, vol. 112, no. 3, Article ID 036101, 2012.
- [12] J. J. Yuan, H. D. Li, S. Y. Gao, Y. H. Lin, and H. Y. Li, "A facile route to n-type TiO_2 -nanotube/p-type boron-doped-diamond heterojunction for highly efficient photocatalysts," *Chemical Communications*, vol. 46, no. 18, pp. 3119–3121, 2010.
- [13] F. Schuster, F. Furtmayr, R. Zamani et al., "Self-assembled GaN nanowires on diamond," *Nano Letters*, vol. 12, no. 5, pp. 2199–2204, 2012.
- [14] H. W. Kroto, J. R. Heath, S. C. O'Brien, R. F. Curl, and R. E. Smalley, " C_{60} : buckminsterfullerene," *Nature*, vol. 318, no. 6042, pp. 162–163, 1985.
- [15] S. Iijima, "Helical microtubules of graphitic carbon," *Nature*, vol. 354, no. 6348, pp. 56–58, 1991.
- [16] T. M. Willey, C. Bostedt, T. van Buuren et al., "Molecular limits to the quantum confinement model in diamond clusters," *Physical Review Letters*, vol. 95, no. 11, Article ID 113401, 2005.
- [17] D. C. Elias, R. R. Nair, T. M. G. Mohiuddin et al., "Control of graphene's properties by reversible hydrogenation: evidence for graphane," *Science*, vol. 323, no. 5914, pp. 610–613, 2009.
- [18] J. Zhou, Q. Wang, Q. Sun, X. S. Chen, Y. Kawazoe, and P. Jena, "Ferromagnetism in semihydrogenated graphene sheet," *Nano Letters*, vol. 9, no. 11, pp. 3867–3870, 2009.
- [19] L. A. Chernozatonskii, P. B. Sorokin, A. A. Kuzubov et al., "Influence of size effect on the electronic and elastic properties of diamond films with nanometer thickness," *Journal of Physical Chemistry C*, vol. 115, no. 1, pp. 132–136, 2011.
- [20] J. Li, H. D. Li, Z. G. Wang, and G. T. Zou, "Structure, magnetic, and electronic properties of hydrogenated two-dimensional diamond films," *Applied Physics Letters*, vol. 102, no. 7, Article ID 073114, 2013.
- [21] M. Fyta, "Nitrogen-vacancy centers and dopants in ultrathin diamond films: electronic structure," *Journal of Physical Chemistry C*, vol. 117, no. 41, pp. 21376–21381, 2013.
- [22] D. Odkhuu, D. Shin, R. S. Ruoff, and N. Park, "Conversion of multilayer graphene into continuous ultrathin sp^3 -bonded carbon films on metal surfaces," *Scientific Reports*, vol. 3, article 3276, 2013.
- [23] A. G. Kvashnin, L. A. Chernozatonskii, B. I. Yakobson, and P. B. Sorokin, "Phase diagram of quasi-two-dimensional carbon, from graphene to diamond," *Nano Letters*, vol. 14, no. 2, pp. 676–681, 2014.
- [24] L. Y. Antipina and P. B. Sorokin, "Converting chemically functionalized few-layer graphene to diamond films: a computational study," *The Journal of Physical Chemistry C*, vol. 119, no. 5, pp. 2828–2836, 2015.
- [25] K. Honda, T. N. Rao, D. A. Tryk et al., "Impedance characteristics of the nanoporous honeycomb diamond electrodes for electrical double-layer capacitor applications," *Journal of the Electrochemical Society*, vol. 148, no. 7, pp. A668–A679, 2001.
- [26] Y. S. Zou, Y. Yang, W. J. Zhang et al., "Fabrication of diamond nanopillars and their arrays," *Applied Physics Letters*, vol. 92, no. 5, Article ID 053105, 2008.
- [27] J. Song, H. D. Li, F. Lin, L. Y. Wang, H. L. Wu, and Y. Q. Yang, "Plasmon-enhanced photoluminescence of Si-V centers in diamond from a nanoassembled metal-diamond hybrid structure," *CrystEngComm*, vol. 16, no. 36, pp. 8356–8362, 2014.
- [28] J. Song, S. H. Cheng, H. D. Li, H. Y. Guo, S. P. Xu, and W. Q. Xu, "A novel surface-enhanced Raman scattering substrate: diamond nanopit infilled with gold nanoparticle," *Materials Letters*, vol. 135, pp. 214–217, 2014.
- [29] J. Song, H. D. Li, S. H. Cheng, and Q. L. Wang, "Fabrication of a hybrid structure of diamond nanopits infilled with a gold nanoparticle," *RSC Advances*, vol. 4, no. 60, pp. 32000–32003, 2014.
- [30] N. J. Yang, H. Uetsuka, E. Osawa, and C. E. Nebel, "Vertically aligned nanowires from boron-doped diamond," *Nano Letters*, vol. 8, no. 11, pp. 3573–3576, 2008.
- [31] N. J. Yang, H. Uetsuka, and C. E. Nebel, "Biofunctionalization of vertically aligned diamond nanowires," *Advanced Functional Materials*, vol. 19, no. 6, pp. 887–893, 2009.
- [32] C. Lu, Y. L. Li, S. B. Tian, W. X. Li, J. J. Li, and C. Z. Gu, "Enhanced gas-sensing by diamond nanoneedle arrays formed by reactive ion etching," *Microelectronic Engineering*, vol. 88, no. 8, pp. 2319–2321, 2011.
- [33] B. J. M. Hausmann, M. Khan, Y. Zhang et al., "Fabrication of diamond nanowires for quantum information processing applications," *Diamond & Related Materials*, vol. 19, no. 5–6, pp. 621–629, 2010.
- [34] T. M. Babinec, B. J. M. Hausmann, M. Khan et al., "A diamond nanowire single-photon source," *Nature Nanotechnology*, vol. 5, no. 3, pp. 195–199, 2010.
- [35] Q. Q. Jiang, D. Q. Liu, G. Q. Liu et al., "Focused-ion-beam overlay-patterning of three-dimensional diamond structures for advanced single-photon properties," *Journal of Applied Physics*, vol. 116, no. 4, Article ID 044308, 2014.

- [36] E. Neu, P. Appel, M. Ganzhorn et al., "Photonic nano-structures on (111)-oriented diamond," *Applied Physics Letters*, vol. 104, no. 15, Article ID 153108, 2014.
- [37] M. Y. Liao, S. Hishita, E. Watanabe, S. Koizumi, and Y. Koide, "Suspended single-crystal diamond nanowires for high-performance nanoelectromechanical switches," *Advanced Materials*, vol. 22, no. 47, pp. 5393–5397, 2010.
- [38] H. D. Li, H. Lü, D. D. Sang et al., "Synthesizing of ZnO micro/nanostructures at low temperature with new reducing agents," *Chinese Physics Letters*, vol. 25, no. 10, pp. 3794–3797, 2008.
- [39] H. D. Li, D. D. Sang, S. H. Cheng et al., "Epitaxial growth of ZnO nanorods on diamond and negative differential resistance of n-ZnO nanorod/p-diamond heterojunction," *Applied Surface Science*, vol. 280, pp. 201–206, 2013.
- [40] D. D. Sang, H. D. Li, and S. H. Cheng, "Growth and electron field emission of ZnO nanorods on diamond films," *Applied Surface Science*, vol. 258, no. 1, pp. 333–336, 2011.
- [41] Q. Yu, J. Li, H. D. Li, Q. L. Wang, S. H. Cheng, and L. L. Li, "Fabrication, structure, and photocatalytic activities of boron-doped ZnO nanorods hydrothermally grown on CVD diamond film," *Chemical Physics Letters*, vol. 539–540, pp. 74–78, 2012.
- [42] A. Hachigo, H. Nakahata, K. Higaki, S. Fujii, and S.-I. Shikata, "Heteroepitaxial growth of ZnO films on diamond (111) plane by magnetron sputtering," *Applied Physics Letters*, vol. 65, no. 20, pp. 2556–2558, 1994.
- [43] H. B. Yu, S. Chen, X. Quan, H. M. Zhao, and Y. B. Zhang, "Fabrication of a TiO₂-BDD heterojunction and its application as a photocatalyst for the simultaneous oxidation of an azo dye and reduction of Cr(VI)," *Environmental Science and Technology*, vol. 42, no. 10, pp. 3791–3796, 2008.
- [44] J. H. Qu and X. Zhao, "Design of BDD-TiO₂ hybrid electrode with P-N function for photoelectroalytic degradation of organic contaminants," *Environmental Science and Technology*, vol. 42, no. 13, pp. 4934–4939, 2008.
- [45] Y. S. Chen, J. C. Crittenden, S. Hackney, L. Sutter, and D. W. Hand, "Preparation of a novel TiO₂-based p-n junction nanotube photocatalyst," *Environmental Science & Technology*, vol. 39, no. 5, pp. 1201–1208, 2005.
- [46] H. G. Kim, P. H. Borse, W. Choi, and J. S. Lee, "Photocatalytic nanodiodes for visible-light photocatalysis," *Angewandte Chemie—International Edition*, vol. 44, no. 29, pp. 4585–4589, 2005.
- [47] F. Marken, A. S. Bhambra, D.-H. Kim, R. J. Mortimer, and S. J. Stott, "Electrochemical reactivity of TiO₂ nanoparticles adsorbed onto boron-doped diamond surfaces," *Electrochemistry Communications*, vol. 6, no. 11, pp. 1153–1158, 2004.
- [48] D. V. Bavykin, E. V. Milsom, F. Marken et al., "A novel cation-binding TiO₂ nanotube substrate for electro- and bioelectrocatalysis," *Electrochemistry Communications*, vol. 7, no. 10, pp. 1050–1058, 2005.
- [49] K. Siuzdak, R. Bogdanowicz, M. Sawczak, and M. Sobaszek, "Enhanced capacitance of composite TiO₂ nanotube/boron-doped diamond electrodes studied by impedance spectroscopy," *Nanoscale*, vol. 7, no. 2, pp. 551–558, 2015.
- [50] F. Schuster, M. Hetzl, S. Weiszer et al., "Position-controlled growth of GaN nanowires and nanotubes on diamond by molecular beam epitaxy," *Nano Letters*, vol. 15, no. 3, pp. 1773–1779, 2015.
- [51] F. Schuster, A. Winnerl, S. Weiszer, M. Hetzl, J. A. Garrido, and M. Stutzmann, "Doped GaN nanowires on diamond: structural properties and charge carrier distribution," *Journal of Applied Physics*, vol. 117, no. 4, Article ID 044307, 2015.
- [52] Ü. Özgür, Y. I. Alivov, C. Liu et al., "A comprehensive review of ZnO materials and devices," *Journal of Applied Physics*, vol. 98, no. 4, Article ID 041301, 2005.
- [53] C. X. Wang, G. W. Yang, T. C. Zhang et al., "Fabrication of transparent p-n hetero-junction diodes by p-diamond film and n-ZnO film," *Diamond and Related Materials*, vol. 12, no. 9, pp. 1548–1552, 2003.
- [54] A. B. Djuriić, A. M. C. Ng, and X. Y. Chen, "ZnO nanostructures for optoelectronics: material properties and device applications," *Progress in Quantum Electronics*, vol. 34, no. 4, pp. 191–259, 2010.
- [55] N. K. Reddy, Q. Ahsanulhaq, J. H. Kim, and Y. B. Hahn, "Behavior of n-ZnO nanorods/p-Si heterojunction devices at higher temperatures," *Applied Physics Letters*, vol. 92, no. 4, Article ID 043127, 2008.
- [56] X.-M. Zhang, M.-Y. Lu, Y. Zhang, L.-J. Chen, and Z. L. Wang, "Fabrication of a high-brightness blue-light-emitting diode using a ZnO-Nanowire array grown on p-GaN thin film," *Advanced Materials*, vol. 21, no. 27, pp. 2767–2770, 2009.
- [57] J. B. Baxter and E. S. Aydil, "Epitaxial growth of ZnO nanowires on a- and c-plane sapphire," *Journal of Crystal Growth*, vol. 274, no. 3–4, pp. 407–411, 2005.
- [58] T. Ochiai and A. Fujishima, "Photoelectrochemical properties of TiO₂ photocatalyst and its applications for environmental purification," *Journal of Photochemistry and Photobiology C: Photochemistry Reviews*, vol. 13, no. 4, pp. 247–262, 2012.

Research Article

Fabrication and Characterization of Highly Oriented N-Doped ZnO Nanorods by Selective Area Epitaxy

Yang Zhang,¹ Shulin Gu,¹ Kun Tang,¹ Jiandong Ye,¹ Haixiong Ge,² Zhengrong Yao,¹ Shunming Zhu,¹ and Youdou Zheng¹

¹National Laboratory of Solid State Microstructures, School of Electronic Science & Engineering, Nanjing University, Nanjing 210046, China

²National Laboratory of Solid State Microstructures, Department of Materials Science and Engineering, College of Engineering and Applied Sciences, Nanjing University, Nanjing 210093, China

Correspondence should be addressed to Shulin Gu; slgu@nju.edu.cn and Kun Tang; ktang@nju.edu.cn

Received 28 February 2015; Accepted 15 April 2015

Academic Editor: Meiyong Liao

Copyright © 2015 Yang Zhang et al. This is an open access article distributed under the Creative Commons Attribution License, which permits unrestricted use, distribution, and reproduction in any medium, provided the original work is properly cited.

High-quality nitrogen-doped ZnO nanorods have been selectively grown on patterned and bare ZnO templates by the combination of nanoimprint lithography and chemical vapor transport methods. The grown nanorods exhibited uniformity in size and orientation as well as controllable density and surface-to-volume ratio. The structural and optical properties of ZnO nanorods and the behaviour of N dopants have been investigated by means of the scanning electron microscope, photoluminescence (PL) spectra, and Raman scattering spectra. The additional vibration modes observed in Raman spectra of N-doped ZnO nanorods provided solid evidence of N incorporation in ZnO nanorods. The difference of excitonic emissions from ZnO nanorods with varied density and surface-to-volume ratio suggested the different spatial distribution of intrinsic defects. It was found that the defects giving rise to acceptor-bound exciton (A^0X) emission were most likely to distribute in the sidewall surface with nonpolar characteristics, while the donor bound exciton (D^0X) emission related defects distributed uniformly in the near top polar surface.

1. Introduction

As a direct bandgap semiconductor, with its bandgap of 3.37 eV and binding energy of 60 meV at room temperature, zinc oxide (ZnO) materials in forms of bulk, films, and nanostructures have shown versatile potential applications in electronic and optoelectronic devices, such as sensors [1, 2], light-emitting diodes [3, 4], and solar cells [5]. ZnO nanorods have attracted much attention due to the easy fabrication procedure via various growth techniques including metal-organic chemical vapor deposition (MOCVD) [6], thermal evaporation [7], vapor liquid solid deposition [8, 9], and pulsed laser deposition (PLD) [10]. Besides, the selective area epitaxy of well-aligned high quality ZnO nanostructures has also been achieved [11–13]. In micron scale, conventional photolithography is easy and widely used to achieve the required patterns on the substrates [11], but as the dimension is shrunk into nanometer scale, electron-beam lithography

(EBL) [12, 13] is mostly used. However, EBL is relatively expensive and not suitable for practical application. Alternatively, nanoimprint lithography method [14, 15] provides an available and inexpensive choice for nanoscaled patterning in nanostructures fabrication.

The fabricated ZnO nanorods are usually oriented along c -axis and show weak dependence on the employed substrates. The top surface of ZnO nanorods is in either (0001) or (000 $\bar{1}$) orientation, exhibiting polar nature with Zn or O termination, respectively. A nonpolar (10 $\bar{1}$ 0) surface has the smallest surface formation energy among low index surfaces, and thus, (10 $\bar{1}$ 0) facets would be the major constituting facet of a crystalline ZnO nanomaterial [16]. In fact, the sidewall surface of ZnO nanorods is usually in the (10 $\bar{1}$ 0) direction, which is nonpolar with equal numbers of Zn and O atoms on the surface. Nanometer-sized materials have a high surface-to-volume ratio, which critically affects the electronic and optical properties. In particular, when the ZnO nanorods

have smaller diameters, their surface-to-volume ratios are higher and the surface effect is expected to be more distinguished. The surface effect should have a close correlation with the large density of dangling bonds existing in the sidewall surface of ZnO nanostructures, which have been ascribed to be the intrinsic defects, such as oxygen or zinc vacancies (V_O or V_{Zn}), and have a great effect on the optical properties of the nanorods.

Photoluminescence has been proven to be a powerful tool to study the optical properties of ZnO nanorods. For wide bandgap semiconductors, such as GaN and ZnO, He-Cd laser at the wavelength of 325 nm has been used as the excitation source, which has a small penetration depth of only 60 nm in ZnO material. Thus, the observed photoluminescence in ZnO films is mostly contributed from the region near surface, even taking the contribution of the recombination from the carriers located within the diffusion length of the excited region into account. Therefore, the overall photoluminescence spectra of ZnO nanorods can be regarded as the superposed radiative recombination signals mostly from both the top surface and the sidewall surface. The typical observed complicated ZnO luminescence spectra are then significantly influenced by the crystal morphology, thus leading to the divergence of optical emissions reported on various ZnO nanorods and exhibiting strong dependence on the sizes, morphologies, and growth techniques of ZnO nanostructures.

In fact, the optical properties of different facet ZnO film for both polar and nonpolar surfaces have been investigated. Different polarity surfaces have been found to lead different emission properties, including the kind of the emission and its intensity [17, 18]. For instance, the luminescent properties of the Zn-polar and O-polar faces have been reported to be extremely different: the PL intensity of the Zn-polar face is stronger than that of the O-polar face and the PL intensity of the zero-phonon free excitons relative to that of phonon replicas is stronger in the O-polar face than that in the Zn-polar face. The origin of the observed differences in PL properties has been discussed in terms of the difference of exciton-phonon coupling strengths, opposite band bending effect, and difference of the adsorption [17]. The opposite band bending effects at the two polar faces have been suggested to reduce the absorption effect at the O-polar face compared to the Zn-polar face [19]. As for nanomaterials, the similar differences observed in the CL spectra of O- (FX dominate) and Zn (DX dominate)-polar ZnO nanorods can be directly correlated with the distinct photoluminescence properties in O- and Zn-polar ZnO epilayers and single crystals. It was found that the incorporation of impurities both in terms of concentration and nature may also depend on the polarity of ZnO NWs [20].

Moreover, the high surface-to-bulk ratio and the sidewall nonpolar surface existing in the nanorods may cause the observed emissions to be much more complicated. For nanorods array, the surface will include both the top surface and the sidewall surface, which should have important but different contribution to the observed emissions. Photoluminescence measurement can hardly get detailed information about such spatial distribution of the luminescence

nor related defects on the surface of ZnO nanorods. The different facets in ZnO nanorods surface even aggravate the complication of observed photoluminescence. In contrast to photoluminescence, cathodoluminescence can be easily applied to distinguish the observed emissions from the nanorods and correlate them with the nanorod structures. It is reported that the observed visible emission, which can be related with the existing surface defects, such as zinc or oxygen vacancies [21, 22], comes from the sidewall surface of nanorods. The band edge emission is believed mostly to come from the interior region in the nanorods. This indicates that the light emission spectra of ZnO observed from diverse morphology cannot be directly compared, although some common spectral features are present [23].

Besides the relationship between the existing intrinsic defects and the visible green band emission, the spatial distribution of near band edge emission in ZnO nanorods has also been deeply investigated via photoluminescence. Such inhomogeneity in optical properties of ZnO nanorods has actually been observed via the angular dependent PL measurements. The luminescence detected from the nanorods illuminated with the laser beam parallel to their growth axes shows that the near band emission (NBE) is dominated by the A-line and its LO phonon replicas while the emission collected from the nanorods illuminated from their lateral side exhibits higher contribution of free exciton [24]. The study suggests that Zn interstitials or some other donors are less formed in the sidewall surface, leading to a low carrier concentration within nonpolar facet. However, the investigation of detailed distribution of the above intrinsic defects in the ZnO nanorods is still challenging.

In this paper, the ZnO nanorods doped by nitrogen with different surface-to-bulk ratio have been fabricated on patterned and bar ZnO films, respectively, by a selective area chemical vapor transport (CVT) growth method. The growth mechanism of the ZnO nanorods on SiO_2 patterned and nonpatterned ZnO seed films has been proposed. The correlation of optical emission and defects formation in topmost surface and sidewall surface has been established via surface morphological observation, Raman scattering, and low-temperature photoluminescence spectra. Distinctive shallow acceptors are observed to be preferentially formed on the sidewalls of the nanorods. Concerning the p-type doping in ZnO films which is still challenging, our study paves a way to realize economic and mass-productive controllable growth of well-patterned ZnO nanorods and to enhance the acceptor incorporation efficiency in low-dimension ZnO nanostructures grown at a high substrate temperature.

2. Experimental Details

In order to thoroughly control the uniformity of the crystal orientation and polarity of the nucleation surface, thick ZnO films grown by two-step growth procedure via metal-organic chemical vapor deposition have been used as seed layers for the growth of ZnO nanorods. The seed layer exhibited uniform Zn-polarity and high crystalline quality, as reported elsewhere [25]. A thin SiO_2 barrier layer at a thickness of 60 nm as the selective mask was then deposited on

the as-grown ZnO seed layer by plasma enhanced chemical vapor deposition (PECVD). Then a layer of hot embossing resist material was spin-coated on the SiO₂/ZnO/sapphire substrates. A module of arrayed circular cylinder (200 nm in diameter and 90 nm in height) of 400 nm period was prepared. The subsequent process was the nanoimprint lithography, and followed by this process, the hot embossing resist material was solidified at a higher temperature. The resisting material/SiO₂/ZnO/sapphire substrates were then etched by reactive ion etching process and the rest resisting material was lifted off by dimethylbenzene in ultrasonic cleaner. Thus, diameter and period of the hole can therefore be patterned on SiO₂/ZnO/sapphire substrates at the dimension of 200 nm and the period of 400 nm.

The growth of vertically aligned ZnO nanorods was carried out in a horizontal tube furnace via the chemical vapor transport method without employing any catalysts. The source material was a mixture of high purity ZnO and graphite powders (ZnO : C = 1 : 1 by weight), which was placed in the centre of the quartz tube put in a horizontal furnace operated at the temperature of 950°C. The substrate placed downstream was the prepared ZnO template on sapphire at the thickness of 2 μm grown by the MOCVD method as seed layers. For ZnO nanorods growth, N₂ was used as the carrier gas, while N₂O was of both O and N sources. The flow rates of N₂ and N₂O were 100 sccm and 1 sccm, respectively. A radiofrequency plasma generator was used for the ionization of N₂O to produce both efficient N and O precursors for growth.

To get different intensity and surface-to-volume ratio of ZnO nanorods, three different kinds of samples have been grown. Sample A was grown on the patterned substrate for 20 minutes. Sample B was grown with the same condition but long growth time of 60 min. Sample C was also grown for one hour but directly on ZnO substrate.

The morphology of the as-grown ZnO nanorods was characterized by a 5350 NE Dawson Creek Derive scanning electron microscopy (SEM) attached with energy dispersive analyser. The crystalline quality of all samples was analyzed by X-ray diffraction (XRD) performed on a Rigaku D/MAX-2500 using Cu Kα radiation at 40 kV and 200 mA by step scanning with a step size of 0.02°. The 514 nm Ar⁺ laser with a power of 5 mW was used as the excitation source in micro-Raman spectroscopy at RT and the measurement was performed under a backscattering configuration. Photoluminescence spectra were recorded in the temperature of 9 K, excited by a He–Cd laser with a wavelength of 325 nm. The laser beam was impinged on the sample surface with an angle of approximately 60°. The excited PL emission was measured with a JY-Horiba monochromator, aligned normal to the sample surface. The chemical configuration of the elements was determined by X-ray photoelectron spectrometry with an Al Kα X-ray monochromatic source at 1486.6 eV (Thermo Fisher Scientific Inc., Model K-Alpha).

3. Results and Discussions

Figure 1 shows the scanning electron microscope images of ZnO nanorods grown in different conditions. From sample

A (Figure 1(a)), it can be clearly seen that ZnO nanorods were achieved only in the area of exposed ZnO layers, while on SiO₂ layers no growth occurred, which shows that ZnO nanorods grew selectively on ZnO and SiO₂ substrates. It can also be seen that ZnO nanorods have different growth density and size distribution on both substrates. On bare ZnO substrates, ZnO nanorods have a dense distribution, the diameter of which mostly ranges from 150 nm to 400 nm (Figure 1(f)). While on patterned ZnO substrates, ZnO nanorods of sample B were evenly distributed and the size of them was concentrated at 720 nm (Figure 1(e)). Consequently, we can conclude that, on patterned ZnO substrates, the growth of ZnO nanorods can be precisely controlled and we can get good ZnO nanorod arrays.

It is noted that the density of ZnO nanorods grown on sample B (Figure 1(b)) is about one-fifth that obtained on sample C (Figure 1(c)), but the averaged size is about 3 times larger than that of sample C. As shown in Figure 2, for the above ZnO nanorods growth on barely or patterned ZnO film, the density and size of ZnO nanorods are finally determined by the formation of the initial nucleus on the substrate. For bare ZnO film (Figure 2(b)), the whole surface is available for the formation of the nucleation sites for ZnO nanorods growth (Figure 2(b)(1)), so the size of the nucleus will be decided by the unoccupied space between the neighbored nuclei, which determine the amount of adsorbed radicals which may be possible to migrate into the nucleus and so contribute to the growth of the initial nucleus. For the growth conditions as employed in the work, almost the whole surface will be covered by the grown ZnO nanorods (Figure 2(b)(2)). For patterned ZnO film in the work (Figure 2(a)), only partial ZnO surface is exposed to the ambient growth (Figure 2(a)(1)). However, the adsorption reaction radicals on the covered SiO₂ surface have a high migration rate and can also move and incorporate with the nucleation sites (Figure 2(a)(2)), resulting in a much larger nucleus (Figure 2(a)(3)). In this case, much larger sizes of ZnO should be formed on sample B. According to the scanning electron microscopy image, we get the distribution of the ZnO nanorods size and number for both cases, which agree well with the above suggestion and discussion.

The XRD spectra of samples A, B, and C are shown in Figure 3. The inset shows the ZnO (0002) rocking curve (XRC) for all the samples. From the ω-2θ patterns, it can be seen that only the ZnO (0002) diffraction peaks have been detected, indicative of the desired c-axis preferential growth for the ZnO nanorods. Furthermore, the intensity of the (0002) peak drops for sample C, and the width of the ω rocking curves increases from 297 arc sec (sample A) and 276 arc sec (sample B) to 423 arc sec (sample C). The decreased XRD intensity and the increased XRC width for sample C have been ascribed to the relatively degraded crystalline quality of the grown nanorods as compared to the ZnO seed film, since the grown nanorods are much denser and will contribute more to the detected XRD patterns.

For photoluminescence measurements on ZnO nanorods array, the space between the neighbored nanorods will have a great effect. Small space like the case of nanorods grown on sample C should give a little contribution from the sidewall

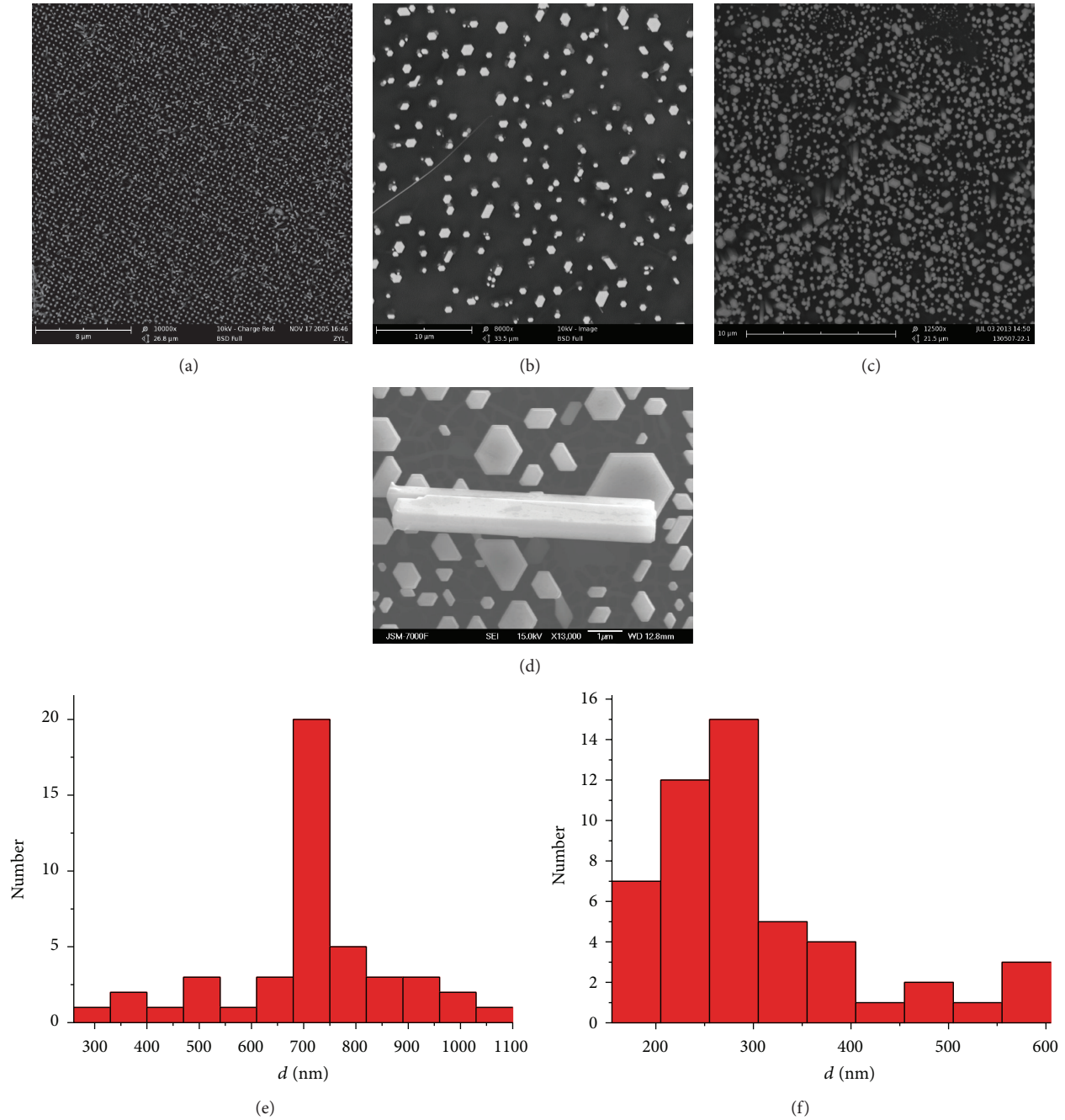


FIGURE 1: SEM images (a, b, c) of ZnO nanorods grown on patterned (a: sample A and b: sample B) and bare (c: sample C) ZnO substrates. (d) An amplified image of the ZnO nanorods, showing dense hexagonal nanorods in the size of tens to hundreds of nanometers. (e) and (f) The plot of the nanorod number versus the nanorod size distribution (e: sample B, f: sample C).

surface to the final emission, due to limited penetration depth of the incident laser and also less collection of the emission from the sidewall surface. However, a large space similar to the case on sample B should certainly give a high contribution from the sidewall surface. Considering the fact that the top surface coverage is lower than that of sample C, the contribution from the top surface for sample B might be weaker than the case for sample C. Therefore, the emission intensity ratio for the contribution from the top surface

over the sidewall surface can be moderated and the different contribution may be evaluated in the work.

Figure 4 shows the photoluminescence (PL) spectra of samples A, B, and C measured at 9 K. The features of PL spectra can be classified into two categories: near band emission (around 3.3 eV) and deep band emission (around 2.5 eV) [19]. During PL test, the sample was vertically placed and the laser irradiated to the nanorods with an angle of about 60° . The near band emissions of PL spectra of samples A, B,

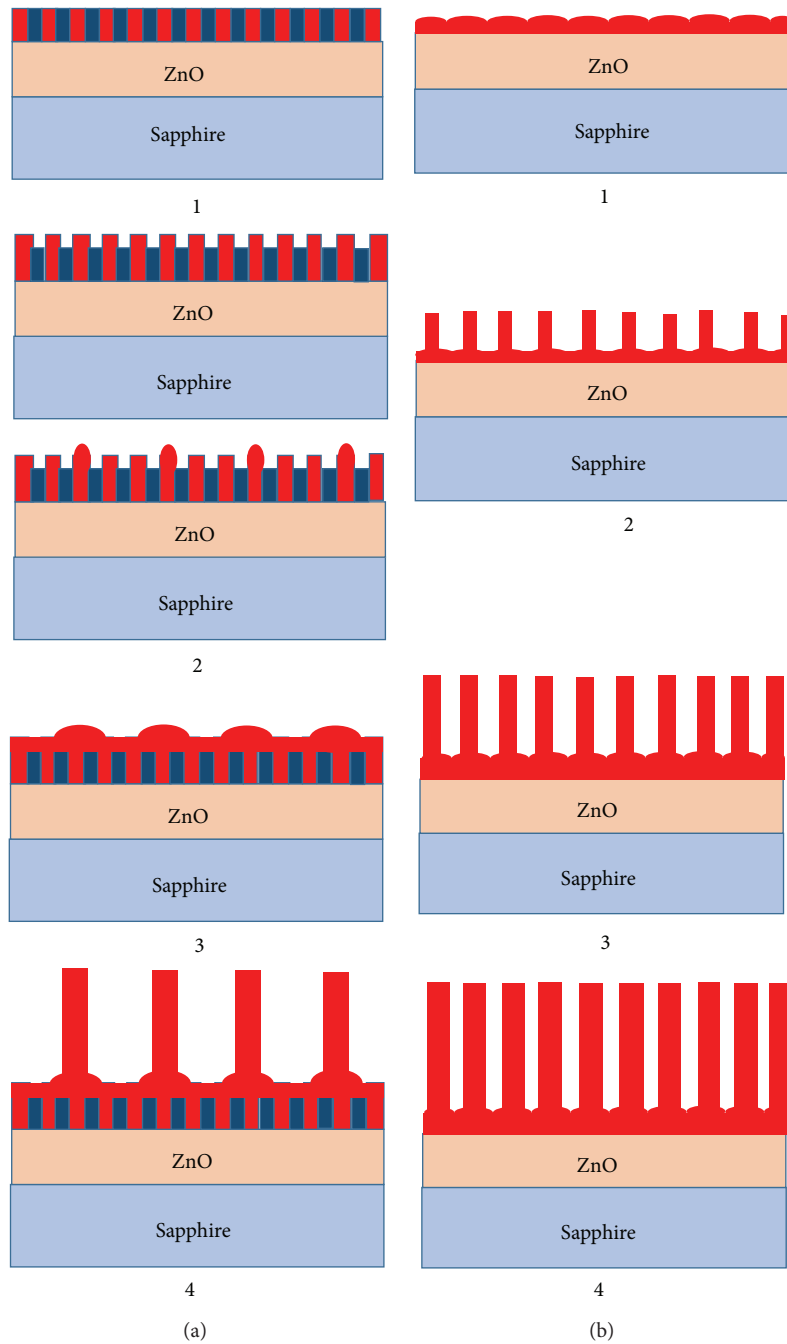


FIGURE 2: Growth illustrations of ZnO nanorods on patterned (a) and bare (b) substrates.

and C are shown in Figure 4(b). For sample A at the initial state of growth, small nanodisks covered the open areas on the patterned SiO_2/ZnO substrate. The dominating emission located at 3.362 eV, which is due to recombination of excitons bound to donors or acceptors and similar to the observation on the patterned SiO_2/ZnO substrate due to large open area of the SiO_2/ZnO substrate. As the MOCVD grown ZnO film is generally n-type, the peak at 3.362 eV can be recognized as D^0X [26]. Besides, a new peak at 3.368 eV appears which can be ascribed to the surface exciton SX, which is observed in

the ZnO films and more apparent in the ZnO nanostructures due to a large surface-to-volume ratio.

Compared with sample A, more ZnO nanorods have been grown on sample B. It is interesting to note that a broad peak located at 3.359 eV dominated in the spectrum, which can be easily resolved into two peaks, 3.358 eV and 3.362 eV, respectively. The emission around 3.358 eV has been previously ascribed as acceptor bound exciton (A^0X), and the later one should be the D^0X as described in sample A. The intensity of A^0X on sample B is much stronger than that in sample

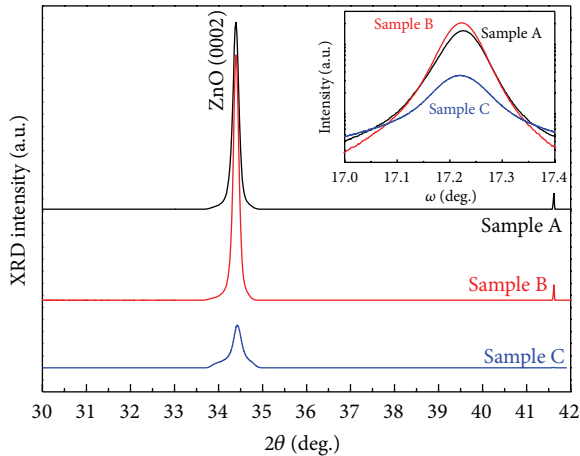


FIGURE 3: XRD patterns for all the samples. The inset shows the ω -scan rocking curves.

A, where a shoulder located at 3.358 eV can be devolved too besides the main emission peak at 3.362 eV. Similarly, the surface exciton has also been intensified compared with sample A due to more contribution from the grown nanorods. As more dense nanorods were grown on sample C, it was expected to have a stronger A^0X emission. However, opposite phenomenon is revealed as shown in Figure 4, where the main emission peak has been shifted to high energy located at 3.363 eV. Of course, a small shoulder located at 3.358 eV can be devolved from the peak, but its intensity has become much smaller compared with sample B. The peak-fitting result of PL spectrum shows that the intensity of A^0X (3.358 eV) in sample C is much smaller than that of sample B. As the nanorods coverage in sample C is much higher, it suggested that the photoemission excited and collected from the sidewalls of the nanorods will be much smaller. The change trend of A^0X emission and surface exciton SX emission for samples A, B, and C surely indicates that the A^0X and SX should mainly originate from the sidewall surface with a small fraction comes from the top surface. The change of the D^0X emission has also revealed high donor concentration contribution from the near top surface compared to the sidewall surface.

Calculation results on the formation energy of Zn vacancies at different positions in the slab reveal that Zn vacancies are much more probably closer to the (1010) surface (1 eV energy lower) than inner positions in the slab [27]. This has also been supported by another report, which indicates V_{Zn} on a nonpolar $(10\bar{1}0)$ surface had significantly smaller formation energy than it did in the bulk [28]. Considering the fact that the sidewall surface is $(1010)/(10\bar{1}0)$ direction, the A^0X emission can probably be relevant to V_{Zn} .

Figure 5 shows the green band emission of samples A, B, and C at temperature 9 K. It is interesting that fine structure, which consists mainly of doublets, can be observed. The energy spacing between any two adjacent lines (LO phonon replicas) in the fine structure is about 72 meV. The number of LO-replicas that can be clearly seen is eight. At high energy side, two well-resolved series superimposing the broad band

can be observed. Both of the two series equally separate fine structures and the energy spacing between them is about 27 meV. The intensity of the GB for sample C is obviously stronger than that of sample B, which agrees well with the coverage of the ZnO nanorods as shown above. This indicates that the GB is mainly contributed from the ZnO nanorods and contribution from the ZnO film does not need to be taken into account here.

Raman scattering spectra of samples A, B, and C with incident light parallel to the c -axis of the nanorods have been shown in Figure 6. As indicated in the above discussion, the observed emissions in the PL measurements should occur from the top surface or the sidewall surface. Different to what happened in the PL measurements, the excitation laser photon energy for Raman scattering is smaller than the bandgap of ZnO, indicating that almost scattering from both the ZnO nanorods and ZnO film can contribute to the Raman spectroscopy. In Figure 6, the observed peaks located at 99, 332, and 438 cm^{-1} are the classical modes of ZnO, corresponding to $E_2(\text{low})$, $2E_2(\text{M})$, and $E_2(\text{high})$, respectively, which should come from both ZnO nanorods and films [29, 30]. In addition to the ZnO modes, peaks around 276, 510, 582, and 644 cm^{-1} are observed, with their intensity increased for samples A, B to C. The origin of these additional modes was controversial. They were assigned to N local vibrational modes, or ZnO silent modes allowed by the breakdown of the translational crystal symmetry, or Zn interstitial clusters due to N incorporation [31–33]. Regardless of the assignments, the increased intensity of the vibration modes indicates that it is contributed from the ZnO nanorods, not from the ZnO seed film. And N atoms have been incorporated into the ZnO nanorods.

The incorporation of nitrogen has been proven by XPS. Figure 7 shows the N 1s XPS line for sample C. An indistinct nitrogen signal could be seen with a high level of noise due to the low nitrogen concentration. Considering the fact that the nanorods were grown at 950°C, at which the nitrogen solubility will drop sharply, the incorporation of nitrogen is thus low. For samples A and B, due to the looser distribution of the nanorods, it is difficult to get the nitrogen signals, while, for sample C, the density of the nanorods is much higher and hence a weak signal of nitrogen could be detected shown in Figure 7. It is surprising that a small amount of nitrogen can still exist in the nanorods grown at such a high substrate temperature. It is highly possible that the nitrogen atoms could be stabilized via bonding with interstitial zinc defects, forming the Zn_i-N_O complexes, which has been proposed to be thermally stable. This proposal could be partially evidenced by the fact that the Zn_i related Raman vibration mode at 276 cm^{-1} is strongest for sample C.

As for the assignment of the acceptor, nitrogen substituting for oxygen, N_O , is calculated to be a deep acceptor. On the other hand, the acceptor ionization energy is predicted to be significantly reduced by the presence of various intrinsic defects that can act as efficient compensating centers and also facilitate formation of various N-related complexes, including donor or acceptor complexes such as Zn_i-N_O or $V_{Zn}-N_O$. In our case, we prefer to ascribe the observed acceptor to $V_{Zn}-N_O$ or even Zn vacancy clusters, or Zn vacancy

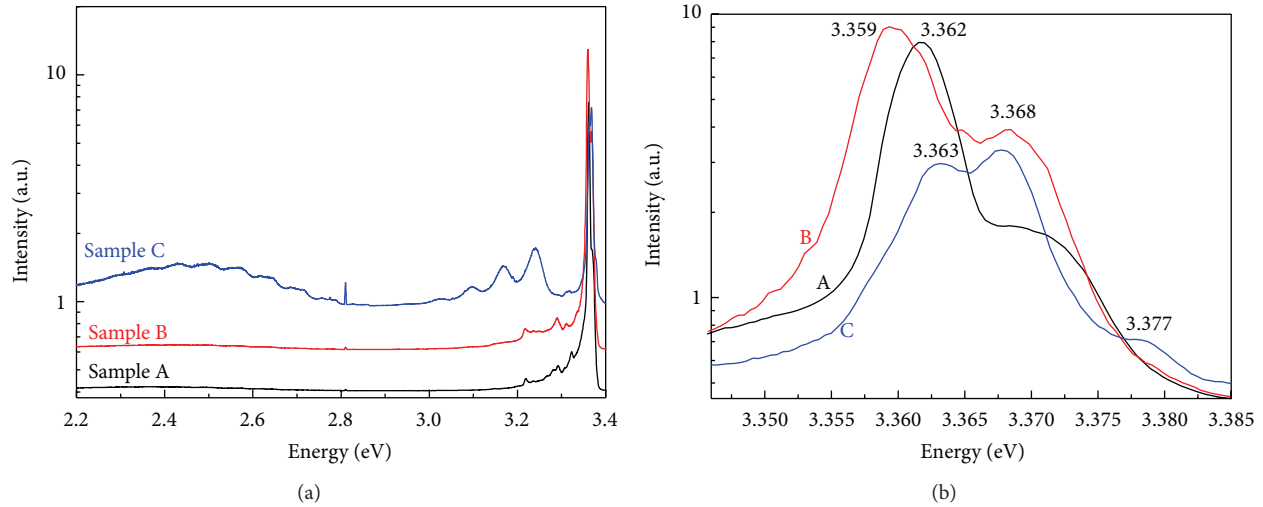


FIGURE 4: PL spectra of samples A, B, and C at 9 K. (a) Full spectra from 2.2 to 3.4 eV; (b) near band edge spectra from 3.345 to 3.385 eV.

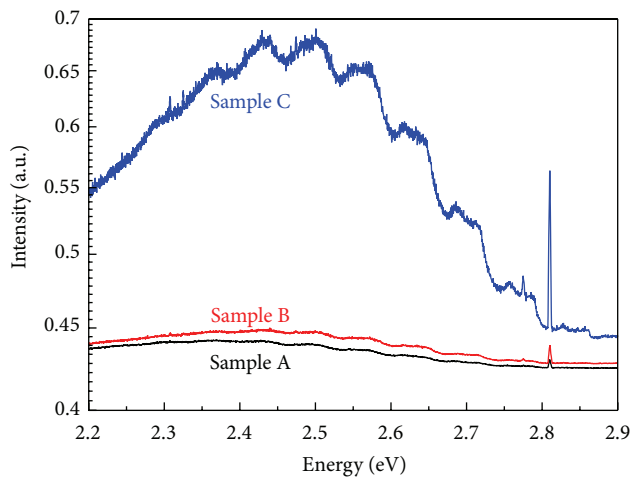


FIGURE 5: Green band emission of PL spectra of samples A, B, and C.

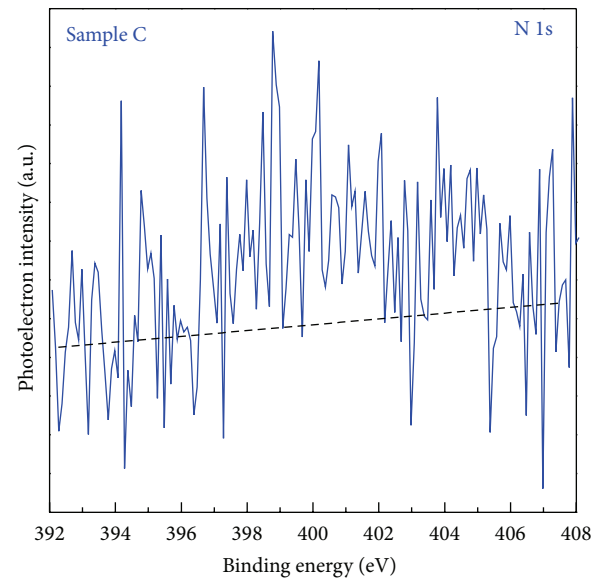


FIGURE 7: Nitrogen 1s XPS line of sample C.

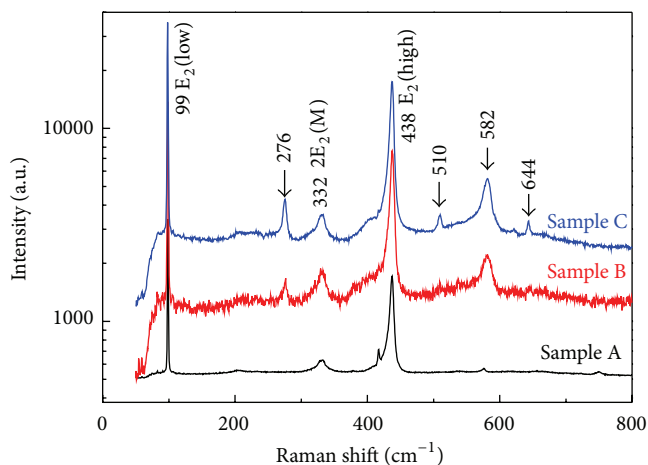


FIGURE 6: Raman scattering spectra of samples A, B, and C.

related complex should be a better description of the shallow acceptor. These acceptors are believed to locate near the sidewall surface according to the enhanced A⁰X emission observed in sample B, possibly due to the modification of large surface-to-volume ratio on the formation energy of the acceptors.

4. Conclusions

The paper illustrates different growth process of ZnO nanorods on patterned and bare ZnO substrates. ZnO nanorods of different intensity and different surface-to-volume ratio have been grown. From the PL test, we can see that the defects in ZnO nanorods are not uniformly distributed in the slab. The A⁰X emission related defects, which

may be relevant to V_{Zn} , are more likely to distribute in the sidewall surface, while D^0X related defects uniformly distribute in the near top surface. The Raman spectra ensure the fact that N atoms have been incorporated into the ZnO nanorods. Our work infers how to realize the modification on the formation energy of the acceptor, like the effect of the large surface-to-volume ratio, which is critical for the realization of the p-type doping in ZnO films.

Conflict of Interests

The authors declare that there is no conflict of interests regarding the publication of this paper.

Acknowledgments

This research was supported by the State Key Program for Basic Research of China under Grant no. 2011CB302003, National Natural Science Foundation of China (nos. 6103020, 60990312, 61274058, and 61322403), Basic Research Program of Jiangsu Province (BK20130013), and the Priority Academic Program Development of Jiangsu Higher Education Institutions.

References

- [1] J. B. K. Law and J. T. L. Thong, "Simple fabrication of a ZnO nanowire photodetector with a fast photoresponse time," *Applied Physics Letters*, vol. 88, no. 13, Article ID 133114, 2006.
- [2] M. S. Arnold, P. Avouris, Z. W. Pan, and Z. L. Wang, "Field-effect transistors based on single semiconducting oxide nanobelts," *Journal of Physical Chemistry B*, vol. 107, no. 3, pp. 659–663, 2003.
- [3] R. Könenkamp, R. C. Word, and C. Schlegel, "Vertical nanowire light-emitting diode," *Applied Physics Letters*, vol. 85, no. 24, pp. 6004–6006, 2004.
- [4] H. T. Ng, J. Han, T. Yamada, P. Nguyen, Y. P. Chen, and M. Meyyappan, "Single crystal nanowire vertical surround-gate field-effect transistor," *Nano Letters*, vol. 4, no. 7, pp. 1247–1252, 2004.
- [5] M. Law, L. E. Greene, J. C. Johnson, R. Saykally, and P. D. Yang, "Nanowire dye-sensitized solar cells," *Nature Materials*, vol. 4, pp. 455–459, 2005.
- [6] J. Y. Park, Y. S. Yun, Y. S. Hong, H. Oh, J.-J. Kim, and S. S. Kim, "Synthesis, electrical and photoresponse properties of vertically well-aligned and epitaxial ZnO nanorods on GaN-buffered sapphire substrates," *Applied Physics Letters*, vol. 87, no. 12, Article ID 123108, pp. 1–3, 2005.
- [7] Y. Zhang, H. Jia, R. Wang et al., "Low-temperature growth and Raman scattering study of vertically aligned ZnO nanowires on Si substrate," *Applied Physics Letters*, vol. 83, no. 22, pp. 4631–4633, 2003.
- [8] C. H. Wang, A. S. W. Wong, and G. W. Ho, "Facile solution route to vertically aligned, selective growth of ZnO nanostructure arrays," *Langmuir*, vol. 23, no. 24, pp. 11960–11963, 2007.
- [9] Y. Tak and K. Yong, "Controlled growth of well-aligned ZnO nanorod array using a novel solution method," *Journal of Physical Chemistry B*, vol. 109, no. 41, pp. 19263–19269, 2005.
- [10] Y.-J. Kim, C.-H. Lee, Y. J. Hong, G.-C. Yi, S. S. Kim, and H. Cheong, "Controlled selective growth of ZnO nanorod and microrod arrays on Si substrates by a wet chemical method," *Applied Physics Letters*, vol. 89, no. 16, Article ID 163128, 2006.
- [11] Q. Ahsanulhaq, S. H. Kim, and Y. B. Hahn, "Hexagonally patterned selective growth of well-aligned ZnO nanorod arrays," *Journal of Alloys and Compounds*, vol. 484, pp. 17–20, 2009.
- [12] H. Wang, Z. P. Zhang, X. N. Wang et al., "Selective growth of vertical-aligned ZnO nanorod arrays on si substrate by catalyst-free thermal evaporation," *Nanoscale Research Letters*, vol. 3, no. 9, pp. 309–314, 2008.
- [13] A. Qurashi, J. H. Kim, and Y. B. Hahn, "Density-controlled selective growth of well-aligned ZnO nanorod arrays by a hybrid approach," *Superlattices and Microstructures*, vol. 48, no. 2, pp. 162–169, 2010.
- [14] L. Ressler, E. Palleau, and S. Behar, "Electrical nano-imprint lithography," *Nanotechnology*, vol. 23, no. 25, Article ID 255302, 2012.
- [15] K.-B. Choi and J. J. Lee, "Passive compliant wafer stage for single-step nano-imprint lithography," *Review of Scientific Instruments*, vol. 76, no. 7, Article ID 075106, 2005.
- [16] B. Meyer and D. Marx, "Density-functional study of the structure and stability of ZnO surfaces," *Physical Review B*, vol. 67, Article ID 035403, 2003.
- [17] D. C. Oh, T. Kato, H. Goto et al., "Comparative study of photoluminescences for Zn-polar and O-polar faces of single-crystalline ZnO bulks," *Applied Physics Letters*, vol. 93, no. 24, Article ID 241907, 2008.
- [18] M. W. Allen, P. Miller, R. J. Reeves, and S. M. Durbin, "Influence of spontaneous polarization on the electrical and optical properties of bulk, single crystal ZnO," *Applied Physics Letters*, vol. 90, no. 6, Article ID 062104, 2007.
- [19] A. Yamamoto, Y. Moriwaki, K. Hattori, and H. Yanagi, "A comparative study of photoluminescence of Zn-polar and O-polar faces in single crystal ZnO using moment analysis," *Applied Physics Letters*, vol. 98, no. 6, Article ID 061907, 2011.
- [20] V. Consonni, E. Sarigiannidou, E. Appert et al., "Selective area growth of well-ordered ZnO nanowire arrays with controllable polarity," *ACS Nano*, vol. 8, no. 5, pp. 4761–4770, 2014.
- [21] C. Klingshirm, J. Fallert, H. Zhou et al., "65 years of ZnO research—old and very recent results," *Physica Status Solidi B*, vol. 247, no. 6, pp. 1424–1447, 2010.
- [22] A. B. Djuriić, A. M. C. Ng, and X. Y. Chen, "ZnO nanostructures for optoelectronics: material properties and device applications," *Progress in Quantum Electronics*, vol. 34, no. 4, pp. 191–259, 2010.
- [23] V. Khranovskyy, V. Lazorenko, G. Lashkarev, and R. Yakimova, "Luminescence anisotropy of ZnO microrods," *Journal of Luminescence*, vol. 132, no. 10, pp. 2643–2647, 2012.
- [24] S. S. Kurbanov, H. D. Cho, and T. W. Kang, "Effect of excitation and detection angles on photoluminescence spectrum from ZnO nanorod array," *Optics Communications*, vol. 284, no. 1, pp. 240–244, 2011.
- [25] H. Chen, S. Gu, K. Tang et al., "Origins of green band emission in high-temperature annealed N-doped ZnO," *Journal of Luminescence*, vol. 131, no. 6, pp. 1189–1192, 2011.
- [26] J. Xu, R. Ott, A. S. Sabau et al., "Generation of nitrogen acceptors in ZnO using pulse thermal processing," *Applied Physics Letters*, vol. 92, no. 15, Article ID 151112, 2008.
- [27] F. Fabbri, M. Villani, A. Catellani et al., "Zn vacancy induced green luminescence on non-polar surfaces in ZnO nanostructures," *Scientific Reports*, vol. 4, article 5158, 2014.

- [28] K. Chae, Y. C. Chung, and H. Kim, "Ferromagnetism induced by vacancies in bulk and the (1010) surfaces of ZnO: density functional theory calculations," *Japanese Journal of Applied Physics*, vol. 50, Article ID 01BE05, 2011.
- [29] R. H. Callender, S. S. Sussman, M. Selders, and R. K. Chang, "Dispersion of Raman cross section in CdS and ZnO over a wide energy range," *Physical Review B*, vol. 7, no. 8, pp. 3788–3798, 1973.
- [30] F. Decremps, J. Pellicer-Porres, A. M. Saitta, J.-C. Chervin, and A. Polian, "High-pressure Raman spectroscopy study of wurtzite ZnO," *Physical Review B*, vol. 65, no. 9, Article ID 092101, 4 pages, 2002.
- [31] A. Kaschner, U. Haboeck, M. Strassburg et al., "Nitrogen-related local vibrational modes in ZnO:N," *Applied Physics Letters*, vol. 80, no. 11, pp. 1909–1911, 2002.
- [32] X. Zhu, H.-Z. Wu, D.-J. Qiu et al., "Photoluminescence and resonant Raman scattering in N-doped ZnO thin films," *Optics Communications*, vol. 283, no. 13, pp. 2695–2699, 2010.
- [33] S. J. Jokela and M. D. McCluskey, "Unambiguous identification of nitrogen-hydrogen complexes in ZnO," *Physical Review B*, vol. 76, Article ID 193201, 2007.

Research Article

Enhancement of Two-Dimensional Electron-Gas Properties by Zn Polar ZnMgO/MgO/ZnO Structure Grown by Radical-Source Laser Molecular Beam Epitaxy

Li Meng,^{1,2,3} Jingwen Zhang,^{1,2,3} Qun Li,^{1,2,3} and Xun Hou¹

¹Key Laboratory of Photonics Technology for Information, Xi'an Jiaotong University, Xi'an, Shaanxi 710049, China

²Key Laboratory for Physical Electronics and Devices under Ministry of Education, Xi'an Jiaotong University, Xi'an, Shaanxi 710049, China

³Joint Laboratory of Functional Materials and Devices for Informatics, Xi'an Jiaotong University and Institute of Semiconductors, CAS, Xi'an, Shaanxi 710049, China

Correspondence should be addressed to Jingwen Zhang; jwzhang@mail.xjtu.edu.cn

Received 19 January 2015; Accepted 9 March 2015

Academic Editor: Meiyong Liao

Copyright © 2015 Li Meng et al. This is an open access article distributed under the Creative Commons Attribution License, which permits unrestricted use, distribution, and reproduction in any medium, provided the original work is properly cited.

A Zn polar ZnMgO/MgO/ZnO structure with low Mg composition Zn_{1-x}Mg_xO layer ($x = 0.05$) grown on a-plane (11-20) sapphire by radical-source laser molecular beam epitaxy was reported. The insertion of a thin (1 nm) MgO layer between ZnMgO and ZnO layers in the ZnMgO/ZnO 2DEG structures results in an increase of 2DEG sheet density and affects electron mobility slightly. The carrier concentration reached a value as high as $1.1 \times 10^{13} \text{ cm}^{-2}$, which was confirmed by *C-V* measurements. A high Hall mobility of $3090 \text{ cm}^2/\text{Vs}$ at 10 K and $332 \text{ cm}^2/\text{Vs}$ at RT was observed from Zn_{0.95}Mg_{0.05}O/MgO/ZnO heterostructure. The choice of the thickness of MgO was discussed. The dependence of carrier sheet density of 2DEG on ZnMgO layer thickness was calculated in theory and the theoretical prediction and experimental results agreed well.

1. Introduction

ZnO and its heterostructures, which have several advantages including a high saturation velocity [1], a large conduction band offset for ZnMgO/ZnO heterostructures [2], and the possibility to form a high-density two-dimensional electron-gas (2DEG) [3], have great potential for high-frequency and high-power device applications. So far, the formation of 2DEG at Zn polar Zn_{1-x}Mg_xO/ZnO interface has been observed by a few groups using molecular beam epitaxy (MBE) [4–8], pulse laser deposition (PLD) techniques [9], metal-organic vapor phase epitaxy (MOVPE) [10], and RF sputtering [11]. However, in low Mg composition Zn_{1-x}Mg_xO/ZnO heterostructures ($x < 0.1$) high electron mobility can be observed but with very low 2DEG sheet density ($n < 10^{12} \text{ cm}^{-2}$) [12], and in high Mg composition Zn_{1-x}Mg_xO/ZnO heterostructures ($x > 0.1$), 2DEG sheet density reached a considerable value ($10^{12} \sim 10^{13} \text{ cm}^{-2}$) but

electron mobility is still deeply affected by alloy disorder scattering, especially at low temperatures. In addition the obtained mobility in previous papers was lower than $250 \text{ cm}^2/\text{Vs}$ at RT [13]. It has been reported that modified AlGaIn/AlN/GaN structures, which employ a thin AlN interfacial layer between AlGaIn and GaN layers, show higher 2DEG properties than those of conventional AlGaIn/GaN structures. This is reported to be a result of the reduction of alloy disorder scattering due to the suppression of carrier penetration from the GaN channel into the AlGaIn layer [14–17]. However, the inserting of MgO into ZnMgO/ZnO structure has never been reported. In this work, we report a Zn polar ZnMgO/MgO/ZnO structure to enhance two-dimensional electron-gas properties and discuss the dependence of carrier sheet density of 2DEG on ZnMgO layer thickness which was calculated in theory and the theoretical prediction and experimental results agreed well.

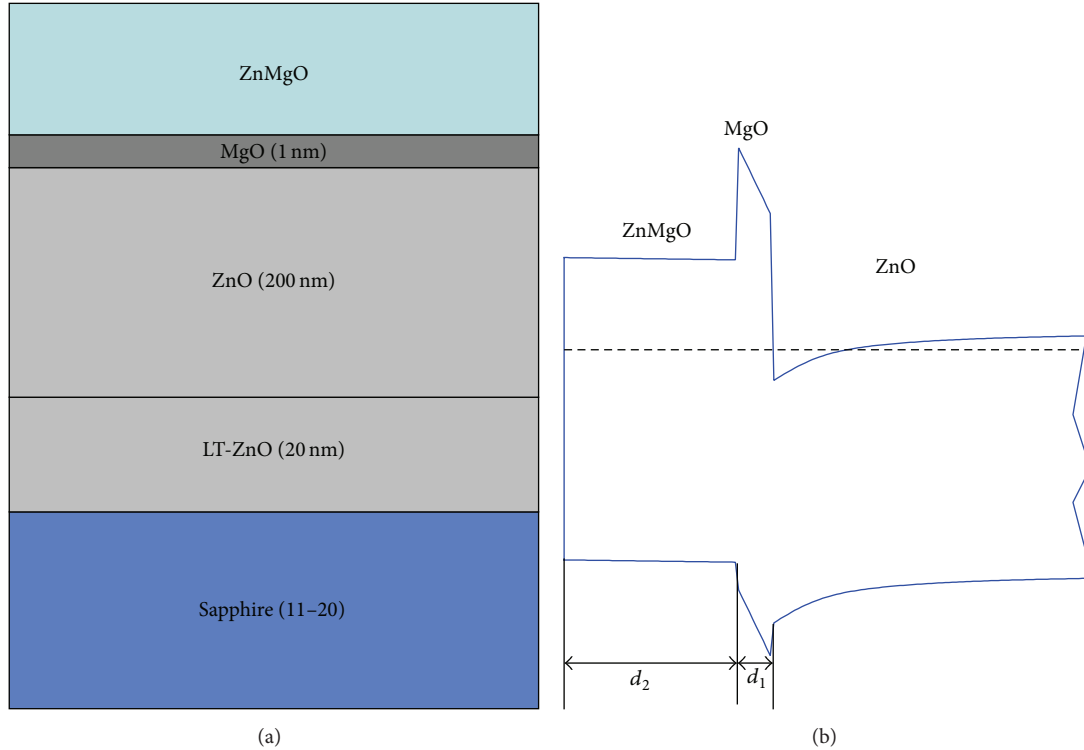


FIGURE 1: Layer structure (a) and band diagram (b) for a Zn polar ZnMgO/MgO/ZnO heterostructure. The growth direction is $\langle 0001 \rangle$ for Zn polarity.

2. Materials and Methods

Zn polar ZnMgO/ZnO and ZnMgO/MgO/ZnO heterostructures were all grown on sapphire (11-20) substrates by radical-source laser molecular beam epitaxy (RS-LMBE) system (Shenyang Scientific Instrument Co., Ltd., Chinese Academy of Sciences (SKY)). The 5N purity of ZnO target was vaporized by KrF excimer laser (Lambda Physik, COMPex 102, 248 nm, 1–20 Hz, 100 mJ). At first, the substrates were treated by nitrogen plasma, which was ionized by radio-frequency (rf) plasma source (Oxford Applied Research, HD-25) at 700°C for 1 h to obtain nitrogen polarity surface and control the growth of single-domain Zn polar ZnO film [18]. The growth was conducted in an oxygen pressure of 10^{-3} Pa. A 20 nm thick low temperature- (LT-) ZnO buffer layer was deposited at 250°C. Secondly, a 200 nm undoped ZnO layer was deposited at 700°C. Finally, an undoped ZnMgO layer was grown at 400°C. For ZnMgO/MgO/ZnO heterostructures (Figure 1(a)), the MgO was deposited before the growth of ZnMgO layer under same condition with ZnMgO layer. The crystalline qualities of the thin films were studied by Philips X'Pert PW3040 high resolution X-ray diffraction (XRD) system using Cu $K\alpha$ ($\lambda = 0.15406$ nm). The growth evolution of MgO layer and the choice of its thickness were investigated by the streaky patterns of the reflection high-energy electron diffraction (RHEED). The Mg composition (x) was determined from the reflectance measurement of the exciton band gap energy of $Zn_{1-x}Mg_xO$ using the equation $E_g(x) = E_g(0) + 2.145x$ [19]. The crystal

polarity was determined based on differences in etching-rate between Zn polar and O-polar samples. Chemical wet etching was carried out using 0.01 M hydrochloric acid solution at room temperature, for etching-rate measurements [20]. The capacitance-voltage (C-V) measurement was performed by using mercury contacts. The electrical properties were examined by Lake Shore 7707A Hall mobility system in a van der Pauw configuration with a magnetic-field of 1000 G.

3. Results and Discussion

3.1. The Thickness of the MgO Insert Layer. To optimize the MgO thickness and make sure that the MgO has grown as wurtzite structure, the growth evolution of MgO layer was investigated by RHEED pattern, shown as in Figure 2. Initially, the MgO layer grew 2-dimensionally on c-ZnO as the thickness was 0.5 and 1 nm in Figures 2(a) and 2(b). Then the growth mode of MgO layer changes from 2-dimensional to 3-dimensional. When the MgO thickness was 1.5 nm, the RHEED spots appeared (Figure 2(c)), which suggests that the crystal structure of the MgO layer changes with increasing layer thickness. Therefore, in this paper, a 1 nm MgO layer was chosen.

3.2. Structural Property. Figure 3 shows the XRD spectra for the grown ZnMgO/MgO/ZnO structure on sapphire substrate. Because of the low concentration of Mg in the ZnMgO layer, the ZnO (0002) peak and ZnMgO (0002) are overlapped. The crystal quality of the $Zn_{0.95}Mg_{0.05}O/MgO/ZnO$

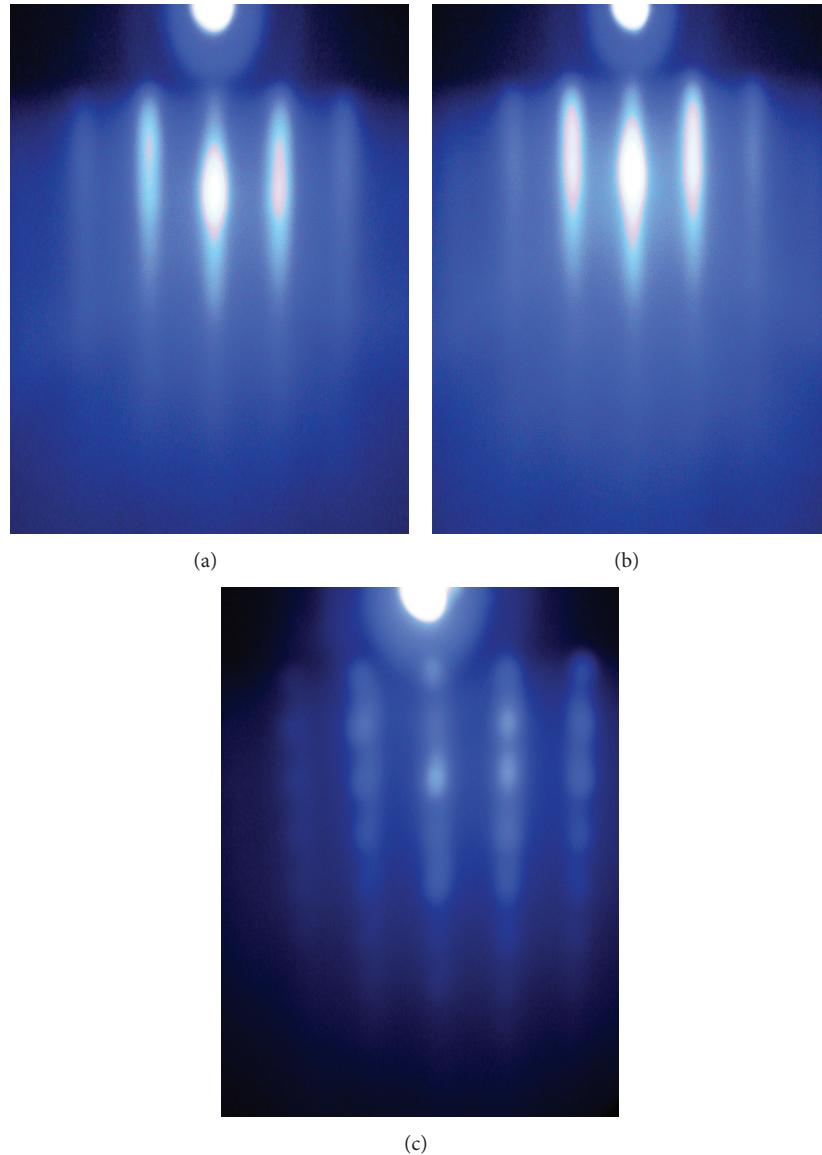


FIGURE 2: The evolution of RHEED pattern during growth of the MgO layer. The direction of MgO is $\langle 11\bar{2}0 \rangle$. (a) The thickness of the MgO buffer layer is 0.5 nm; (b) thickness of MgO = 1 nm; and (c) thickness of MgO = 1.5 nm.

structure was characterized by a cross-sectional TEM image (JEM-2100F). A typical image recorded near the ZnMgO/MgO/ZnO interface is shown in the inset of Figure 3. The interface could not be detected in the TEM micrograph clearly, which suggests that the structure has a high degree of crystalline quality. The MgO has no phase transition from wurtzite structure to rock salt structure. High electron mobility will benefit from the enhanced structure and crystal quality. It also can be observed that the MgO interfacial layer is grown with a thickness of approximately 1 nm, which corresponds to the designed thickness.

3.3. Electrical Property. Figure 4 displays carrier density derived from capacitance as a function of distance from the top surface for the $\text{Zn}_{0.95}\text{Mg}_{0.05}\text{O}/\text{ZnO}$ and

$\text{Zn}_{0.95}\text{Mg}_{0.05}\text{O}/\text{MgO}/\text{ZnO}$ structures, and both of the thicknesses of $\text{Zn}_{0.95}\text{Mg}_{0.05}\text{O}$ layers are 100 nm. It shows that high concentration 2DEG was confined at the interface. Formation of 2DEG at the interface was demonstrated by the features. Comparing with $\text{Zn}_{0.95}\text{Mg}_{0.05}\text{O}/\text{ZnO}$ structure, a sharp 2DEG peak is shown around interface in $\text{Zn}_{0.95}\text{Mg}_{0.05}\text{O}/\text{MgO}/\text{ZnO}$ structure without penetration into the $\text{Zn}_{1-x}\text{Mg}_x\text{O}$ layer, which behaves similarly with previous report about AlGaIn/AlN/GaN [14]. From these results, it can be concluded that the thin MgO interfacial layer effectively suppresses carrier penetration into the ZnMgO layer and enhances the confinement of 2DEG in ZnO channel. In addition, a sheet carrier concentration of $1.1 \times 10^{13} \text{ cm}^{-2}$ was observed in the $\text{Zn}_{0.95}\text{Mg}_{0.05}\text{O}/\text{MgO}/\text{ZnO}$ structure with 20 nm thick $\text{Zn}_{0.95}\text{Mg}_{0.05}\text{O}$ layer confirmed by

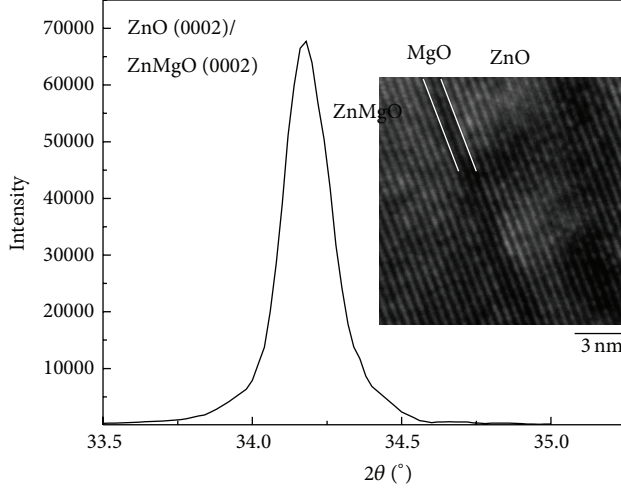


FIGURE 3: The XRD spectra for the grown ZnMgO/MgO/ZnO structure; the inset is the cross-sectional TEM image of a ZnMgO/MgO/ZnO film.

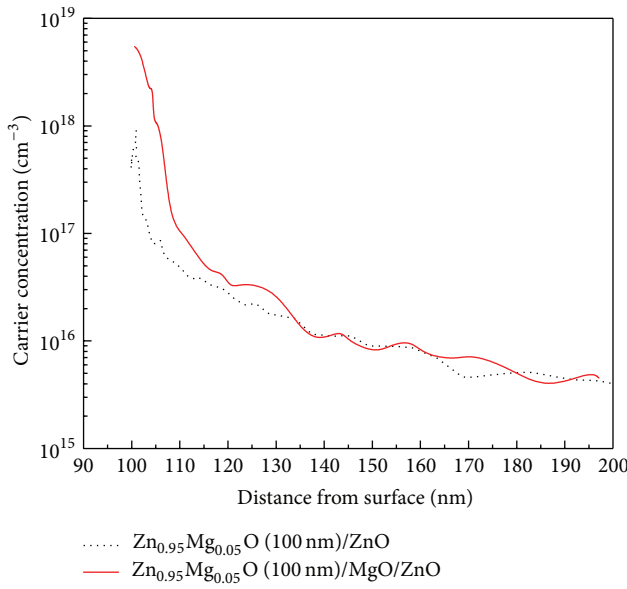


FIGURE 4: C-V depth profiling of the 2DEG and net donor concentration in the Zn_{0.95}Mg_{0.05}O/ZnO and Zn_{0.95}Mg_{0.05}O/MgO/ZnO structures.

C-V measurement. 2DEG of Zn_{0.95}Mg_{0.05}O/ZnO structure with 20 nm thick Zn_{0.95}Mg_{0.05}O layer was not observed by C-V. Owing to the low Mg content and thickness of ZnMgO barrier layer, the conduction band offset was small and the providing of electron was not enough to format 2DEG.

Table 1 shows the typical values of Hall mobility (μ) and 2DEG density (n) measured at 300 K and 10 K for ZnMgO/ZnO structures with or without MgO interfacial layers. From Table 1, it is clearly seen that the Hall mobility was increased by the insertion of MgO interfacial layers. In particular, the Zn_{0.95}Mg_{0.05}O (20 nm)/MgO/ZnO heterostructure showed very high Hall mobility of 332 cm²/Vs

TABLE 1: Typical Hall mobility (μ) and 2DEG density (n) measured at 300 K and 10 K for ZnMgO/ZnO structures with or without MgO interfacial layers.

Structure	ZnMgO thickness (nm)	n ($\times 10^{12}$ cm ⁻²)		μ (cm ² /Vs)	
		300 K	10 K	300 K	10 K
ZnMgO/MgO/ZnO	20	25	22	332	3090
ZnMgO/ZnO	20	1.5	0.2	137	130
ZnMgO/MgO/ZnO	100	2.2	1.9	321	2480
ZnMgO/ZnO	100	0.2	0.4	215	2360

at RT and 3090 cm²/Vs at 10 K. Figure 5 shows the results of temperature-dependent Hall measurements. The electron mobility of Zn_{0.95}Mg_{0.05}O (100 nm)/ZnO and Zn_{0.95}Mg_{0.05}O (100 nm and 20 nm)/MgO/ZnO structures increases with decreasing temperature, as shown in Figure 5(a). This trend is nearly identical to that reported for AlGaAs/GaAs [21–23], AlGaN/GaN [24, 25], and ZnMgO/ZnO heterostructure [5, 13], which is consistent with the existence of a 2DEG at the heterointerface. Compared with reported values for both Zn polar and O-polar ZnMg(Mn)O/ZnO heterostructures, the high mobility is obvious [11, 13, 26, 27]. The mobility of Zn_{0.95}Mg_{0.05}O (20 nm)/ZnO structure changed similarly to a single ZnO thin film as the temperature was changing, which indicates no 2DEG was formatted because of thin barrier layer. By the insertion of MgO layer, a 2DEG was observed. The results agree well with the results of C-V measurement. The high electron mobility of the ZnMgO/MgO/ZnO heterostructure was mainly attributed to the reduction of alloy disorder scattering. In Figure 5(b), the sheet carrier concentration of Zn_{0.95}Mg_{0.05}O (100 nm)/ZnO and Zn_{0.95}Mg_{0.05}O (100 nm and 20 nm)/MgO/ZnO structures changes little with increasing temperatures, indicating the good confinement of channel electrons. The insert of a thin (1 nm) MgO layer between ZnMgO and ZnO enhanced the sheet carrier concentration almost one order of magnitude. It also confirms the thin MgO enhanced the confinement effectively.

3.4. The Calculation and Experimental Results of the Dependence of Carrier Sheet Density of 2DEG on ZnMgO Layer Thickness. It is noted that the presence of strong polarization-induced fields in both MgO and ZnMgO cap layers leads to a very interesting dependence of the 2DEG sheet density in ZnMgO/MgO/ZnO structures on ZnMgO cap thickness. The density of 2DEG decreases with increasing ZnMgO thickness. To discuss the behavior of 2DEG density changing with the thickness of ZnMgO layer in ZnMgO/MgO/ZnO structures, simple electrostatic analysis of the Zn_{1-x}Mg_xO/MgO/ZnO heterostructures yields the following expression for the 2DEG sheet density [11, 15, 28–30]:

$$n_s = \frac{1}{1 + d_1/d_2} \left[\frac{+\sigma}{e} - \frac{\epsilon_0 \epsilon}{d_2} (e\phi_b + E_F - \Delta E_C) \right], \quad (1)$$

where the effect of Zn_{1-x}Mg_xO cap was approximately equal to a ZnO cap layer because of the low Mg composition and where d_1 (1 nm here) and d_2 are the thicknesses of the MgO and top Zn_{1-x}Mg_xO layer barrier layers, correspondingly,

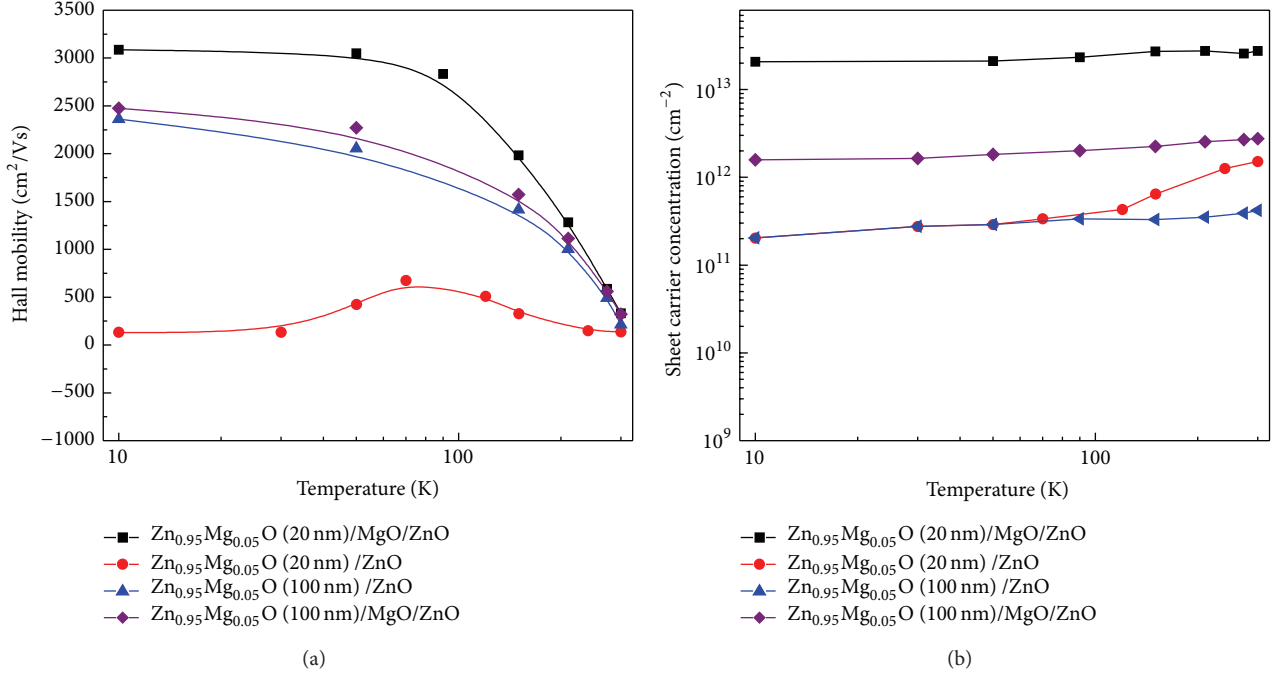


FIGURE 5: Temperature-dependent Hall measurements for Zn polar Zn_{0.95}Mg_{0.05}O/ZnO and Zn_{0.95}Mg_{0.05}O/MgO/ZnO structures, mobility (a) and carrier concentration (b).

as shown in Figure 1(b); the surface potential $e\phi_b$ is assumed to be pinned at surface with a level of 0.8 eV below ZnO conduction band edge. The conduction band offset ΔE_C is equal to $0.9 \times [E_g(\text{MgO}) - E_g(\text{ZnO})]$ [31]. We approximate the Fermi level \bar{E}_F by the infinite triangular quantum well [23], which can be expressed as

$$E_F = \left[\frac{9\pi\hbar^2}{(8\epsilon_0\sqrt{8m^*})} \frac{n_s}{\epsilon} \right]^{2/3} + \frac{\pi\hbar^2}{m^*n_s}, \quad (2)$$

where the dielectric constant ϵ is given as $(8.75 + 1.08 * 1)$ for the very thin wurtzite MgO [10]. The effective mass is taken to be $m^* \approx 0.26m_e$. σ is the polarization-induced charge density determined by the vector sum of the spontaneous polarization (P_{SP}) and the strain-induced piezoelectric polarization (P_{PE}) while there is no external field. We assume that the thin MgO layer is fully strained on ZnO and polarization constants vary linearly with x composition. Thus, the dependence of total polarizations-induced charges in MgO layer can be expressed as $\sigma = 0.029x$ (C/m²) ($x = 1$) [12]. Taking the tunneling of electrons from MgO/ZnO channel to Zn_{1-x}Mg_xO layer into account, we modified σ by a coefficient ν , and then it can be expressed as

$$\sigma = 0.029\nu \text{ (C/m}^2\text{)}, \quad (\nu = 0 \sim 1). \quad (3)$$

For $\nu = 0.1$, the calculated 2DEG density and experimental results were shown in Figure 6. The solid line is the calculated plot extracted from (1). The sheet carrier concentration decreases rapidly as the thickness of ZnMgO layer increases. The 2DEG density of the Zn_{0.95}Mg_{0.05}O/MgO/ZnO

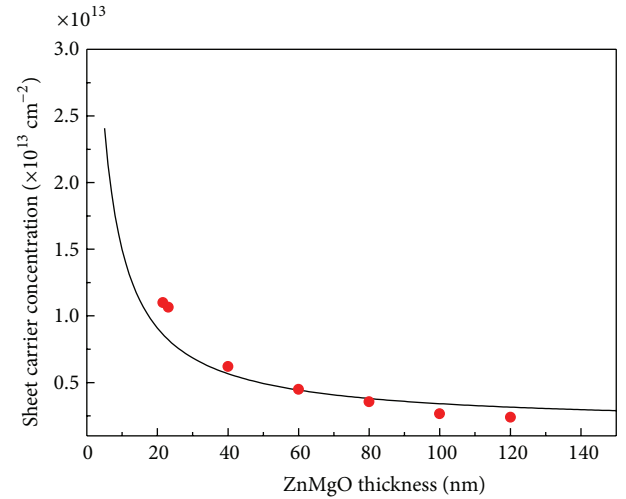


FIGURE 6: The dependence of sheet carrier concentration as a function of ZnMgO layer thickness.

structure with the layer thickness of 20 nm is $1.1 \times 10^{13} \text{ cm}^{-2}$, and it becomes $2.4 \times 10^{12} \text{ cm}^{-2}$ when the thickness is 120 nm. The theoretical prediction and experimental results agreed well below 80 nm, which confirmed the ZnMgO layers in ZnMgO/MgO/ZnO structure, to a certain extent, behaved similar to a ZnO cap layer. After the thickness became larger than 80, the 2DEG density became lower than the calculated line. That is because the stress of the ZnMgO strain layer increases as the thickness increases, which results in the

deterioration of crystal quality. There might be other reasons which need to be studied in the future.

We note that there is somewhat a discrepancy in the sheet carrier concentration values obtained by C - V and Hall measurement. Since the data observed from Hall measurement includes the contribution of bulk carrier, the value was higher than the true value.

4. Conclusion

In summary, formation of a 2DEG was confirmed for Zn polar ZnMgO/ZnO heterostructures with low Mg composition ($x = 0.05$). The enhancement of 2DEG concentration and mobility were realized in Zn_{1-x}Mg_xO/MgO/ZnO with low Mg composition by inserting of a thin (1 nm) MgO obviously. The sample shows a high Hall mobility of 3090 cm²/Vs at 10 K and 332 cm²/Vs at RT. The carrier concentration reached a value as high as 1.1×10^{13} cm⁻². However, the study for higher Mg content Zn_{1-x}Mg_xO/MgO/ZnO structures will be done in the future. The results demonstrate a well defined heterostructure and the possibility for fabrication of ZnMgO/MgO/ZnO HEMT devices.

Conflict of Interests

The authors declare that there is no conflict of interests regarding the publication of this paper.

Acknowledgments

This work was supported by Project 863 of Xi'an Jiaotong University (2013AA03A101) and National Natural Science Foundation of China (no. 60876042 and no. 61176018).

References

- [1] J. D. Albrecht, P. P. Ruden, S. Limpijumngong, W. R. L. Lambrecht, and K. F. Brennan, "High field electron transport properties of bulk ZnO," *Journal of Applied Physics*, vol. 86, no. 12, pp. 6864–6867, 1999.
- [2] A. Ohtomo, M. Kawasaki, T. Koida et al., "Mg_xZn_{1-x}O as a II-VI widegap semiconductor alloy," *Applied Physics Letters*, vol. 72, no. 19, pp. 2466–2468, 1998.
- [3] A. Ohtomo, M. Kawasaki, I. Ohkubo, H. Koinuma, T. Yasuda, and Y. Segawa, "Structure and optical properties of ZnO/Mg_{0.2}Zn_{0.8}O superlattices," *Applied Physics Letters*, vol. 75, no. 7, pp. 980–982, 1999.
- [4] H. Tampo, H. Shibata, K. Maejima et al., "Polarization-induced two-dimensional electron gases in ZnMgO/ZnO heterostructures," *Applied Physics Letters*, vol. 93, no. 20, Article ID 202104, 3 pages, 2008.
- [5] A. Tsukazaki, A. Ohtomo, M. Kawasaki et al., "Spin susceptibility and effective mass of two-dimensional electrons in Mg_xZn_{1-x}O/ZnO heterostructures," *Physical Review B*, vol. 78, no. 23, Article ID 233308, 2008.
- [6] S. Sasa, M. Ozaki, K. Koike, M. Yano, and M. Inoue, "High-performance ZnO/ZnMgO field-effect transistors using a heterometal-insulator-semiconductor structure," *Applied Physics Letters*, vol. 89, no. 5, Article ID 053502, 2006.
- [7] K. Koike, D. Takagi, M. Kawasaki et al., "Ion-sensitive characteristics of an electrolyte-solution-gate ZnO/ZnMgO heterojunction field-effect transistor as a biosensing transducer," *Japanese Journal of Applied Physics*, vol. 46, no. 36-40, pp. L865–L867, 2007.
- [8] K. Koike, D. Takagi, M. Hashimoto et al., "Characteristics of enzyme-based ZnO/Zn_{0.7}Mg_{0.3}O heterojunction field-effect transistor as glucose sensor," *Japanese Journal of Applied Physics*, vol. 48, no. 4, Article ID 04C081, 2009.
- [9] M. Nakano, A. Tsukazaki, A. Ohtomo et al., "Electronic-field control of two-dimensional electrons in polymer-gated-oxide semiconductor heterostructures," *Advanced Materials*, vol. 22, no. 8, pp. 876–879, 2010.
- [10] J. D. Ye, S. Pannirselvam, S. T. Lim et al., "Two-dimensional electron gas in Zn-polar ZnMgO/ZnO heterostructure grown by metal-organic vapor phase epitaxy," *Applied Physics Letters*, vol. 97, no. 11, Article ID 111908, 2010.
- [11] H.-A. Chin, I.-C. Cheng, C.-K. Li et al., "Electrical properties of modulation-doped rf-sputtered polycrystalline MgZnO/ZnO heterostructures," *Journal of Physics D: Applied Physics*, vol. 44, no. 45, Article ID 455101, 4 pages, 2011.
- [12] A. Tsukazaki, H. Yuji, S. Akasaka et al., "High electron mobility exceeding 10^4 cm² v⁻¹ s⁻¹ in Mg_xZn_{1-x}O/ZnO single heterostructures grown by molecular beam epitaxy," *Applied Physics Express*, vol. 1, no. 5, Article ID 055004, 2008.
- [13] H. Tampo, H. Shibata, K. Matsubara et al., "Two-dimensional electron gas in Zn polar ZnMgO/ZnO heterostructures grown by radical source molecular beam epitaxy," *Applied Physics Letters*, vol. 89, no. 13, Article ID 132113, 3 pages, 2006.
- [14] M. Miyoshi, T. Egawa, H. Ishikawa et al., "Nanostructural characterization and two-dimensional electron-gas properties in high-mobility AlGaN/AlN/GaN heterostructures grown on epitaxial AlN/sapphire templates," *Journal of Applied Physics*, vol. 98, no. 6, Article ID 063713, 5 pages, 2005.
- [15] I. P. Smorchkova, L. Chen, T. Mates et al., "AlN/GaN and (Al,Ga)N/AlN/GaN two-dimensional electron gas structures grown by plasma-assisted molecular-beam epitaxy," *Journal of Applied Physics*, vol. 90, no. 10, pp. 5196–5201, 2001.
- [16] L. Shen, S. Heikman, B. Moran et al., "AlGaN/AlN/GaN high-power microwave HEMT," *IEEE Electron Device Letters*, vol. 22, no. 10, pp. 457–459, 2001.
- [17] L. Hsu and W. Walukiewicz, "Effect of polarization fields on transport properties in AlGaN/GaN heterostructures," *Journal of Applied Physics*, vol. 89, no. 3, pp. 1783–1789, 2001.
- [18] Z. X. Mei, Y. Wang, X. L. Du et al., "Controlled growth of O-polar ZnO epitaxial film by oxygen radical preconditioning of sapphire substrate," *Journal of Applied Physics*, vol. 96, no. 12, pp. 7108–7111, 2004.
- [19] H. Tampo, H. Shibata, K. Maejima et al., "Strong excitonic transition of Zn_{1-x}Mg_xO alloy," *Applied Physics Letters*, vol. 91, no. 26, Article ID 261907, 3 pages, 2007.
- [20] J. S. Park, S. K. Hong, T. Minegishi et al., "Polarity control of ZnO films on (0001) Al₂O₃ by Cr-compound intermediate layers," *Applied Physics Letters*, vol. 90, no. 20, Article ID 201907, 3 pages, 2007.
- [21] R. Dingle, H. L. Störmer, A. C. Gossard, and W. Wiegmann, "Electron mobilities in modulation-doped semiconductor heterojunction superlattices," *Applied Physics Letters*, vol. 33, no. 7, pp. 665–667, 1978.

- [22] S. Hiyamizu, T. Mimura, T. Fujii, and K. Nanb, "High mobility of two-dimensional electrons at the GaAs/n-AlGaAs heterojunction interface," *Applied Physics Letters*, vol. 37, no. 9, pp. 805–807, 1980.
- [23] S. Hiyamizu and T. Mimura, "High mobility electrons in selectively doped GaAs/n-AlGaAs heterostructures grown by MBE and their application to high-speed devices," *Journal of Crystal Growth*, vol. 56, no. 2, pp. 455–463, 1982.
- [24] M. A. Khan, J. M. Van Hove, J. N. Kuznia, and D. T. Olson, "High electron mobility GaN/Al_xGa_{1-x}N heterostructures grown by low-pressure metalorganic chemical vapor deposition," *Applied Physics Letters*, vol. 58, no. 21, pp. 2408–2410, 1991.
- [25] M. A. Khan, J. N. Kuznia, J. M. Van Hove, N. Pan, and J. Carter, "Observation of a two-dimensional electron gas in low pressure metalorganic chemical vapor deposited GaN-Al_xGa_{1-x}N heterojunctions," *Applied Physics Letters*, vol. 60, no. 24, pp. 3027–3029, 1992.
- [26] T. Edahiro, N. Fujimura, and T. Ito, "Formation of two-dimensional electron gas and the magnetotransport behavior of ZnMnO/ZnO heterostructure," *Journal of Applied Physics*, vol. 93, no. 10, pp. 7673–7675, 2003.
- [27] K. Koike, K. Hama, I. Nakashima et al., "Piezoelectric carrier confinement by lattice mismatch at ZnO/Zn_{0.6}Mg_{0.4}O heterointerface," *Japanese Journal of Applied Physics*, vol. 43, no. 10, pp. L1372–L1375, 2004.
- [28] O. Ambacher, B. Foutz, J. Smart et al., "Two dimensional electron gases induced by spontaneous and piezoelectric polarization in undoped and doped AlGaIn/GaN heterostructures," *Journal of Applied Physics*, vol. 87, no. 1, pp. 334–344, 2000.
- [29] I. P. Smorchkova, C. R. Elsass, J. P. Ibbetson et al., "Polarization-induced charge and electron mobility in AlGaIn/GaN heterostructures grown by plasma-assisted molecular-beam epitaxy," *Journal of Applied Physics*, vol. 86, no. 8, pp. 4520–4526, 1999.
- [30] E. T. Yu, G. J. Sullivan, P. M. Asbeck, C. D. Wang, D. Qiao, and S. S. Lau, "Measurement of piezoelectrically induced charge in GaN/AlGaIn heterostructure field-effect transistors," *Applied Physics Letters*, vol. 71, no. 19, pp. 2794–2796, 1997.
- [31] M. Yano, *Zinc Oxide, Bulk, Thin Films and Nanostructures*, C. Jagadish and S. J. Pearton, Eds., Elsevier, Amsterdam, The Netherlands, 2006.

Research Article

Mobility Limitations due to Dislocations and Interface Roughness in AlGaN/AlN/GaN Heterostructure

Qun Li,¹ Jingwen Zhang,¹ Li Meng,¹ Jing Chong,² and Xun Hou¹

¹Key Laboratory for Physical Electronics and Devices of the Ministry of Education, Key Laboratory of Photonics Technology for Information of Shaanxi Province, and ISCAS-XJTU Joint Laboratory of Functional Materials and Devices for Informatics, School of Electronics and Information Engineering, Xi'an Jiaotong University, Xi'an 710049, China

²China Satellite Maritime Tracking and Control Department, Jiangyin 214431, China

Correspondence should be addressed to Jingwen Zhang; jwzhang@mail.xjtu.edu.cn

Received 12 March 2015; Revised 29 May 2015; Accepted 8 June 2015

Academic Editor: Meiyong Liao

Copyright © 2015 Qun Li et al. This is an open access article distributed under the Creative Commons Attribution License, which permits unrestricted use, distribution, and reproduction in any medium, provided the original work is properly cited.

The dislocations and surface roughness in an AlGaN/AlN/GaN heterostructure were analyzed by transmission electron microscopy (TEM) and atomic force microscopy (AFM), respectively, and the mobility limitation mechanisms in the two-dimensional electron gas (2DEG) were studied using a theoretical model that took into account the most important scattering mechanisms. An exponential correlation function provides a better description of the statistical properties of surface roughness than the Gaussian form and thus is adopted in the theoretical model. The calculated results are in good agreement with Hall data. The quantitative measurements of dislocations and surface roughness allow the evaluation of the relative importance of each extrinsic scattering mechanism.

1. Introduction

GaN-based materials have attracted a great deal of attention over the past two decades due to their direct and large band gap. A high sheet carrier density (over $1.0 \times 10^{13} \text{ cm}^{-2}$) and high mobility (over $6.0 \times 10^4 \text{ cm}^2/\text{Vs}$) two-dimensional electron gas (2DEG) can be formed in AlGaN/GaN heterostructures even without intentionally doping [1, 2], which forecasts the prospects for fabricating high-power, high-frequency microwave devices.

In an ideal, defect free material, the electron mobility is mainly limited by electron-phonon interactions. In a real heterostructure material, however, the extrinsic scattering mechanisms, such as dislocations, interface roughness, and charged impurities, may dominate the electron mobility, particularly at low temperatures.

Most GaN thin films are grown on *c*-plane sapphire substrates by metal-organic chemical vapor deposition (MOCVD). The larger lattice mismatch between the GaN layer and the sapphire substrate induces a large number of dislocations. Great efforts have been made to improve the crystal quality of GaN films by preparing a nucleation layer,

optimizing growth parameters, and so on, but GaN still has a dislocation density up to $10^8 \sim 10^{10} \text{ cm}^{-2}$ [3]. Although high-density dislocations do not significantly affect the efficiencies of GaN-based light-emitting diodes (LEDs) and laser diodes (LDs) [4], they may dominate the electron mobility in AlGaN/GaN heterostructures [5, 6].

Interface roughness is another important scattering mechanism that affects the electron mobility in AlGaN/GaN heterostructures. Interface roughness is difficult to be measured directly. Cross-sectional transmission electron microscopy (TEM) measurements can give a direct observation of spatial variation in interface structure, but this approach is not convenient to quantify the interface roughness. For the heterostructures grown in a two-dimensional (2D) growth mode, the interface roughness can be approximated by surface roughness and thus can be characterized by atomic force microscopy (AFM) measurements. The effect of interface roughness on electron mobility is also difficult to be precisely modeled due to the random variation of roughness height. In theoretical calculations, a correlation function has usually been adopted to describe the statistical properties of interface roughness for mathematical convenience [7, 8].

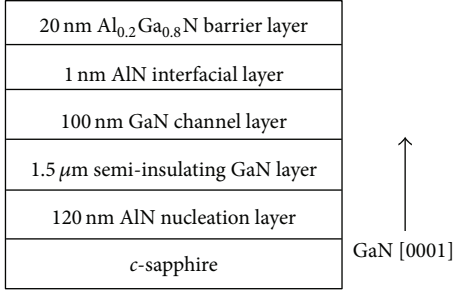


FIGURE 1: Schematic drawing of the Ga-polar AlGaIn/AlN/GaN heterostructure grown by MOCVD on *c*-sapphire substrate.

In addition to dislocations and interface roughness, charged residual impurities and alloy disorder may play important roles in the electron transport in a 2DEG system [9, 10]. In most theoretical studies regarding electron transport, the parameters describing extrinsic scattering mechanisms, such as dislocation density and impurity density, have been treated as adjustable fitting parameters [11, 12]; however, the relative importance of different extrinsic scattering mechanisms cannot be evaluated when the number of the fitting parameters is more than one. To evaluate their relative importance with regard to the mobility limitation, it is necessary first to quantify these parameters via direct measurements and then to calculate the mobility limited by individual scattering mechanisms.

In this work we prepared an AlGaIn/AlN/GaN heterostructure by MOCVD on *c*-sapphire and studied the mobility limitation mechanisms in the 2DEG. The TEM and AFM techniques are used to analyze the dislocations and surface roughness in the AlGaIn/AlN/GaN heterostructure, respectively. The measured results of dislocations and surface roughness are put into a theoretical model that takes into account the most important scattering mechanisms to fit the Hall data and to evaluate the relative importance of each extrinsic scattering mechanism.

2. Experimental Results

A Ga-polar AlGaIn/AlN/GaN heterostructure was grown by MOCVD on *c*-plane sapphire. As shown in Figure 1, the AlGaIn/AlN/GaN heterostructure consists of a 120 nm AlN nucleation layer, a 1.5 μm GaN semi-insulating layer, a 100 nm GaN channel layer, a 1 nm AlN interfacial layer, and a 20 nm Al_{0.2}Ga_{0.8}N barrier layer.

The cross-sectional and plan-view TEM measurements are performed on the heterostructure sample. In Figure 2(a) the dark-field cross-sectional TEM image shows the dislocation distribution. The high-density dislocations near the substrate appear to be arranged irregularly. These dislocations are generated at the early stage of the growth when the neighboring three-dimensional (3D) islands coalesce due to the Volmer-Weber growth mode. After the islands coalesce and dislocations form, the growth mode switches from a 3D growth to a 2D growth. The threading dislocations vertically traverse from the AlN nucleation layer to the AlGaIn barrier

layer, which is accompanied by a decrease in the dislocation density. The areal density of dislocations in the AlGaIn layer is estimated to be $1 \times 10^9 \text{ cm}^{-2}$ by counting dislocations from plan-view TEM images (see, e.g., Figure 2(b)). The high-resolution cross-sectional TEM image (Figure 2(c)) shows abrupt AlGaIn/AlN/GaN interfaces and a smooth AlGaIn surface, further indicating a 2D growth mode of the AlGaIn layer.

Dislocations can affect the 2DEG mobility in two ways: first, they induce local deformation of the crystal structure; secondly, the accumulated charges along the dislocation line can scatter electrons via Coulomb interactions. The effect of the local strain field on electron mobility is negligibly small compared with that of the Coulomb interactions [5]; therefore, only the Coulomb interactions are taken into account in the dislocation scattering in this study. Coulomb interactions are isotropic; thus, the calculations do not require determining the dislocation types.

Figure 3 shows a $3 \mu\text{m} \times 3 \mu\text{m}$ AFM image. The root-mean-square (RMS) surface roughness is 0.13 nm, indicating a smooth surface. The statistical properties of surface roughness can be described by a correlation function, which is defined as [8]

$$C(r) = \frac{1}{S} \int_S H(r') H(r'+r) dr', \quad (1)$$

where S is the sample area, r' is the position vector on the surface, r is the relative distance, and $H(r')$ is the surface height at position r' . The correlation function can be numerically calculated from the AFM measurement. But more often, two approximate analytical expressions, that is, for the Gaussian, $C(r) = \Delta^2 \exp(-r^2/\Lambda^2)$, and exponential, $C(r) = \Delta^2 \exp(-r/\Lambda)$, are employed in theoretical calculations for mathematical convenience. Once the analytical form of the correlation function has been fixed, the surface roughness can be described by two parameters, that is, the RMS roughness Δ and the horizontal correlation length Λ of surface heights. The Λ is usually defined as a distance at which the value of correlation function drops to $e^{-1} = 36.8\%$ of the value at $r = 0$ (here e is the Neper number).

The normalized correlation function calculated from the AFM data is shown in Figure 4. The correlation length Λ is determined to be 4.5 nm according to the definition above. In addition, the analytical Gaussian and exponential correlation functions with $\Lambda = 4.5 \text{ nm}$ are present in Figure 4 for comparison. It can be seen from Figure 4 that the exponential form more closely resemble the measured results than the Gaussian form. Therefore, the exponential correlation function is substituted for the measured one in the following scattering calculations.

Figure 5 shows the temperature-dependent Hall-effect measurements. The electron mobility monotonically increases with the decrease of the temperature and gradually saturates below 100 K. The sheet carrier density, $N_s = 1.05 \times 10^{13} \text{ cm}^{-2}$, is almost temperature independent, indicating that the contribution of bulk carriers is quite small. The Hall-effect measurements exhibit obvious characteristics of the 2DEG formation in the AlGaIn/AlN/GaN heterostructure.

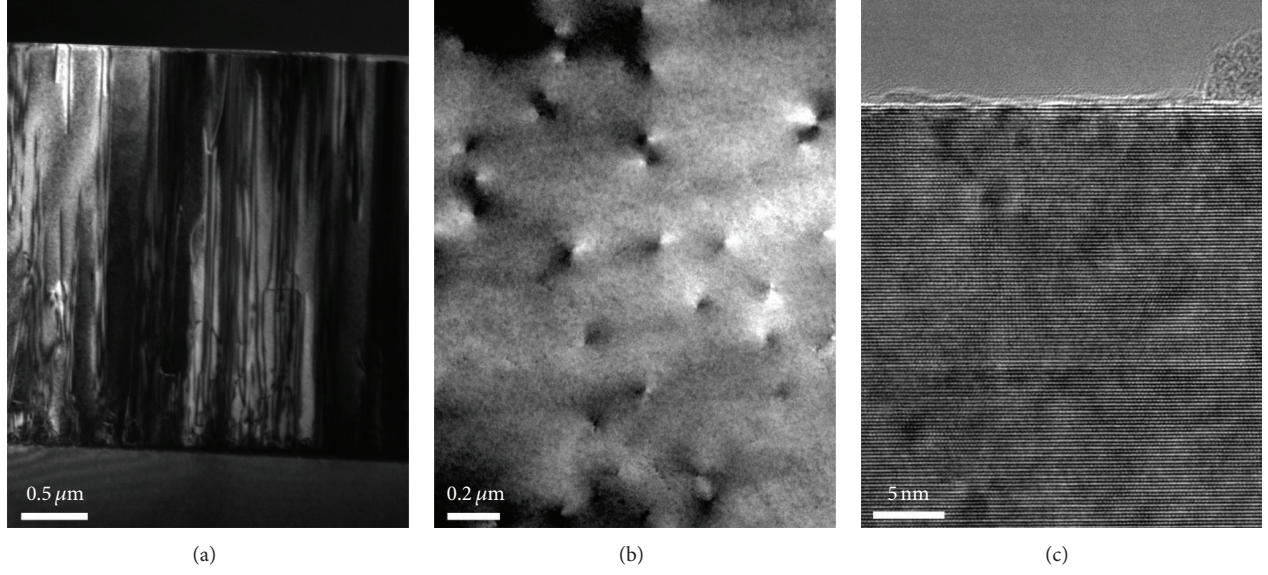


FIGURE 2: (a) Dark-field cross-sectional TEM image, (b) bright-field plan-view TEM image, and (c) high-resolution cross-sectional TEM image of the AlGaIn/AlN/GaN heterostructure.

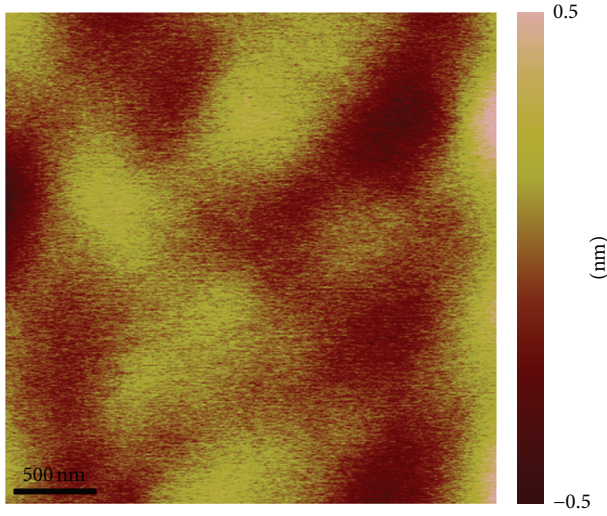


FIGURE 3: AFM image of the AlGaIn/AlN/GaN heterostructure with an RMS roughness of 0.13 nm.

3. Theoretical Descriptions

The scattering theories of the 2DEG system have been well developed by several authors [5, 13–19]. We give below a brief description of the analytical expressions for the momentum relaxation time $\tau_i(E)$ due to the important scattering mechanisms. The corresponding mobility component is calculated via $\mu_i = e\tau_i/m^*$; here e is the electronic charge, and m^* is the electron effective mass. The total mobility is calculated using Matthiessen's rule:

$$\frac{1}{\mu_{\text{TOT}}} = \sum_i \frac{1}{\mu_i}. \quad (2)$$

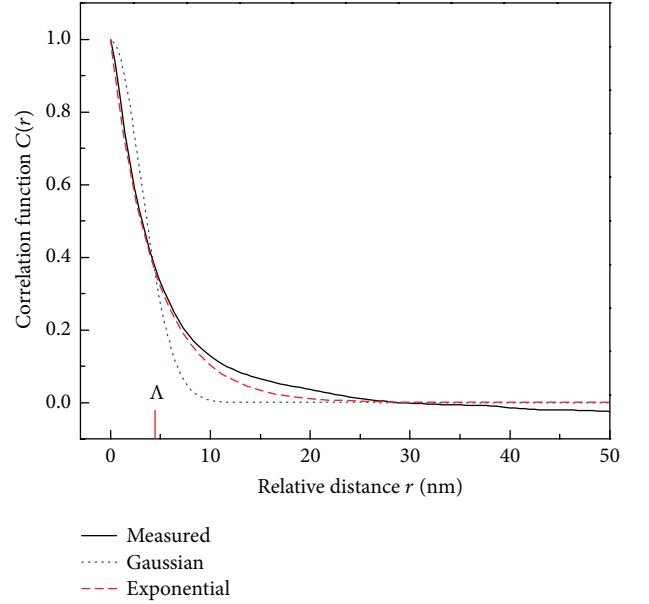


FIGURE 4: Normalized correlation function of surface roughness as a function of relative distance. The solid line is calculated from the AFM data, and the dashed and dotted lines represent the exponential and Gaussian correlation functions, respectively.

3.1. Dislocation Scattering (DIS). The matrix element for the Coulomb interactions of a single dislocation line is expressed as [20]

$$|M_{\text{DIS}}|^2 = \frac{e^2 \rho_l^2}{4S\epsilon_0^2 \epsilon_s^2 q^2} \left\{ \left[\int \exp(-q|z' - z|) dz' \right] \cdot |\xi(z)|^2 dz \right\}^2, \quad (3)$$

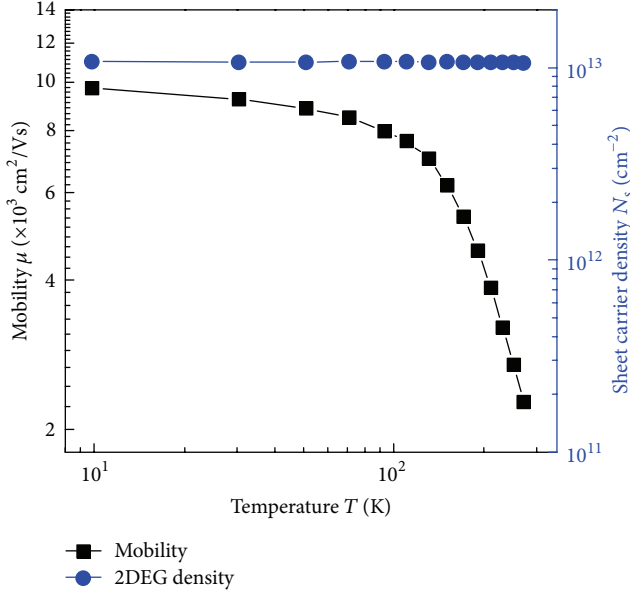


FIGURE 5: Mobility and sheet carrier density as a function of temperature for the AlGaIn/GaN heterostructure.

where q is the scattered wave vector, ϵ_0 is the permittivity of free space, ϵ_s is the static permittivity, $\rho_l = ef/c$ is the linear charge density along the dislocation line, f is the fraction of filled states, c is the lattice constant along the wurtzite GaN [0001] direction, and $\xi(z)$ is the electron wave function. Here we set $f = 1$; that is, there is one charge in every interval length of c along the dislocation line.

The reciprocal momentum relaxation time for the DIS is given by

$$\frac{1}{\tau_{\text{DIS}}(E)} = \frac{N_{\text{DIS}} m^* e^2 \rho_l^2}{4\pi \hbar^3 \epsilon_0^2 \epsilon_s^2} \cdot \int_0^\pi \left\{ \iint \left[\exp(-q|z' - z|) \right] |\xi(z)|^2 dz \right\}^2 \cdot \frac{(1 - \cos \theta)}{q^2 \epsilon^2(q)} d\theta, \quad (4)$$

where N_{DIS} is the dislocation density, \hbar is the reduced Planck's constant, and θ is the angle between electron wave vectors before and after scattering. The wave vector q is related to θ via $q = 2k \sin(\theta/2)$; k is the electron wave vector. $\epsilon(q)$ is the screening function within the zero-temperature random-phase approximation [16].

3.2. Interface Roughness Scattering (IRS). Interface roughness induces fluctuations in the position of the barrier layer, leading to perturbations of the electron energy and wave function in the well layer. The effect of interface roughness on electron mobility is more important in narrower wells [12].

For an exponentially correlated surface, the matrix element for the IRS can be expressed as

$$|M_{\text{IRS}}|^2 = \frac{e^4 \Delta^2 \Lambda^2 N_s^2}{2S \epsilon_0^2 \epsilon_s^2} (1 + q^2 \Lambda^2)^{-3/2}. \quad (5)$$

The reciprocal momentum relaxation time is given by

$$\frac{1}{\tau_{\text{IRS}}(E)} = \frac{e^4 m^* \Delta^2 \Lambda^2 N_s^2}{2\pi \hbar^3 \epsilon_0^2 \epsilon_s^2} \int_0^\pi (1 + q^2 \Lambda^2)^{-3/2} \frac{(1 - \cos \theta)}{\epsilon^2(q)} d\theta. \quad (6)$$

3.3. Charged Impurity Scattering (CIS). Most AlGaIn/GaN heterostructures have been prepared without doping, but residual impurities, such as carbon, hydrogen, interstitial atoms, and vacancies, cannot be completely eliminated [21]. The neutral impurity scattering is quite small and consequently is neglected in this work. However, the CIS may dominate the electron mobility at low temperatures. The matrix element for the CIS is expressed as [12]

$$|M_{\text{CIS}}|^2 = \frac{N(z)}{S} \left(\frac{e^2 F_c(q, z)}{2\epsilon_0 \epsilon_s q} \right)^2, \quad (7)$$

where $N(z)$ is the distribution function of charged impurities. $F_c(q, z)$ is given by [12]

$$F_c(q, z) = \int |\xi(z')|^2 \exp(-q|z - z'|) dz'. \quad (8)$$

Assuming that charged impurities are evenly distributed throughout the heterostructure at a density of N_{CIS} , the reciprocal momentum relaxation time is given by

$$\frac{1}{\tau_{\text{CIS}}(E)} = \frac{e^4 m^* N_{\text{CIS}}}{4\pi \hbar^3 \epsilon_0^2 \epsilon_s^2} \int_0^\pi \frac{|F_c(q, z)|^2 dz}{q^2 \epsilon^2(q)} (1 - \cos \theta) d\theta. \quad (9)$$

3.4. Phonon Scattering. Acoustic phonon scattering may dominate the electron mobility in the temperature range from several tens to two hundred of degrees Kelvin. Because wurtzite GaN is noncentrosymmetric, acoustic phonons can affect the electron mobility via deformation-potential (DP) and piezoelectric (PE) scatterings. In this study both DP and PE scatterings are taken into account. A detailed description of the acoustic phonon scattering can be found in [13, 15].

Polar optical (PO) phonon scattering dominates the electron mobility at high temperatures. The momentum relaxation time for PO phonon scattering is hardly strictly defined because the PO phonon scattering is inelastic and anisotropic. An accurate approach for studying PO phonon-limited mobility (μ_{PO}) is to directly solve the Boltzmann equation, but in that way one must carry out some really elaborate mathematical calculations. Here we use an approximate analytical expression to calculate μ_{PO} [16].

The physical parameters used in the calculations are listed in Table 1.

TABLE 1: Parameters of ZnO employed in calculations. Here m_0 is the free electron mass.

Parameter	Symbol (units)	Value
Mass density	ρ (kg/m ³)	6.15×10^3 ^a
Electron effective mass	m^*	$0.22 m_0$ ^b
Dielectric constant (high frequency)	ϵ_∞	5.47 ^b
Dielectric constant (low frequency)	ϵ_s	10.4 ^b
LA-phonon velocity	u_l (m/s)	6.56×10^3 ^a
LO-phonon energy	$\hbar\omega_{\text{PO}}$ (meV)	91.2 ^b
Piezoelectric tensor	e_{15} (C/m ²)	-0.3 ^c
	e_{31} (C/m ²)	-0.33 ^c
	e_{33} (C/m ²)	0.65 ^c
Deformation constant	D (eV)	8.5 ^b

^a[16], ^b[20], ^c[22].

4. Fittings

For AlGaIn/AlN/GaN heterostructures, the AlN interfacial layer produces a potential barrier of height 2.1 eV at the AlN/GaN interface [23], effectively preventing electron penetration into the AlGaIn layer. Therefore, the wave function, $\xi(z) = (b^3/2)^{1/2} z \exp(-bz/2)$, proposed by Fang and Howard [24], is still a good approximation to the electron distribution along the growth direction for AlGaIn/AlN/GaN heterostructures and consequently is employed in the scattering calculations. For the same reason alloy scattering is neglected in this study.

For the 2DEG in our heterostructure sample, the Fermi energy $E_F = \hbar k_F^2/2m^* \gg 2k_B T$ over the entire temperature range up to 300 K, where $k_F = \sqrt{2\pi N_s}$ is the Fermi wave vector; thus, the 2DEG is highly degenerate even at room temperature [25]. In the fitting to the experimental data, therefore, it is justified to perform scattering calculations only at the Fermi energy.

Figure 6 shows a comparison between the theoretical and experimental results. The theoretical calculations are in good agreement with the experimental data. The measured values of the dislocation density and interface roughness, that is, $N_{\text{DIS}} = 1 \times 10^9 \text{ cm}^{-2}$, $\Delta = 0.13 \text{ nm}$, and $\Lambda = 4.5 \text{ nm}$, are used in the fittings. Charged impurities are assumed to be evenly distributed throughout the heterostructure at a density of N_{CIS} . In the fittings only the N_{CIS} is treated as an adjustable parameter and is determined to be $N_{\text{CIS}} = 6 \times 10^{17} \text{ cm}^{-3}$. A comparable unintentional doping level is frequently found in the literatures [16, 26]; thus, the fitting value of the charged impurity density is easy to reach experimentally and is acceptable.

The direct measurements of the defect parameters allow the evaluation of the relative importance of the extrinsic scattering mechanisms. It can be seen from Figure 6 that the CIS imposes the most severe limitation on low- and moderate-temperature mobilities, followed by the DIS and IRS. The mobilities limited by acoustic DP and PE scatterings are inversely proportional to the temperature. Acoustic scattering is relatively less important for the AlGaIn/AlN/GaN sample, but this scattering mechanism will play a more important

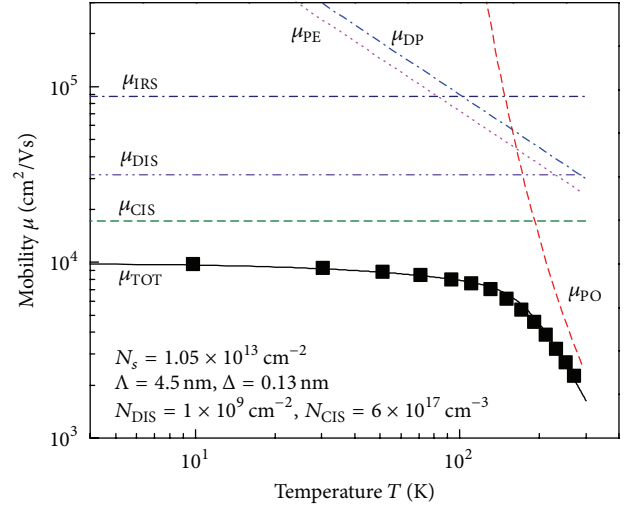


FIGURE 6: Temperature dependence of the mobility limited by individual scattering mechanisms including dislocation scattering (μ_{DIS}), interface roughness scattering (μ_{IRS}), charged impurity scattering (μ_{CIS}), acoustic DP scattering (μ_{DP}), acoustic PE scattering (μ_{PE}), PO phonon scattering (μ_{PO}), and all mentioned scattering mechanisms (μ_{TOT}). The scattered symbols are the experimental data.

role in the heterostructures with perfect crystal quality. The mobility limited by PO phonons decreases exponentially with increasing temperature, and this scattering mechanism is dominant at temperatures above 200 K.

Because the charged impurities dominate the electron transport at low and moderate temperatures, the calculation accuracies of DIS and IRS are more readily affected by measurement and model inaccuracies. But because of the larger distinction between the extrinsic scattering mechanisms, their relative importance would not be influenced by the inaccuracies.

5. Conclusions

In this study, we analyzed the dislocations and interface roughness in an AlGaIn/AlN/GaN heterostructure via direct measurements and explained the temperature dependence of the Hall mobility using a theoretical model. The dislocation density is estimated to be $1 \times 10^9 \text{ cm}^{-2}$ by TEM. The correlation length Λ and roughness height Δ are, respectively, determined to be 4.5 and 0.13 nm by AFM. The exponential correlation function, $C(r) = \Delta^2 \exp(-r/\Lambda)$, gives a better description of the statistical properties of surface roughness than the Gaussian form and thus is employed in the theoretical model. The theoretical calculations are in good agreement with the experimental data. The quantitative measurements of the dislocation density and interface roughness allow the evaluation of the relative importance of each extrinsic scattering mechanism. It is found that the CIS is the most important scattering mechanism at low and moderate temperatures, followed by the DIS and IRS, whereas the PO phonon scattering is dominant above 200 K.

Conflict of Interests

The authors declare that there is no conflict of interests regarding the publication of this paper.

Acknowledgments

The authors would like to thank Chuansheng Ma of International Center for Dielectric Research for TEM measurements. This work was supported by the National Natural Science Foundation of China under Grant nos. 61176018 and 60876042 and the National High Technology Research and Development Program of China (863 Program) under Grant no. 2013AA03A101.

References

- [1] M. Higashiwaki, S. Chowdhury, M.-S. Miao, B. L. Swenson, C. G. Van de Walle, and U. K. Mishra, "Distribution of donor states on etched surface of AlGa_xN/GaN heterostructures," *Journal of Applied Physics*, vol. 108, no. 6, Article ID 063719, 2010.
- [2] E. Frayssinet, W. Knap, P. Lorenzini et al., "High electron mobility in AlGa_xN/GaN heterostructures grown on bulk GaN substrates," *Applied Physics Letters*, vol. 77, no. 16, pp. 2551–2553, 2000.
- [3] V. P. Kladko, A. F. Kolomys, M. V. Slobodian et al., "Internal strains and crystal structure of the layers in AlGa_xN/GaN heterostructures grown on a sapphire substrate," *Journal of Applied Physics*, vol. 105, no. 6, Article ID 063515, 2009.
- [4] D. C. Look and J. R. Sizelove, "Dislocation scattering in GaN," *Physical Review Letters*, vol. 82, no. 6, pp. 1237–1240, 1999.
- [5] F. Carosella and J.-L. Farvacque, "Effect of threading dislocations on carrier mobility in AlGa_xN/GaN quantum wells," *Journal of Physics Condensed Matter*, vol. 20, no. 32, Article ID 325210, 2008.
- [6] X. Xu, X. Liu, X. Han et al., "Dislocation scattering in Al_xGa_{1-x}N/GaN heterostructures," *Applied Physics Letters*, vol. 93, no. 18, Article ID 182111, 2008.
- [7] S. M. Goodnick, D. K. Ferry, C. W. Wilmsen, Z. Liliental, D. Fathy, and O. L. Krivanek, "Surface roughness at the Si(100)-SiO₂ interface," *Physical Review B*, vol. 32, no. 12, pp. 8171–8189, 1985.
- [8] G. Fishman and D. Calecki, "Influence of surface roughness on the conductivity of metallic and semiconducting quasi-two-dimensional structures," *Physical Review B*, vol. 43, no. 14, pp. 11581–11585, 1991.
- [9] L. Hsu and W. Walukiewicz, "Electron mobility in Al_xGa_{1-x}N/GaN heterostructures," *Physical Review B*, vol. 56, no. 3, pp. 1520–1528, 1997.
- [10] A. Gold, "Theory of transport properties of the sixfold-degenerate two-dimensional electron gas at the H-Si(111) surface," *Physical Review B*, vol. 82, no. 19, Article ID 195329, 2010.
- [11] D. Zanato, S. Gokden, N. Balkan, B. K. Ridley, and W. J. Schaff, "The effect of interface-roughness and dislocation scattering on low temperature mobility of 2D electron gas in GaN/AlGa_xN," *Semiconductor Science and Technology*, vol. 19, no. 3, pp. 427–432, 2004.
- [12] J. M. Li, J. J. Wu, X. X. Han et al., "A model for scattering due to interface roughness in finite quantum wells," *Semiconductor Science and Technology*, vol. 20, no. 12, pp. 1207–1213, 2005.
- [13] T. Kawamura and S. Das Sarma, "Phonon-scattering-limited electron mobilities in Al_xGa_{1-x}As/GaAs heterojunctions," *Physical Review B*, vol. 45, no. 7, pp. 3612–3627, 1992.
- [14] T. Ando, A. B. Fowler, and F. Stern, "Electronic properties of two-dimensional systems," *Reviews of Modern Physics*, vol. 54, no. 2, pp. 437–672, 1982.
- [15] P. J. Price, "Two-dimensional electron transport in semiconductor layers. I. Phonon scattering," *Annals of Physics*, vol. 133, no. 2, pp. 217–239, 1981.
- [16] S. B. Lisesivdin, A. Yildiz, N. Balkan, M. Kasap, S. Ozelcik, and E. Ozbay, "Scattering analysis of two-dimensional electrons in AlGa_xN/GaN with bulk related parameters extracted by simple parallel conduction extraction method," *Journal of Applied Physics*, vol. 108, no. 1, Article ID 013712, 2010.
- [17] D. N. Quang, N. H. Tung, V. N. Tuoc, N. V. Minh, H. A. Huy, and D. T. Hien, "Quantum and transport lifetimes due to roughness-induced scattering of a two-dimensional electron gas in wurtzite group-III-nitride heterostructures," *Physical Review B*, vol. 74, no. 20, Article ID 205312, 2006.
- [18] A. Asgari, S. Babanejad, and L. Faraone, "Electron mobility, Hall scattering factor, and sheet conductivity in AlGa_xN/AlN/GaN heterostructures," *Journal of Applied Physics*, vol. 110, no. 11, Article ID 113713, 2011.
- [19] H. Tokuda, J. Yamazaki, and M. Kuzuhara, "High temperature electron transport properties in AlGa_xN/GaN heterostructures," *Journal of Applied Physics*, vol. 108, no. 10, Article ID 104509, 2010.
- [20] M. N. Gurusinghe, S. K. Davidsson, and T. G. Andersson, "Two-dimensional electron mobility limitation mechanisms in Al_xGa_{1-x}N/GaN heterostructures," *Physical Review B*, vol. 72, no. 4, Article ID 045316, 2005.
- [21] A. Ishibashi, H. Takeishi, M. Mannoh, Y. Yabuuchi, and Y. Ban, "Residual impurities in GaN/Al₂O₃ grown by metalorganic vapor phase epitaxy," *Journal of Electronic Materials*, vol. 25, no. 5, pp. 799–803, 1996.
- [22] A. D. Bykhovski, B. L. Gelmont, and M. S. Shur, "Elastic strain relaxation and piezoeffect in GaN-AlN, GaN-AlGa_xN and GaN-InGa_xN superlattices," *Journal of Applied Physics*, vol. 81, no. 9, pp. 6332–6338, 1997.
- [23] A. Janotti and C. G. van de Walle, "Absolute deformation potentials and band alignment of wurtzite ZnO, MgO, and CdO," *Physical Review B*, vol. 75, no. 12, Article ID 121201, 2007.
- [24] F. F. Fang and W. E. Howard, "Negative field-effect mobility on (100) Si surfaces," *Physical Review Letters*, vol. 16, no. 18, pp. 797–799, 1966.
- [25] R. Grill and G. H. Döhler, "Effect of charged donor correlation and Wigner liquid formation on the transport properties of a two-dimensional electron gas in modulation δ -doped heterojunctions," *Physical Review B*, vol. 59, no. 16, pp. 10769–10777, 1999.
- [26] T. Zhu and R. A. Oliver, "Unintentional doping in GaN," *Physical Chemistry Chemical Physics*, vol. 14, no. 27, pp. 9558–9573, 2012.

Research Article

Gallium Nitride Electrical Characteristics Extraction and Uniformity Sorting

Shyr-Long Jeng,¹ Chih-Chiang Wu,² and Wei-Hua Chieng²

¹Department of Electrical and Electronic Engineering, Ta Hua University of Science and Technology,
No. 1, Dahua Road, Qionglin Shiang, Hsinchu County 30740, Taiwan

²Department of Mechanical Engineering, National Chiao Tung University, No. 1001, University Road, Hsinchu City 30010, Taiwan

Correspondence should be addressed to Chih-Chiang Wu; wuchihchiang0517@gmail.com

Received 6 March 2015; Accepted 16 April 2015

Academic Editor: Meiyong Liao

Copyright © 2015 Shyr-Long Jeng et al. This is an open access article distributed under the Creative Commons Attribution License, which permits unrestricted use, distribution, and reproduction in any medium, provided the original work is properly cited.

This study examined the output electrical characteristics—current-voltage (I - V) output, threshold voltage, and parasitic capacitance—of novel gallium nitride (GaN) power transistors. Experimental measurements revealed that both enhanced- and depletion-mode GaN field-effect transistors (FETs) containing different components of identical specifications yielded varied turn-off impedance; hence, the FET quality was inconsistent. Establishing standardized electrical measurements can provide necessary information for designers, and measuring transistor electrical characteristics establishes its equivalent-circuit model for circuit simulations. Moreover, high power output requires multiple parallel power transistors, and sorting the difference between similar electrical characteristics is critical in a power system. An isolated gate driver detection method is proposed for sorting the uniformity from the option of the turn-off characteristic. In addition, an equivalent-circuit model for GaN FETs is established on the basis of the measured electrical characteristics and verified experimentally.

1. Introduction

Metal-oxide-semiconductor field-effect transistors (MOSFETs) have been widely used over the past 30 years. As silicon approaches its performance limits, wide-bandgap semiconductors, such as gallium nitride (GaN) and silicon carbide (SiC), are emerging technologies that can supersede silicon MOSFETs as next-generation power transistors. Novel wide-band III-nitride semiconductor materials are being rapidly developed because of their unique properties, such as high electron mobility, saturation velocity, sheet carrier concentration at heterojunction interfaces, and breakdown voltages [1, 2]. These properties make III-nitrides feasible for high-power, high-temperature applications. Compared with SiC, GaN has low turn-on and switching losses and is less expensive. In addition, GaN wafers are produced by numerous manufacturers, thus negating any monopoly concerns. Furthermore, GaN has been widely used in light-emitting diodes and wireless applications. GaN power FETs are

suitable for high-voltage, high-current, and motor-control applications as well as for industrial automation systems and automotive electronics [3–5].

Because both the commercially enhanced-mode (E-mode) and depletion-mode (D-mode) GaN FETs manufactured by National Chiao Tung University (NCTU) [6, 7] are relatively new types of power transistors, few related studies are available in the literature. In addition, few manufacturers discuss them because commercial applications are not yet prevalent. The electrical characteristics of commercially manufactured power transistors differ because of the differences in cutting, wiring, wire bonding materials and diameters, and packaging. Before using such power transistors in circuit applications, their electrical characteristics must be extracted and sorted to match similar electrical properties in circuit designs. Unfortunately, extracting similar electrical properties is time-consuming and expensive. Thus, rapid and easy extraction of the electrical characteristics of GaN FETs to sort similar electrical properties is essential.

Moreover, GaN FETs and the design of their gate drivers are relatively new. When using GaN FET power transistors in circuit applications, their unique electrical properties must be considered: (1) no intrinsic body diode [8–10], (2) low gate-to-source voltage limits [9, 10], (3) full-conduction voltage of the gate and uncommon power supply voltage (e.g., 7 V, 8 V) [11–13], and (4) low threshold voltage [9, 10, 12, 13]. The following properties are applicable to bridge-leg architecture power transistors: (1) floating source of the high-side power switch [14, 15] and (2) faulty turn-on [9, 15]. Therefore, GaN-FET-based power transistors require appropriate gate drive circuits and methods to prevent overload. Although numerous studies have examined these properties, none have focused on the turn-off characteristic.

This paper first reports the output electrical characteristics of novel GaN power transistors and standardized electrical measurements to provide necessary information for designers. Second, an isolated gate driver detection method is proposed for sorting. Finally, this paper presents a simple and accurate equivalent-circuit model of GaN FETs for circuit simulations, established on the basis of the measured electrical characteristics and verified experimentally.

2. Materials and Methods

2.1. Measurement of GaN Electrical Characteristics. On the basis of MOSFET and GaN-FET datasheets, the following characteristics were used in this study: (1) breakdown voltage 200 V, rated current 9 A, on-resistance 0.4 Ω , and E-mode MOSFET [16]; (2) breakdown voltage 500 V, rated current 6 A, on-resistance 0.5 Ω , and D-mode MOSFET [17]; (3) breakdown voltage 200 V, rated current 12 A, on-resistance 25 m Ω , and E-mode GaN FET [18]; and (4) D-mode GaN FET manufactured in the laboratory as testing devices. The electrical characteristics measured were I_D - V_D characteristics, threshold voltage, and parasitic capacitance.

2.1.1. I_D - V_D Characteristic Curve. I_D - V_D curve measurements detect the maximum output current of the power transistor when the gate voltage V_{GS} is applied as the full-conduction voltage, and the full-conduction on-state resistance is applied between the drain and source ($R_{DS(ON)}$). The characteristic curve reveals the linear and saturation regions of the circuit, where the device can operate properly. According to the test circuit in [19], the output characteristics are drain current I_D versus drain-source voltage V_{DS} measured under different gate voltages V_{GS} ranging from the gate turn-off to full-on voltage at intervals of 1 V. The V_{GS} range of the E- and D-mode MOSFET is 0 to 12 V and -12 to 0 V, respectively, the V_{GS} range of the E-mode GaN FET is 0 to 5 V, and that of the D-mode GaN FET manufactured by NCTU is -5 to 0 V. Drain voltage generally uses a pulse mode input, which prevents excessive heat that affects the output characteristics. According to the datasheets, test pulse properties for E- and D-mode MOSFETs and E-mode GaN-FETs are a pulse width of 300 μ s and a duty cycle (duty) $\leq 2\%$ [16–18]. In this study, a test pulse width of 300 μ s, pulse period of 300 ms, and duty cycle of 0.1% were used to measure the I_D - V_D curve characteristics of the four aforementioned power transistors.

2.1.2. Threshold Voltage. Threshold voltage (V_{TH}) is the minimum gate bias required to turn the device on and produce a drain current specified in the datasheet. In the threshold voltage measurement circuit for E-mode power transistors, the drain and gate terminals of the power transistors are shorted ($V_{DS} = V_{GS}$) [16]. The voltage to the gate terminal is gradually increased from the turn-off voltage V_{off} (0 V) until the measured current equals the specified drain current. For D-mode power transistors, the drain terminal is connected to a fixed DC voltage source. Similar to the test procedure for E-mode transistors, the voltage to the gate terminal of the D-mode transistor is gradually increased from V_{off} (-5 V) and changes in its drain current I_D are observed. As specified in the datasheet [17], a DC voltage of 25 V is applied to the drain terminal of D-mode MOSFETs. D-mode GaN FETs, which applying to drain terminal's DC voltage value refer to I_D - V_D characteristic curve while the drain voltage attains the saturation region under the power transistor, are fully opened ($V_{GS} = 0$ V). In this study, laboratory-manufactured D-mode GaN FET saturation voltage was set to the voltage measured from the I_D - V_D characteristic curve. The conduction threshold current of E- and D-mode MOSFET is 250 μ A [16, 17] and that of E-mode GaN-FET is 3 mA [18]. The laboratory-manufactured D-mode GaN FET has no datasheet for referencing its conduction threshold current. Therefore, to obtain the gate terminal input voltage V_{GS} at which the drain current I_D increases instantaneously, the experimental measurements of the drain current I_D are transformed logarithmically [20]. The V_{GS} thus obtained is considered the threshold voltage V_{TH} .

2.1.3. Parasitic Capacitance. A power device analyzer/curve tracer [21] was used to measure the capacitance because it supports the measurement of the three nonlinear capacitances: C_{GD} , C_{DS} , and C_{GS} . Figure 1 depicts the C_{GD} , C_{DS} , and C_{GS} measurement circuits, respectively. A multiple frequency capacitance measurement unit with four ports (Hp, Hc, Lp, and Lc) was used for capacitance measurements. Hp and Hc were shorted together (hereafter, CMH), and Lp and Lc were shorted together (hereafter, CML). The CMH outputs an AC test signal through the circuit under test, which is detected by the CML. The CMH operates in the 100 kHz–1 MHz AC frequency range. As specified in the MOSFET and E-mode GaN-FET datasheets, C_{GS} is measured at 100 kHz, and C_{DS} and C_{GS} are measured at 1 MHz; the oscillation level is 30 mV for all measurements. The CML receiving port potential is equivalent to the ground terminal.

The parasitic capacitance C_{GD} is measured using the circuit shown in Figure 1(a). The AC test signal is output from the CMH to the drain terminal, the source terminal is connected to a high-voltage source/monitor unit (HVSMU), and the source terminal grounds the AC signal to the AC guard. Therefore, the AC test signal from C_{DS} to the source terminal is grounded by the AC guard, preventing the signals from being received by the source terminal through the C_{GS} path. When measuring the parasitic capacitance C_{GD} , the HVSMU should provide a V_{off} DC bias relative to the CML gate terminal, and the power transistor should be kept off. Both the enhanced MOSFET and E-mode GaN-FET power

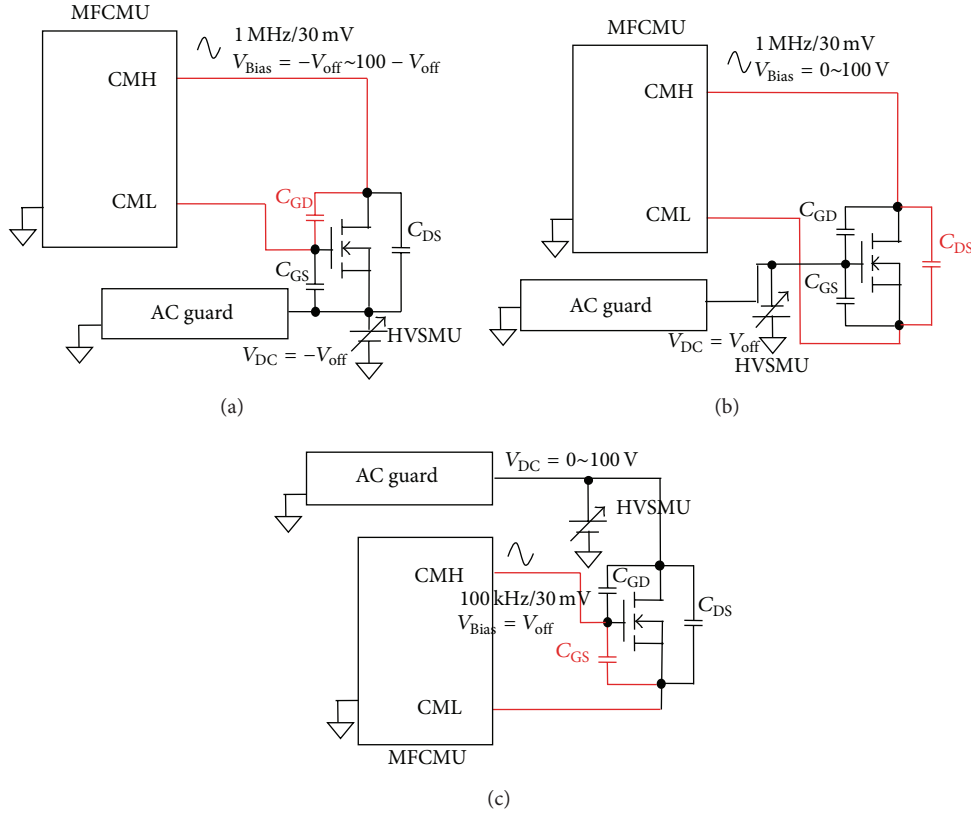


FIGURE 1: Test circuit for (a) C_{GD} capacitance, (b) C_{DS} capacitance, and (c) C_{GS} capacitance.

transistor have the same V_{off} (0 V), whereas that of the D-mode MOSFET power transistor is -12 V. However, the I_D - V_D curve revealed that the tested D-mode MOSFET turns off at -5 V. Therefore, in this study, -5 V was used as the V_{off} for the D-mode MOSFET power transistor. The V_{off} of D-mode GaN FET is -5 V. Because the source terminal has a bias voltage, $-V_{off}$, the CMH should apply an AC bias voltage in the range V_{off} to $100 - V_{off}$ to drain the terminal. Therefore, the bias V_{DS} voltage of measurement can range from 0 to 100 V.

The parasitic capacitance C_{DS} is measured using the circuit shown in Figure 1(b). The circuit is similar to that used to measure C_{GD} ; the only difference is that the gate terminal was changed to the source terminal to connect the CML. The CMH outputs an AC test signal to the drain terminal and receives an AC test signal from the CML by connecting CML to the source of the device under test. The gate terminal grounds the AC guard to prevent the AC test signals from being received by the source terminal through the C_{GD} and C_{GS} paths. To ensure that the power transistor remains off during the measurement, the DC voltage V_{off} is applied to the gate terminal. The CMH gradually increases the AC bias voltage from 0 to 100 V; therefore, the parasitic capacitance measurement C_{DS} is in the V_{DS} voltage range of 0–100 V.

The parasitic capacitance C_{GS} is measured using the circuit shown in Figure 1(c). The CMH outputs an AC test signal to the gate terminal, and the CML receives the signal by connecting to the source terminal. Because the CMH has

a V_{off} bias, the power transistor is kept off. To prevent the signals from being received by the source terminal through the C_{GD} and C_{DS} paths, the drain terminal is grounded to the AC guard. The HVSMU provides DC voltage in the range of 0–100 V; therefore, parasitic capacitance C_{GS} is measured at different V_{DS} voltages in the range of 0–100 V.

2.2. Mechanism of Isolated Gate Drive Detection

2.2.1. Conventional Gate Drive.

Conventional power transistor gate drives use gate drive integrated circuit (IC) architecture. When used in half- and full-bridge-leg drive topologies, gate drives typically use an optical coupling IC to form an isolated floating-supply gate drive circuit architecture. Isolated gate drive circuit architecture consists of fast optical coupling IC, gate driver IC, and auxiliary supply voltage, as shown in Figure 2. The gate drive voltage for the E-mode GaN FET gate-to-source voltage is $V_{ISO} - G_{ISO}$, and the V_{GS} for D-mode GaN FET gate drive voltage is $-V_{ISO}$ to G_{ISO} . The difference between the gate drive circuits for E- and D-mode GaN FETs is that the input supply voltages for the isolated gate driver amplifier are $(+V_{ISO}) - (G_{ISO})$ and $(G_{ISO}) - (-V_{ISO})$, respectively. The external gate drive signals of the isolated gate drive circuit for the E-mode GaN FET is $[0$ to $+V_{ISO}]$ relative to the ground (Gnd). Through the fast optical coupling IC, the signal is isolated and converted to $[0$ to $+V_{ISO}]$ relative to G_{ISO} . Finally, the isolated signal is amplified through the gate

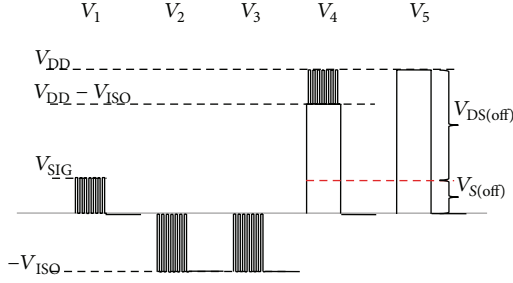


FIGURE 4: Detection drive signal for D-mode transistor.

to evaluate the turn-off capacity of the GaN FET. In this test, with a known probe resistance value R_L and by applying the Kirchhoff laws, the current through the power supply voltage V_{DD} at resistances $R_{DS(off)}$ and R_L is obtained as the leakage current I_{DSS} , which can be described as follows:

$$I_{DSS} = \frac{V_{DD}}{R_{DS(off)} + R_L}. \quad (1a)$$

The leakage current I_{DSS} flows through the voltage probe and produces $V_{S(off)}$ as follows:

$$V_{S(off)} = R_L I_{DSS}. \quad (1b)$$

By substituting (1a) into (1b), the $R_{DS(off)}$ impedance can be derived as follows:

$$R_{DS(off)} = R_L \frac{V_{DD}}{V_{S(off)}} - R_L. \quad (2)$$

A simplified simulation of the isolated gate drive detection circuit is shown in Figure 5(b). The simplified simulation circuit consists of the controlled signal source, E- or D-mode GaN FET current source, the isolated power supply ground G_{ISO} , ground Gnd, the parasitic capacitances C_{GS} , C_{GD} , and C_{DS} , turn-off impedance $R_{DS(off)}$, and voltage probe resistance R_L . The turn-off resistance $R_{DS(off)}$ and voltage probe resistance R_L connect together and, with the applied voltage V_{DD} and ground Gnd, form a loop that can use the Kirchhoff voltage law to estimate the leakage current I_{DSS} . The I_{DS} current source is extracted from the I_D - V_D characteristics. The I_D - V_D characteristic curve of the GaN FET follows the Level 1 MOSFET model characterized by (3a), (3b), and (3c) and is divided into cut-off (3a), linear (3b), and saturation (3c) regions.

Cut-off region:

$$I_{DS} = 0. \quad (3a)$$

Linear region:

$$I_{DS} = K_P \times \left[(V_{GS} - V_{TH}) \times V_{DS} - \frac{1}{2} V_{DS}^2 \right]. \quad (3b)$$

Saturation region:

$$I_{DS} = \frac{1}{2} \times K_P \times (V_{GS} - V_{TH})^2 \times (1 + \lambda \times V_{DS}), \quad (3c)$$

where K_P is the transduced value and λ is the short-channel width-modulation slope coefficient in the saturated region, which is initially set to 0. The sign of V_{TH} determines the mode: positive is for E-mode and negative is for D-mode. Using the established Level 1 MOSFET I_D - V_D characteristics model equations to describe the GaN FET current value in the saturation region reveals a large difference between experimentally measured and simulated data. Therefore, referring to a smoothing equation, the coefficient 1/2 in (3b) is replaced with 1/3 and that in (3c) is replaced with 2/3. The smoothing equation (4) is used to smoothen the I_D - V_D characteristic curve in the linear and saturation regions; the $V_{GS} - V_{TH}$ voltage value is modified to $V_{GS,eff}$ and substituted in (5a) and (5b). The + and - signs denote the D- and E-modes of the GaN FET, respectively, which complies with the I_D - V_D characteristics of the GaN FET model. The δ value impacts the degree of smoothness between the linear and saturated regions; the higher the value is, the smoother the curve is [24]. The smoothing equation is as follows:

$$V_{GS,eff} = (V_{GS} - V_{TH}) - \left(\frac{1}{3} \right) \left((V_{GS} - V_{TH}) - V_{DS} - \delta + \sqrt{((V_{GS} - V_{TH}) - V_{DS} - \delta)^2 \pm 4\delta(V_{GS} - V_{TH})} \right). \quad (4)$$

After smoothening, the GaN FET I_D - V_D characteristic equations for the linear and saturation regions are depicted as follows:

Linear region ($V_{DS} \leq V_{GS,eff}$):

$$I_{DS} = K_P \times \left[V_{GS,eff} \times V_{DS} - \frac{1}{3} V_{DS}^2 \right]. \quad (5a)$$

Saturation region ($V_{DS} > V_{GS,eff}$):

$$I_{DS} = \frac{2}{3} \times K_P \times V_{GS,eff}^2. \quad (5b)$$

SPICE simulation software [25] was used to simulate the electrical characteristics and to verify the measured gate drive signals. The Shenai model [23] was used and the built-in Level 1 MOSFET capacitance model was replaced with external capacitances. The measured gate-source capacitance was relatively independent of V_{DS} voltage, and a constant measured capacitance C_{GS} was used in the circuit model. The C_{GD} and C_{DS} can be described using the following equations:

$$C_{GD} = \frac{C_{GD0}}{(1 - V_{GD}/V_J)^m}, \quad (6a)$$

$$C_{DS} = \frac{C_{DS0}}{(1 - V_{DS}/V_J)^m}, \quad (6b)$$

where C_{GD0} is the zero-bias gate-to-drain capacitance, C_{DS0} is the zero-bias drain-to-source capacitance, V_{GD} is the gate-to-drain voltage, V_{DS} is the drain-to-source voltage, V_J is the junction built-in potential, and m is the junction grading coefficient. The parameters V_J and m were adjusted to obtain the optimal fit with the measured capacitance data. Moreover, the effect of external couple capacitances on V_{GS} during turn-off is considered.

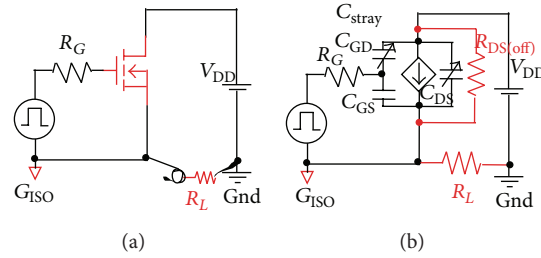


FIGURE 5: Simplified schematic of gate drive detecting circuit: (a) simplified schematic and (b) simplified equivalent model.

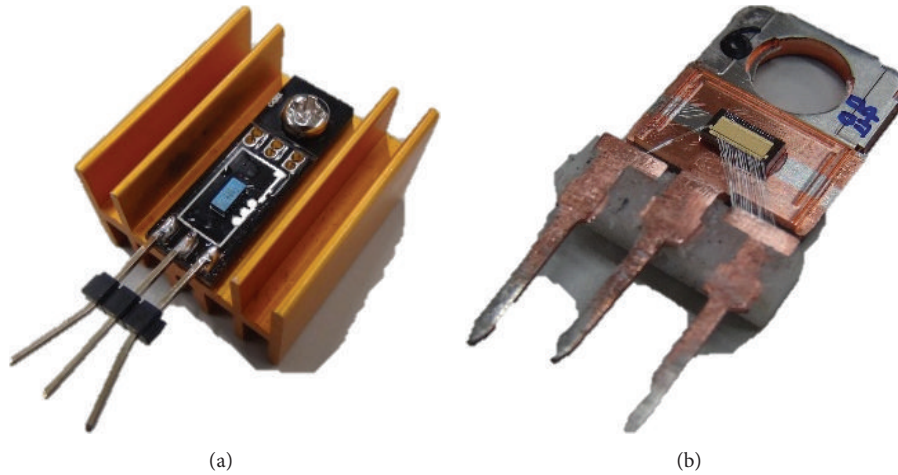


FIGURE 6: GaN FETs device under test: (a) E-mode GaN FET and (b) D-mode GaN FET.

3. Results and Discussion

3.1. I_D - V_D Characteristic Curve. E- and D-mode GaN FET devices under test are shown in Figure 6. The tested D-mode GaN FET chip is 80 mm in size and is packaged in the TO-3P form. Figure 7 depicts the measured I_D - V_D characteristics of the four power transistors. Solid lines represent the waveforms specified in the datasheets, dotted lines represent the measured waveforms, and solid lines with circles represent the SPICE-simulated waveforms.

The measured I_D - V_D characteristics of the E- and D-mode MOSFET waveforms are similar to those specified in the datasheet. The on-resistance $R_{DS(ON)}$ at a specific turn-on gate voltage V_{GS} and drain current I_{DS} can be extracted directly from the output characteristic curves.

Figure 8 plots the $R_{DS(ON)}$ of the four power transistors. In the enhanced MOSFET, $R_{DS(ON)}$ at $V_{GS} = 10$ V, $V_{DS} = 1.44$ V, and $I_{DS} = 4.5$ A is approximately $1.44/4.5 = 0.32 \Omega$, which is under the maximum value specified in the datasheet (0.4Ω). In the D-mode MOSFET, $R_{DS(ON)}$ at $V_{GS} = 0$ V, $V_{DS} = 1.66$ V, and $I_{DS} = 3$ A is approximately $1.66/3 = 0.55 \Omega$, which is close to the value specified in the datasheet (0.5Ω). Although the D-mode MOSFET V_{GS} is 0 V, it conducts current but not at full conduction. When V_{GS} is 5 V, V_{DS} is 30 V and

the output current I_D is 35 A. When V_{GS} is -2 V, the power transistor turns off and the output current I_D is close to zero. GaN FET output characteristic variation is considerably large compared with that of the MOSFET. The output current value exhibits drift phenomena in different E-mode GaN FET samples when the inputs V_{GS} and V_{DS} are the same. The experimental results show that the linear region of the on-resistance R_{ON} is approximately 0.025 – 0.03Ω . When V_{GS} is 5 V and the average output current I_D is 6 A, the average voltage V_{DS} is 0.18 V; therefore, the average on-state resistance R_{ON} is $0.18/6 = 0.03 \Omega$, which exceeds the datasheet value of 0.025Ω . The D-mode GaN FET on-resistance R_{ON} is approximately 0.25 – 0.30Ω . When V_{GS} is 0 V and V_{DS} is 1 V, I_D is 3.87 A; therefore, R_{ON} is $1/3.87 = 0.26 \Omega$.

Equations (5a) and (5b) are used to establish the current source model of a transistor. The output voltage V_{DS} of the E-mode GaN FET is increased from 0 to 3 V at intervals of 0.1 V, and the gate input voltage is increased from 0 to 5 V at intervals of 1 V; the output voltage V_{DS} of the D-mode GaN FET is increased from 0 to 10 V at intervals of 0.5 V, and the gate voltage is increased from -5 to 0 V at intervals of 1 V.

The waveforms are shown in Figures 7(c) and 7(d) as solid lines with circles; the simulated characteristics are similar to the measured characteristics (dashed lines). Drain current

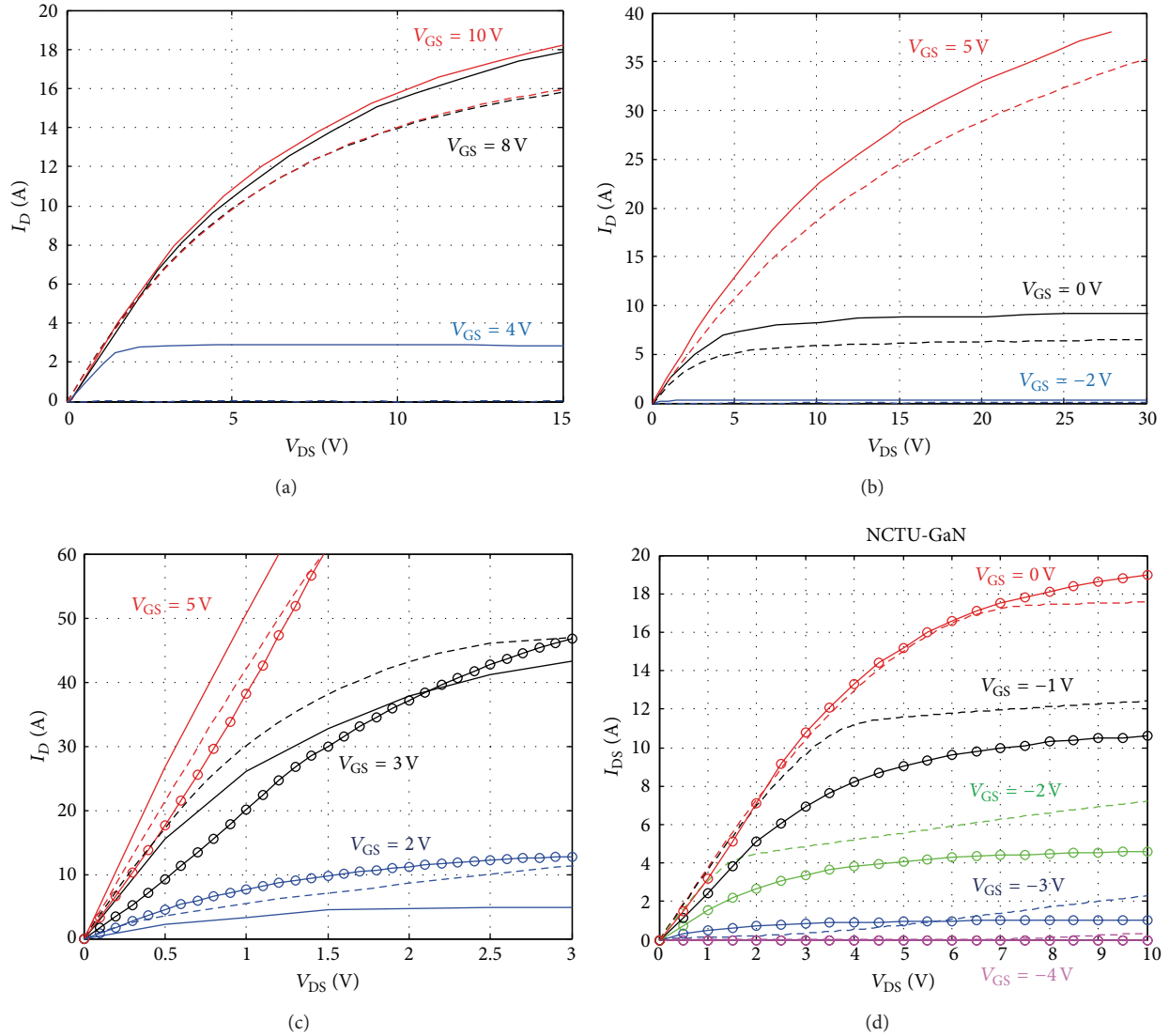


FIGURE 7: Output characteristics: (a) E-mode MOSFET, (b) D-mode MOSFET, (c) E-mode GaN FET, and (d) D-mode GaN FET.

I_{DS} (Y -axis) at a particular voltage V_{DS} (X -axis) can be obtained from the simulated waveform. In addition to the on-resistance R_{ON} characteristics, the saturation voltage of the D-mode GaN FETs exhibits variance. The experimental results show that the average saturation voltage is at $V_{DS} = 7$ V and that the maximum saturation current is between 16 and 18 A. The conduction resistance $R_{DS(ON)}$ of the D-mode GaN FET is 0.26Ω , which is smaller than those of the two MOSFET power transistor (0.32 and 0.55Ω) but much larger than that of the E-mode GaN FET (0.03Ω). In the future, $R_{DS(ON)}$ of the D-mode GaN FET can be improved using internal or external parallel methods [6, 7]; therefore, uniform performance should be sorted.

3.2. Threshold Voltage. The measured threshold voltage V_{TH} is plotted in Figure 9. The conduction threshold current of the MOSFET power transistor is defined as $250 \mu A$.

From the experimental results of the enhanced MOSFET, the threshold voltage V_{TH} is 3.21 V, which is in the range specified in the datasheet (2 – 4 V). Furthermore, the conduction threshold current of the D-mode MOSFET is $250 \mu A$; therefore, the gate threshold voltage V_{TH} is -2.98 V, which is in the range specified in the datasheet (-4 to -2 V). From the information in the manual, E-mode GaN FET conduction threshold current is defined as 3 mA.

In Figure 9(a), when the output current of the E-mode GaN FET is $3000 \mu A$, the gate threshold voltage V_{TH} is 1 V, which is in the range specified in the datasheet (0.7 – 2.5 V). The output current I_D of the D-mode GaN FET is plotted logarithmically in Figure 9(b). Near $V_{GS} = -3.9$ V, the output current I_D rises rapidly. Hence, this V_{GS} voltage is defined as the threshold voltage of the D-mode GaN FET. The threshold voltage V_{TH} of the E-mode GaN FET is much lower than that of the MOSFET.

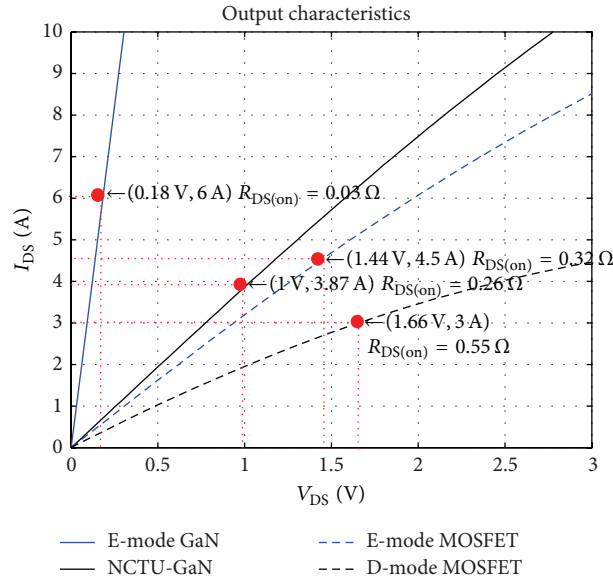


FIGURE 8: On-resistance of the four power transistors.

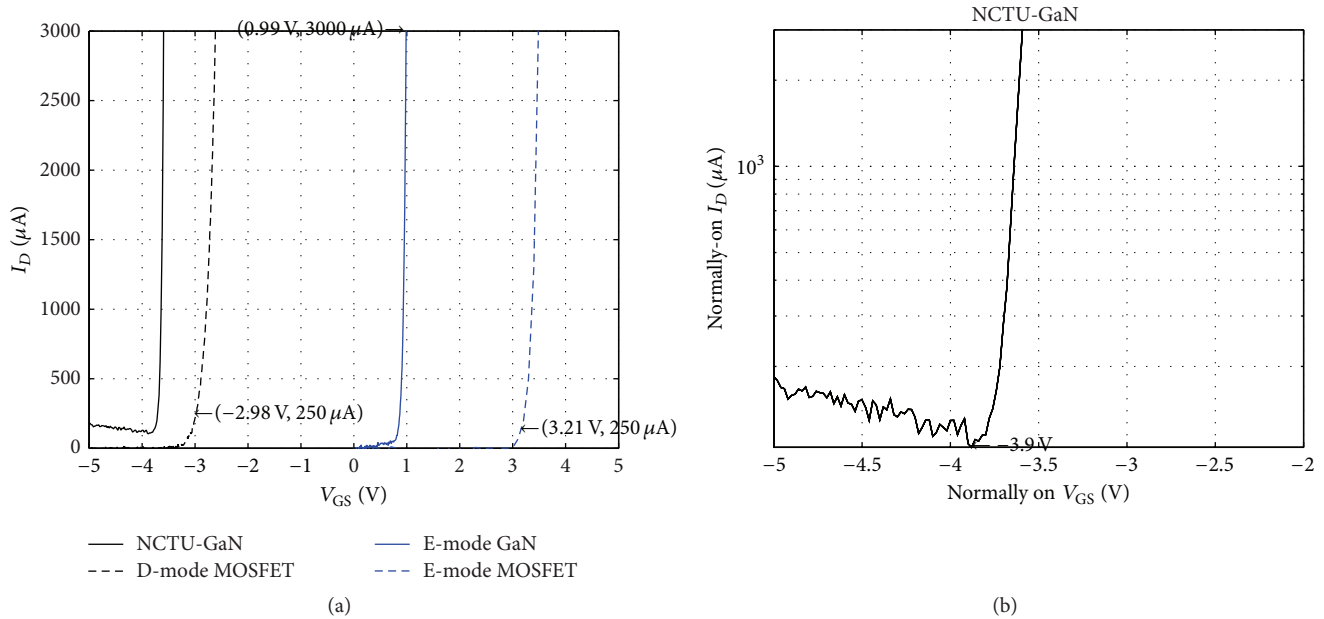


FIGURE 9: Transfer characteristics: (a) comparison of all transistors and (b) D-mode GaN FET.

3.3. Parasitic Capacitance. The datasheet provides power transistor parasitic capacitance characteristics, including the input capacitance (C_{ISS}), output capacitance (C_{OSS}), and transpose capacitance ($C_{RSS} = C_{GD}$), where $C_{ISS} = C_{GS} + C_{GD}$, $C_{OSS} = C_{GD} + C_{DS}$, and $C_{RSS} = C_{GD}$. Figure 10 plots the measured parasitic capacitance values of the four power transistors. From Figure 10(a), for the E-mode MOSFET, at $V_{GS} = 0$ V and the bias voltage $V_{DS} = 25$ V, the parasitic

capacitances C_{ISS} , C_{OSS} , and C_{RSS} are 553.8, 91.5, and 27.3 pF, respectively, which are close to the datasheet values (540 (typ.), 90 (typ.), and 35 pF (typ.), resp.). From Figure 10(b), the E-mode GaN FET, at $V_{GS} = 0$ V, and a bias voltage $V_{DS} = 100$ V, parasitic capacitances C_{ISS} , C_{OSS} , and C_{RSS} are 473.7, 301, and 16.7 pF, respectively, which are close to the datasheet values (540 (max.), 350 (max.), and 12 pF (max.)). From Figure 10(b), the D-mode MOSFET, at $V_{GS} = -10$ V,

TABLE 1: Comparison of datasheet and measured characteristics.

Parameter	Symbol	Test conditions	E-mode GaN FET Value	D-mode GaN FET Value	Unit
On-state resistance	$R_{DS(ON)}$	$V_{GS} = 5 \text{ V}$, $V_{DS} = 0.18 \text{ V}$, $I_D = 6 \text{ A}$	~25 m (max.)/30 m	—	Ω
		$V_{GS} = 0 \text{ V}$, $V_{DS} = 1 \text{ V}$, $I_D = 3.87 \text{ A}$	—	—/0.26	
Gate threshold voltage	V_{TH}	$V_{GS} = V_{DS}$, $I_D = 3 \text{ mA}$	0.99	—	V
		$V_{GS} = 7 \text{ V}$, $\log(I_D) = \text{min. A}$	—	—3.9	
Input capacitance	C_{ISS}	$V_{GS} = 0 \text{ V}$, $V_{DS} = 100 \text{ V}$, osc. level = 30 mV (E-mode)	540 (max.)/473.7	—	pF
		$V_{GS} = -5 \text{ V}$, $V_{DS} = 50 \text{ V}$, osc. level = 30 mV (D-mode)	—	—/72.7	
Output capacitance	C_{OSS}	$V_{GS} = 0 \text{ V}$, $V_{DS} = 100 \text{ V}$, osc. level = 30 mV (E-mode)	350 (max.)/301	—	pF
		$V_{GS} = -5 \text{ V}$, $V_{DS} = 50 \text{ V}$, osc. level = 30 mV (D-mode)	—	—/64.4	
Reverse transfer capacitance	C_{RSS}	$V_{GS} = 0 \text{ V}$, $V_{DS} = 100 \text{ V}$, osc. level = 30 mV (E-mode)	12 (max.)/16.7	—	pF
		$V_{GS} = -5 \text{ V}$, $V_{DS} = 50 \text{ V}$, osc. level = 30 mV (D-mode)	—	—/10.2	

Before slash: datasheet; after slash: measured

and a bias voltage $V_{DS} = 25 \text{ V}$, parasitic capacitances C_{ISS} , C_{OSS} , and C_{RSS} are 2361.7, 243.7, and 61.7 pF, respectively, and C_{ISS} is under the value specified in the datasheet (2800 pF (typ.)), whereas C_{OSS} and C_{RSS} are close to the datasheet values (255 (typ.), 64 pF (typ.)). For the E-mode GaN FET, at $V_{GS} = 0 \text{ V}$ and $V_{DS} = 100 \text{ V}$, parasitic capacitances C_{ISS} , C_{OSS} , C_{RSS} are 473.7, 301, and 16.7 pF, respectively, which are close to the datasheet values (540 (max.), 350 (max.), and 12 pF (max.)). For the D-mode GaN FET, at $V_{GS} = -5 \text{ V}$ and $V_{DS} = 50 \text{ V}$, the parasitic capacitances C_{ISS} , C_{OSS} , and C_{RSS} are 72.7, 64.4, and 10.2 pF, respectively. Comparison of datasheet and measured characteristics are listed in Table 1, and Table 2 lists the important I - V and capacitance model parameters for E- and D-mode used in this study.

According to (6a) and (6b), the parameters listed in Table 2 are used. The relationships $C_{ISS} = C_{GS} + C_{GD}$, $C_{OSS} = C_{GD} + C_{DS}$, and $C_{RSS} = C_{GD}$ are used. Plots of C_{ISS} , C_{OSS} , and C_{RSS} are shown in Figures 10(c) and 10(d). The simulated and experimental curves are similar.

3.4. Isolated Gate Drive Detection. A turn-off voltage of 0 V is used for the E-mode GaN FET; therefore, the full-conduction voltage is limited to 5.5 V. For the D-mode GaN FET, the used turn-off voltage is -5 V , and full-conduction voltage is limited to 2 V. Hence, the driving voltage for the E-mode GaN FET gate-to-source voltage is set to 0–5 V; in other words, V_{ISO} is set to 5 V, and the D-mode GaN FET gate source driving voltage is set to -5 to 0 V. At driving voltages of 0–5 V and -5 to 0 V, the E- and D-mode MOSFET waveforms can be contrasted. Regardless of the MOSFET mode, the voltage probe was used to measure the voltage between the gate terminal and the ground terminal. The E-mode MOSFET waveforms are the same as the ideal isolated gate drive circuit detection signal, as depicted in Figures 3 and 4; the gate voltage when turned on is +29 V and decreases to 0 V when turned off (Figure 11(a)). The D-mode MOSFET gate voltage waveform is +24 V, which decreases to 0 when turned off (Figure 11(b)). When measuring the E-mode GaN FET, the gate voltage is +29 V when turned on, but a difference in

TABLE 2: Simulation model parameters.

Symbol	GaN FETs model parameter		
	Parameter	E-mode	D-mode
K_p	Transconductance parameter (A/V^2)	24	2.1
V_{TO}	Zero-bias threshold voltage	1 V	-3.9 V
δ	Fitting parameter to adjust the curvature	0.4	0.6
C_{GS}	External gate to source capacitance (nF)	0.45	0.06
C_{GD}	External gate to drain capacitance		
	C_{GD0} (nF)	0.1	0.02
	V_j (V)	0.66	0.75
	m	0.39	0.14
C_{DS}	External drain to source capacitance		
	C_{DS0} (nF)	0.89	0.07
	V_j (V)	0.4	0.35
	m	0.22	0.05
C_{stray}	Stray capacitance in the circuit (nF)	2	2
R_L	Voltage probe resistance (Ω)	10 M	1 M
$R_{DS(off)}$	GaN FET turn-off resistance (Ω)	7.647 M	904.8 k

voltage level exists between the gate and the ground. The large change in the voltage level is in the 0–24 V range, as shown in Figure 12(a). D-mode GaN FETs exhibit the same phenomenon, as shown in Figure 12(b). The differences are caused by the turn-off impedance $R_{DS(off)}$. The larger the turn-off impedance is, the smaller the leakage current is; the across voltage $V_{S(off)}$ is small, and the difference between source-to-ground voltage value is close to 0. Conversely, when the turn-off impedance is small, the leakage current is large, and the source-to-ground voltage approaches +24 V. Therefore, the turn-off ability of GaN FETs can indirectly screen device uniformity. Moreover, the impedance value can be quantified.

When $V_{GS} = 5$ V, the E-mode GaN FET turns on. The gate-to-ground voltage is +29 V; when $V_{GS} = 0$ V, the E-mode GaN FET turns off, which is equivalent to the turn-off resistance $R_{DS(off)}$; the voltage probe resistance is R_L . When the Kirchhoff circuit laws are applied, the power supply voltage V_{DD} through $R_{DS(off)}$ and R_L generate the leakage drain current I_{DSS} . Through the isolated gate drive circuit architecture, the voltage probe resistance R_L is 10 M Ω and power supply voltage V_{DD} is 24 V. The $V_{S(off)}$ values for the two modes are 13.6 V and 23.0 V, as shown in Figure 12(a). Substituting these values into (2), $R_{DS(off)}$ is obtained as 7.647 and 0.435 M Ω . Using a digital multimeter in series with the source terminal and the voltage probes (R_L) to measure the GaN FET device during the turn-off state, the leakage currents I_{DSS} are obtained as 1.340 and 2.365 μ A. By substituting $V_{S(off)}$ in (1a), leakage currents I_{DSS} are obtained as 1.36 and 2.30 μ A, which are similar to the measured values.

Next, the gate-to-ground voltage waveform of the D-mode GaN FET is measured. When V_{GS} is 0 V, the D-mode GaN FET drain and source conducts and shorts, and the source terminal voltage is +24 V. Because $V_{GS} = 0$ V, the gate terminal voltage is +24 V; when $V_{GS} = -5$ V, the GaN FET is

off, because the resistance of the D-mode GaN FET $R_{DS(off)}$ is not large enough; therefore, leakage current flows, and the source terminal voltage relative to ground cannot be reduced to 0 V. Next, the turn-off voltage of the D-mode GaN FET is measured using the 10 M Ω voltage probe; the value is always 19 V. The turn-off impedance $R_{DS(off)}$ is much lower than 10 M Ω ; therefore, the voltage probe is adjusted to 1 M Ω to repeat the experiments. $V_{S(off)}$ is in the 0–19 V range. $R_{DS(off)}$ and voltage probe $R_L = 1$ M Ω divide the voltage, assuming that the probe is measured as $V_{S(off)}$ voltage. From (1a), (1b), and (2), the leakage current I_{DSS} and turn-off impedance $R_{DS(off)}$ can be obtained.

The waveform variability of the D-mode GaN FET is similar to that of the E-mode GaN FET, as shown in Figure 12(b). The D-mode GaN FET under a voltage probe $R_L = 1$ M Ω varies in the 16–20 V range. From (2), $R_{DS(off)}$ of the D-mode GaN FET is 463.4 k Ω when $V_{S(off)}$ is 16.4 V and 904.8 k Ω when $V_{S(off)}$ is 12.6 V. However, when $V_{S(off)}$ exceeds 24 - 5 = 19 V, the turn-off impedance is insufficient and the transistor does not turn off.

In the E-mode GaN FET, the threshold voltage V_{TH} of the output characteristic curve I - V model parameter is set to 1 V and K_p is set to 24. An external capacitor is used as listed in Table 2. In the isolated gate driver circuit architecture, the voltage probe resistance $R_L = 10$ M Ω , power supply voltage $V_{DD} = 24$ V, and measuring voltage $V_{S(off)} = 13.6$ V. From (2), $R_{DS(off)}$ impedance is derived as 7.647 M Ω when $V_{S(off)}$ is 13.6 V; therefore, when E-mode GaN FET turns off, the drain-to-source $R_{DS(off)}$ is equivalent to a 7.647 M Ω resistor. R_L is the internal voltage probe resistance, which is 10 M Ω at 10x magnification. In the D-mode GaN FET, the threshold voltage V_{TH} of its I - V output characteristic curve model is -3.9 V and K_p is 2.1. The external capacitor is used as parasitic capacitance. The turn-off impedance $R_{DS(off)}$ of

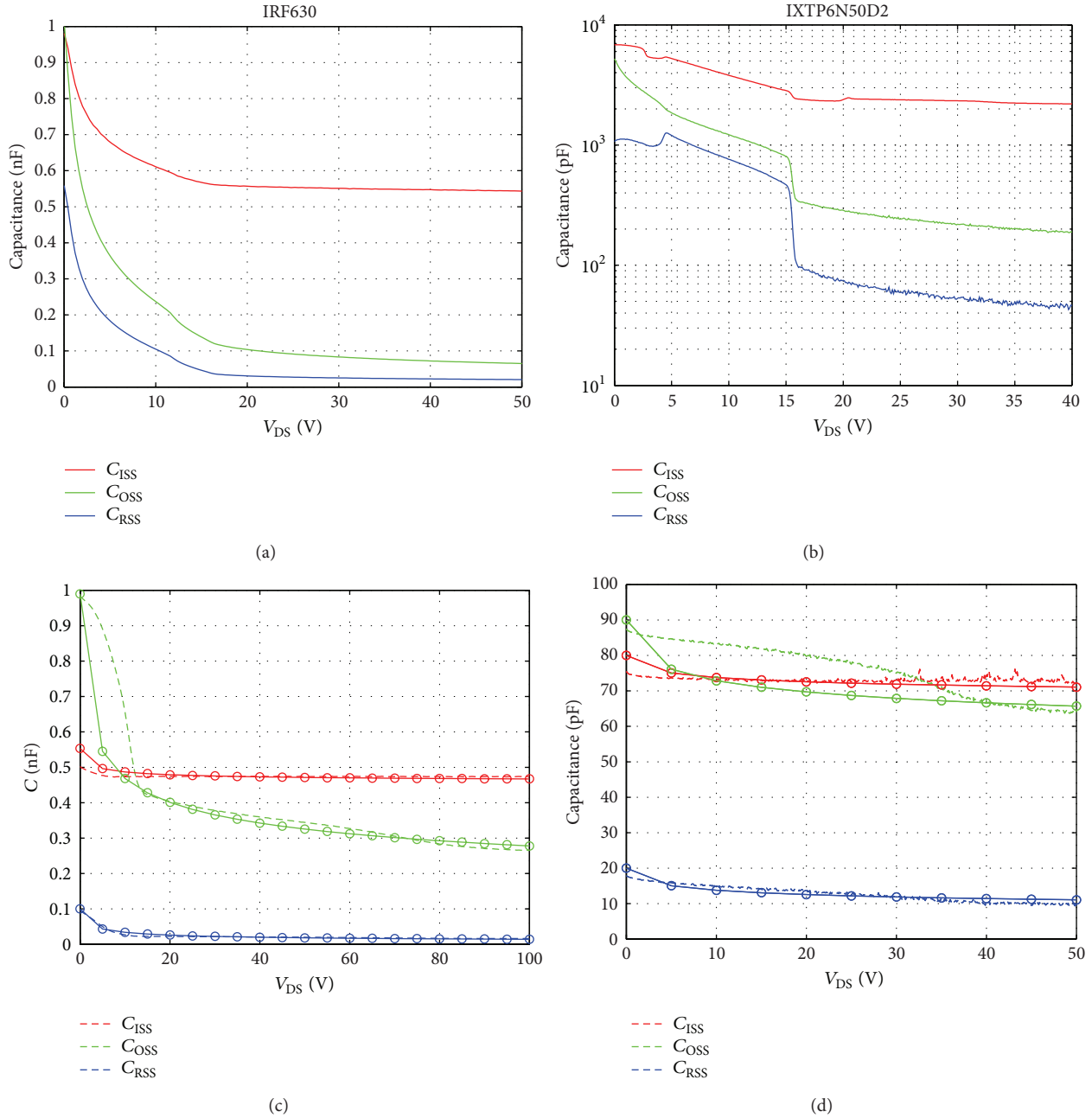


FIGURE 10: Parasitic capacitance: (a) E-mode MOSFET, (b) D-mode MOSFET, (c) E-mode GaN FET, and (d) D-mode GaN FET.

the experimental device using the 10x magnification voltage probe is much lower than 10 MΩ. Hence, a 1x (1 MΩ) probe is used to measure ($R_L = 1\text{ M}\Omega$); the power supply voltage $V_{DD} = 24\text{ V}$ and the measured $V_{S(\text{off})}$ voltage = 12.6 V. From (2), when $V_{S(\text{off})}$ voltage is 12.6 V, $R_{DS(\text{off})}$ is 904.8 kΩ. The equivalent turn-off resistance $R_{DS(\text{off})}$ between the drain-source is equivalent to 904.8 kΩ.

SPICE circuits are established through the equivalent model described in Figure 5. The gate resistor uses 100 Ω R_G , and the E-mode GaN FET gate terminal wave signal V_{GS} voltage is 0–5 V, whereas the D-mode GaN FET V_{GS} is –5 to 0 V. Gate pulse width, period, and frequency of the PWM

signal are 100 μs, 500 μs, and 2 kHz, respectively. The numerical analysis software predicts that the gate drive circuit board has external drain-source stray capacitance C_{stray} and that the actual measurements of waveform segments have a slower falling slope. Because of stray capacitance C_{stray} parallel to drain-to-source and gate-to-drain, the turn-off V_{GS} slope falls slowly in the waveform. The estimates of the stray capacitance C_{stray} value are 2 nF. The GaN FET gate detection simulation parameters are shown in Table 2.

Figures 13 and 14 present the E- and D-mode GaN FET gate detection simulation circuit waveform as shown in black line and measurement waveform as shown in orange

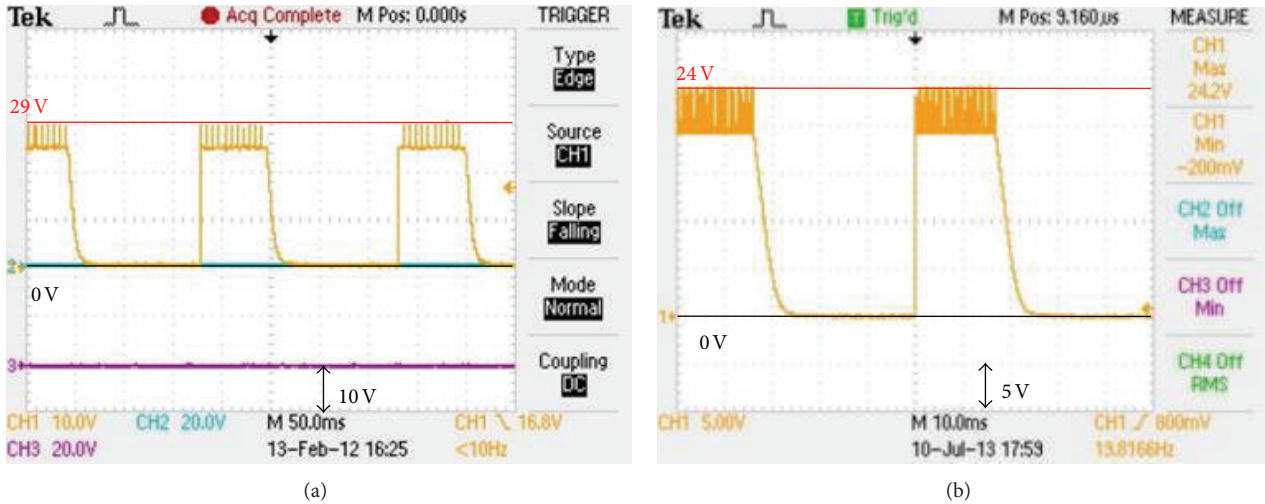


FIGURE 11: MOSFET gate drive detection signal waveforms: (a) E-mode and (b) D-mode.

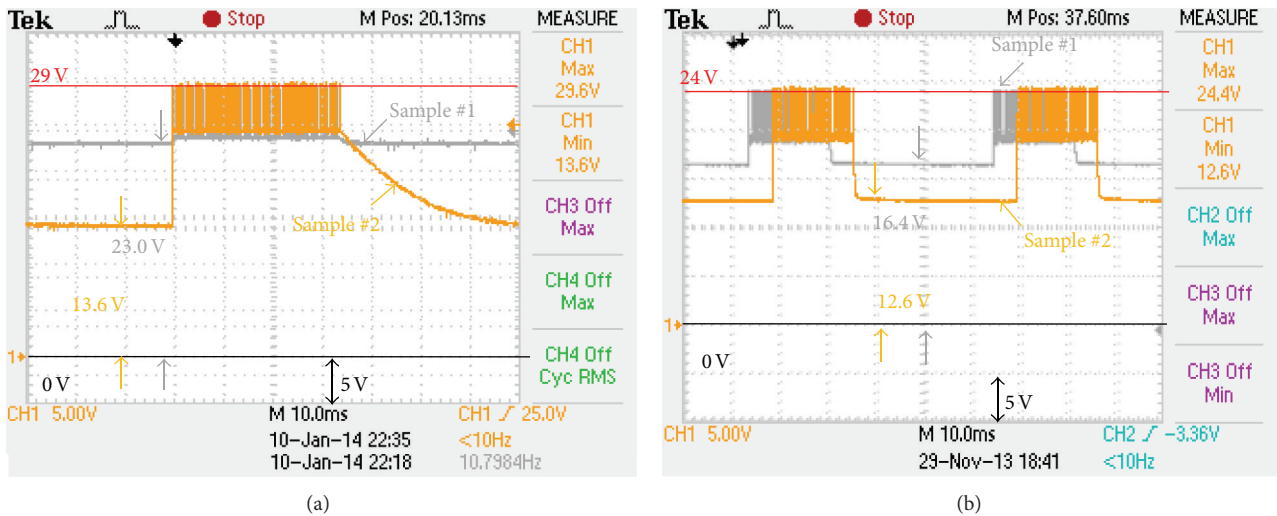


FIGURE 12: GaN FET gate drive detection signal waveforms: (a) E-mode and (b) D-mode.

line superimposing they are matching each other. When the isolated gate detection circuit stops sending the PWM signal to the gate terminal and GaN FET is set to close long enough, the falling slope waveform segment of the discharge through circuit stray capacitance C_{stray} and load resistor R_L from +24 V floating voltage discharge to the voltage $V_{S(off)}$ is in accordance with the measurement. The influence of the parasitic capacitance of the input capacitance C_{ISS} on V_{GS} voltage switching waveform can be observed by enlarging the V_{GS} voltage signal timeline, as shown in the inset of Figures 13(a), 13(b) and 14(a), 14(b); the enlarged V_{GS} voltage signal charge and discharge waveforms are shown in Figures 13(c), 13(d), 14(c), and 14(d). The simulation and experimental gate voltage waveforms of the charge and discharge match perfectly.

The results of the screening and recording of the turn-off voltage $V_{S(off)}$ and the corresponding $R_{DS(off)}$ of the E-mode GaN FET voltages are shown in Figure 15. The off-resistance of E-mode GaN FETs is larger than 1 M Ω , whereas those of D-mode GaN FETs are approximately in the 0.5–1.5 M Ω range.

4. Conclusions

The on-resistance $R_{DS(ON)}$ of E-mode GaN FET and NCTU D-mode GaN FET is 0.025–0.03 Ω and 0.25–0.3 Ω ; both of these values are lower than that of MOSFET. Nevertheless, NCTU's D-mode GaN FET can be further improved using the parallel method to reduce on-resistance. Regarding parasitic capacitance, the C_{RSS} of the E-mode GaN FET is far lower

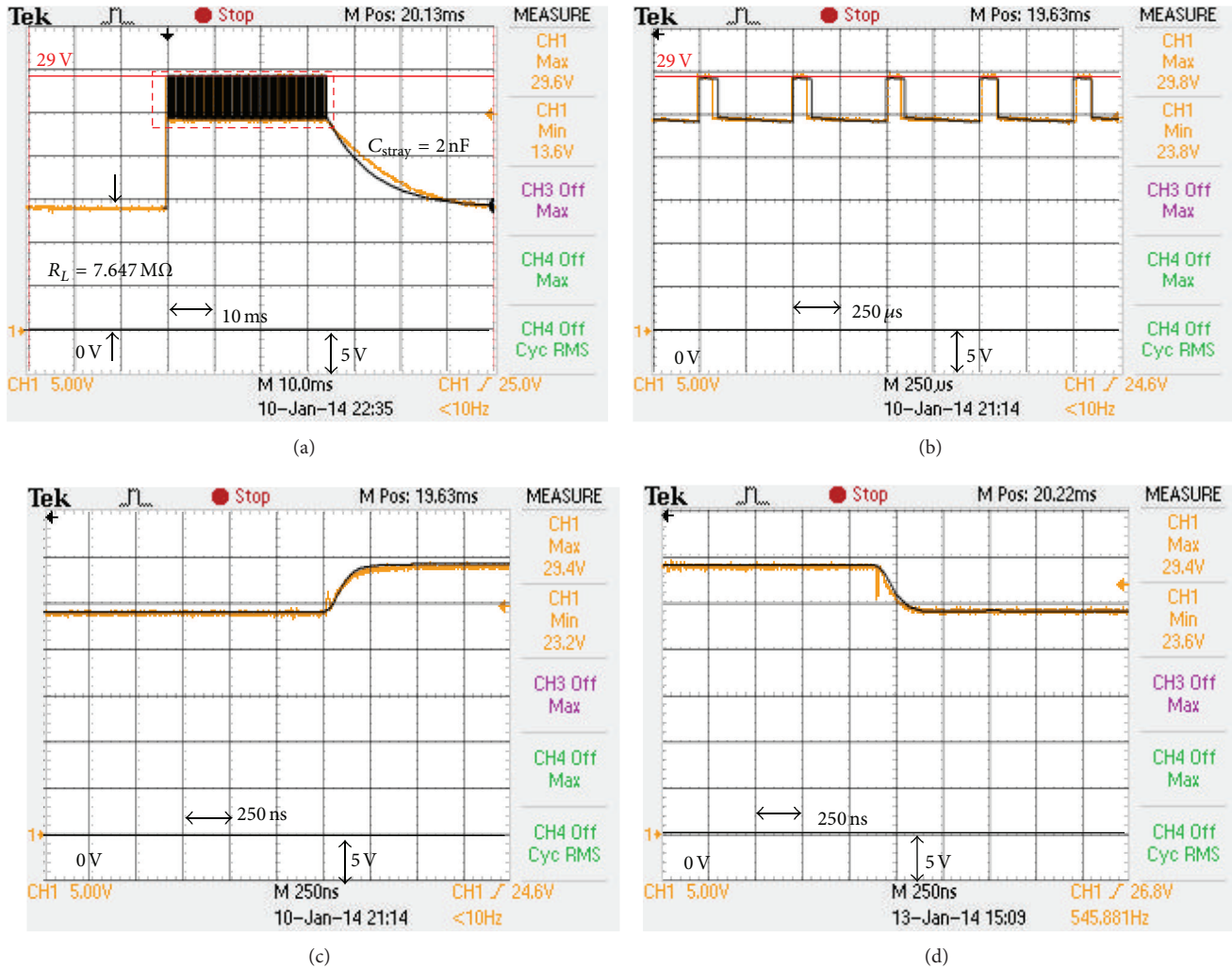


FIGURE 13: Simulation results of E-mode GaN FET.

than that of the enhanced MOSFET; a smaller C_{RSS} capacitance value indicates that the Miller plain area is relatively short and that the switching time is shorter. Compared with the turn-off resistance of different samples, the electrical characteristics of each MOSFET device are highly consistent, whereas those of GaN FET exhibit less uniformity. GaN FETs are currently under development, and the electrical characteristics of each component are relatively unstable; the variability is larger than that in MOSFET. This study established a standardized electrical measurement procedure that provides necessary information for designers. In addition, a simple and accurate GaN FET model was established on the basis of the measured electrical characteristics. The simulation waveforms can be used to obtain information on GaN FET's internal parasitic capacitance, turn-off impedance $R_{\text{DS(off)}}$, and stray capacitance C_{stray} in the inverter circuit board. The proposed GaN FET isolated gate drive circuit screening method by $R_{\text{DS(off)}}$ detection provides a simple uniformity sorting method. The results show that the higher the off-state voltage $V_{\text{S(off)}}$ is, the smaller the turn-off voltage

$V_{\text{DS(off)}}$ is; in other words, the device has a lower $R_{\text{DS(off)}}$. The leakage current in GaN devices is much larger than that in MOSFET devices in the turn-off state. The off-resistance of MOSFET is generally larger than 10 MΩ. By contrast, the off-resistance of E-mode GaN FETs is larger than 1 MΩ, whereas those of D-mode GaN FETs are approximately in the 0.5–1.5 MΩ range. Devices with the same off-state voltage $V_{\text{S(off)}}$ perform similarly. Moreover, the larger the turn-off resistance $R_{\text{DS(off)}}$ is, the closer the characteristics are to those specified in the datasheet.

Conflict of Interests

The authors declare that there is no conflict of interests regarding the publication of this paper.

Acknowledgments

This work was supported by the CSIST Project CSIST-0101-V108(104), Taiwan. The authors would like to thank

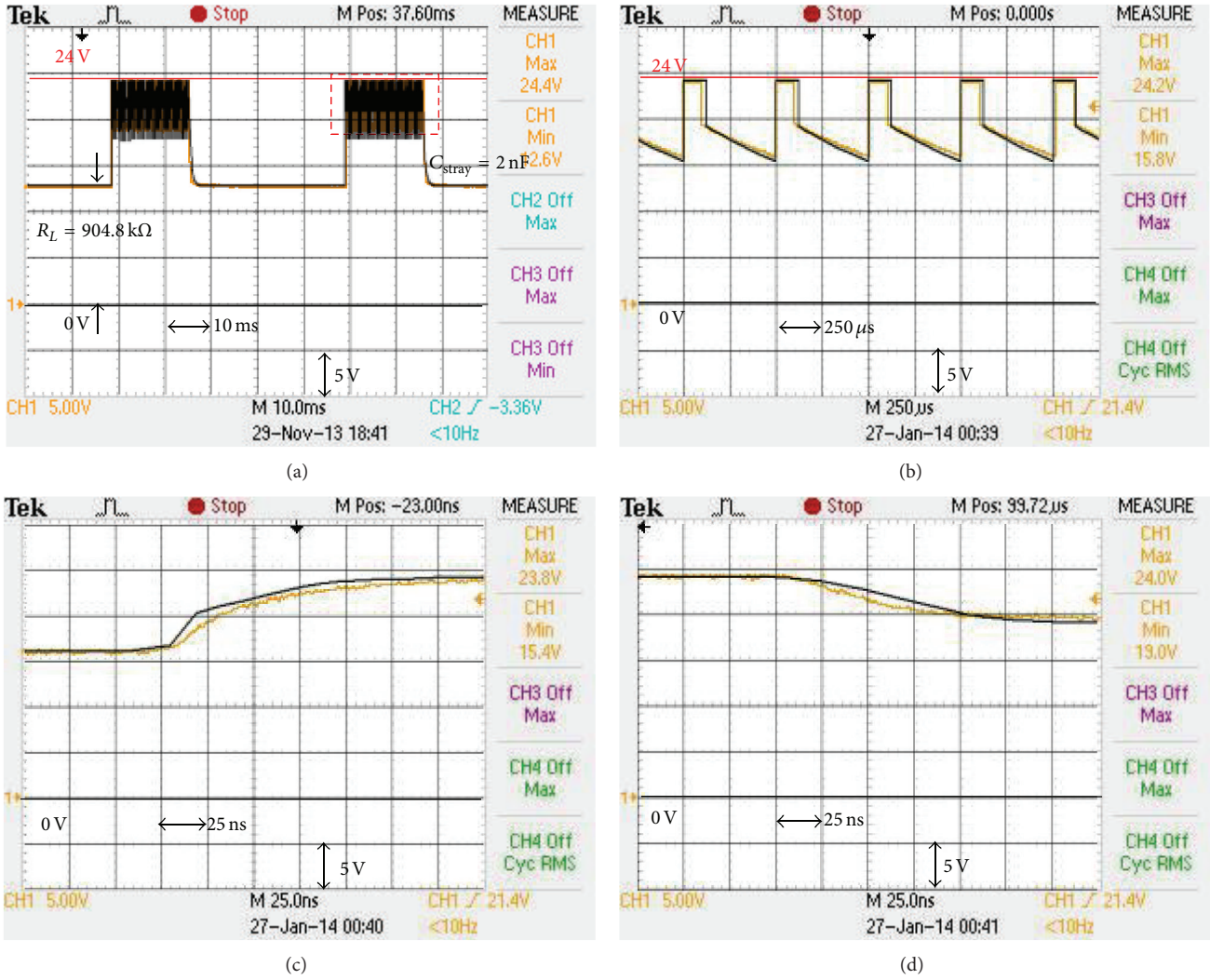


FIGURE 14: Simulation results of D-mode GaN FET.

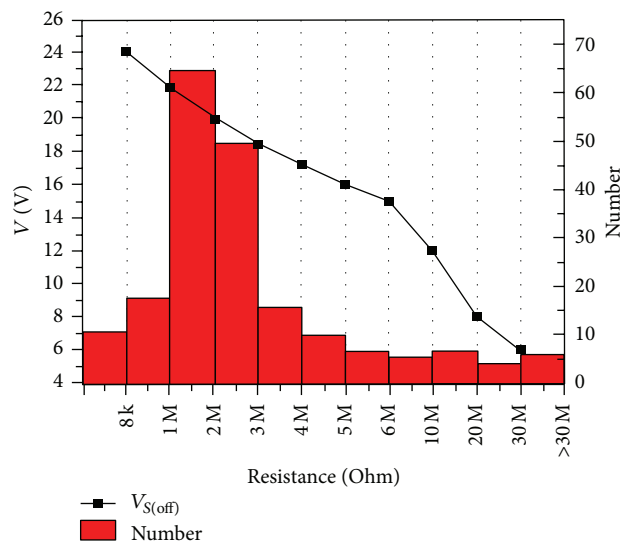


FIGURE 15: The turn-off voltage $V_{S(\text{off})}$ and the corresponding $R_{DS(\text{off})}$ of E-mode GaN FETs.

Professor Edward Yi Chang of NCTU for supporting GaN devices, Professor Stone Cheng of NCTU for supporting package technology, and National Nano Device Laboratories, Hsinchu, Taiwan, for their very helpful suggestions and technical support.

References

- [1] B. Ozpineci, L. M. Tolbert, S. K. Islam, and M. Chinthavali, "Comparison of wide bandgap semiconductors for power applications," in *Proceedings of the 10th European Conference on Power Electronics and Applications*, Toulouse, France, September 2003.
- [2] K. Shenai, M. Dudley, and R. F. Davis, "Rugged electrical power switching in semiconductors: a systems approach," *Proceedings of the IEEE*, vol. 102, no. 1, pp. 35–52, 2014.
- [3] T. Ueda, M. Ishida, T. Tanaka, and D. Ueda, "GaN transistors on Si for switching and high-frequency applications," *Japanese Journal of Applied Physics*, vol. 53, no. 10, Article ID 100214, pp. 1–8, 2014.
- [4] K. Shirabe, M. M. Swamy, J.-K. Kang et al., "Efficiency comparison between Si-IGBT-based drive and GaN-based drive," *IEEE Transactions on Industry Applications*, vol. 50, no. 1, pp. 566–572, 2014.
- [5] B. Wang, N. Tipirneni, M. Riva, A. Monti, G. Simin, and a. E. Santi, "An efficient high-frequency drive circuit for GaN power HFETs," *IEEE Transactions on Industry Applications*, vol. 45, no. 2, pp. 843–853, 2009.
- [6] P. Chou, S. Cheng, and S. Chen, "Evaluation of thermal performance of all-GaN power module in parallel operation," *Applied Thermal Engineering*, vol. 70, no. 1, pp. 593–599, 2014.
- [7] S. Tsai, H. Hsu, Y. Tu, and E. Y. Chang, "Investigation of electrical and thermal properties of multiple AlGaIn/GaN high-electron-mobility transistors flip-chip packaged in parallel for power electronics," *Applied Physics Express*, vol. 8, no. 3, Article ID 034101, 4 pages, 2015.
- [8] H. Umegami, F. Hattori, Y. Nozaki, M. Yamamoto, and O. Machida, "A Novel high-efficiency gate drive circuit for normally off-type GaN FET," *IEEE Transactions on Industry Applications*, vol. 50, no. 1, pp. 593–599, 2014.
- [9] Y. Xi, M. Chen, K. Nielson, and R. Bell, "Optimization of the drive circuit for enhancement mode power GaN FETs in DC-DC converters," in *Proceedings of the 27th Annual IEEE Applied Power Electronics Conference and Exposition (APEC '12)*, pp. 2467–2471, IEEE, Orlando, Fla, USA, February 2012.
- [10] J. Strydom and A. Lidow, "Driving eGaN transistors for maximum performance," 2011, <http://epc-co.com/>.
- [11] P. Jacqmaer, J. Everts, R. Gelagaevz, P. Tant, and J. Driesen, "Fast robust gate-drivers with easily adjustable voltage ranges for driving normally-on wide-bandgap power transistors," in *Proceedings of the 14th International Power Electronics and Motion Control Conference (EPE-PEMC '10)*, pp. T244–T251, Ohrid, Macedonia, September 2010.
- [12] How to Drive GaN Enhancement Mode Power Switching Transistors, GaNSystems Application Note GN001, <http://www.gansystems.com/>.
- [13] Designing Hard-switched Bridges with GaN, Transphorm Application Note AN0004, <http://www.transphormusa.com/>.
- [14] L. Balogh, "Design and application guide for high speed MOSFET gate drive circuit," in *Proceedings of the 2001 Power Supply Design Seminar*, Texas Instruments, 2001.
- [15] Design and Application Guide of Bootstrap Circuit for High Voltage Gate Drive IC, Fairchild Application Note AN-6076, <http://www.fairchildsemi.com/>.
- [16] IRF630 ST Microelectronics Datasheet, <http://www.st.com/>.
- [17] IXTA6N50D2, IXTP6N50D2, IXTH6N50D2 Datasheet, <http://ixdev.ixys.com/DataSheet/DS100177B%28IXTA-TP-TH6N50D2%29.pdf>.
- [18] EPC2010 Datasheet, <http://epc-co.com/>.
- [19] EPC GaN Transistor Parametric Characterization Guide, <http://epc-co.com>.
- [20] A. Ortiz-Conde, F. J. García Sánchez, J. J. Liou, A. Cerdeira, M. Estrada, and Y. Yue, "A review of recent MOSFET threshold voltage extraction methods," *Microelectronics Reliability*, vol. 42, no. 4–5, pp. 583–596, 2002.
- [21] Agilent Technologies, Agilent B1505A Power Device Analyzer/Curve Tracer, Step by Step Measurement Handbook for Power MOSFET, <http://www.agilent.com/>.
- [22] Fairchild AN-9005, Driving and Layout Design for Fast Switching. Super-Junction MOSFETs, <http://www.semi.com/an/AN/AN-9005.pdf>.
- [23] K. Shah and K. Shenai, "Simple and accurate circuit simulation model for gallium nitride power transistors," *IEEE Transactions on Electron Devices*, vol. 59, no. 10, pp. 2735–2741, 2012.
- [24] Y. Cheng, M.-C. Jeng, Z. Liu et al., "A physical and scalable I-V model in BSIM3v3 for analog/digital circuit simulation," *IEEE Transactions on Electron Devices*, vol. 44, no. 2, pp. 277–287, 1997.
- [25] IsSpice4 User's Guide, <http://www.intusoft.com>.

Research Article

Diamond Based Field-Effect Transistors of Zr Gate with SiN_x Dielectric Layers

W. Wang, C. Hu, S. Y. Li, F. N. Li, Z. C. Liu, F. Wang, J. Fu, and H. X. Wang

Key Laboratory for Physical Electronics and Devices of the Ministry of Education, Xi'an Jiaotong University, Shaanxi, Xi'an 710049, China

Correspondence should be addressed to H. X. Wang; hwxwangcn@mail.xjtu.edu.cn

Received 24 March 2015; Accepted 23 April 2015

Academic Editor: Jose Alvarez

Copyright © 2015 W. Wang et al. This is an open access article distributed under the Creative Commons Attribution License, which permits unrestricted use, distribution, and reproduction in any medium, provided the original work is properly cited.

Investigation of Zr-gate diamond field-effect transistor with SiN_x dielectric layers (SD-FET) has been carried out. SD-FET works in normally on depletion mode with p-type channel, whose sheet carrier density and hole mobility are evaluated to be $2.17 \times 10^{13} \text{ cm}^{-2}$ and $24.4 \text{ cm}^2 \cdot \text{V}^{-1} \cdot \text{s}^{-1}$, respectively. The output and transfer properties indicate the preservation of conduction channel because of the SiN_x dielectric layer, which may be explained by the interface bond of C-N. High voltage up to -200 V is applied to the device, and no breakdown is observed. For comparison, another traditional surface channel FET (SC-FET) is also fabricated.

1. Introduction

Diamond appears promising for high-power and high-frequency devices, since it has remarkable properties, such as wide band gap (E_g) of 5.47 eV, the highest thermal conductivity ($22 \text{ W/cm}\cdot\text{K}$), high breakdown field (10 MV/cm), high carrier mobility of electron $4500 \text{ cm}^2 \cdot \text{V}^{-1} \cdot \text{s}^{-1}$, hole $3800 \text{ cm}^2 \cdot \text{V}^{-1} \cdot \text{s}^{-1}$, and high carrier velocity (10^7 cm/s) [1–4]. However, due to the large activation energies of dopants (boron, phosphorus, and nitrogen) for diamond at room temperature, carrier concentrations in the diamond are very low [1, 5], which limit the development of the diamond-based semiconductor devices. Recently, most FETs based on diamond focus on the hydrogen-terminated surface [6–9], which can introduce a p-type conduction layer with a sheet hole density and hole mobility of 10^{13} cm^{-2} and $50\text{--}150 \text{ cm}^2 \cdot \text{V}^{-1} \cdot \text{s}^{-1}$ [10, 11], respectively. In this case, a two-dimensional hole gas (2DHG) exists near the surface of the diamond, associated with the electrochemical potential of adsorbates on a humidity saturated surface [12]. Thus, the conduction surface is thermally and chemically instable and vulnerable to the ambient environment. The oxidation of diamond surface or higher annealing even in vacuum could lead to the missing of 2DHG and degrade the performance of FET device.

This problem can be solved by applying dielectric layers to the diamond surface to maintain the conduction channel for stabilizing or replacing the adsorbates. Various dielectric layers of the H-terminated diamond surface, such as SiO_2 [13], Al_2O_3 [14], AlN [15], HfO_2 [16], LaAlO_3 [17], Ta_2O_5 [18], and ZrO_2 [19], have been mainly used as the insulators by the method of thermal evaporation, atomic layer deposition (ALD), or metal organic chemical vapor deposition (MOCVD). However, there are few reports on using dielectric of SiN_x .

In this paper, the single crystal diamond FET with SiN_x layers was proposed, and its properties were studied. For comparison, traditional H-termination surface channel FET was also fabricated.

2. Device Fabrication

Undoped homoepitaxial diamond films were grown on high-temperature high-pressure (HTHP) synthesized (001) Ila single crystal diamond substrates with the dimension of $3 \times 3 \times 0.5 \text{ mm}^3$ by a microwave plasma CVD system (AX5200S Seki Technotron Corp.). Before growth, the substrates were dipped into a mixed acid of HNO_3 and H_2SO_4 (1:1) at 250°C for 1 hour to remove nondiamond phase. During growth, the total flow rate of the reaction gas was 500 sccm, and

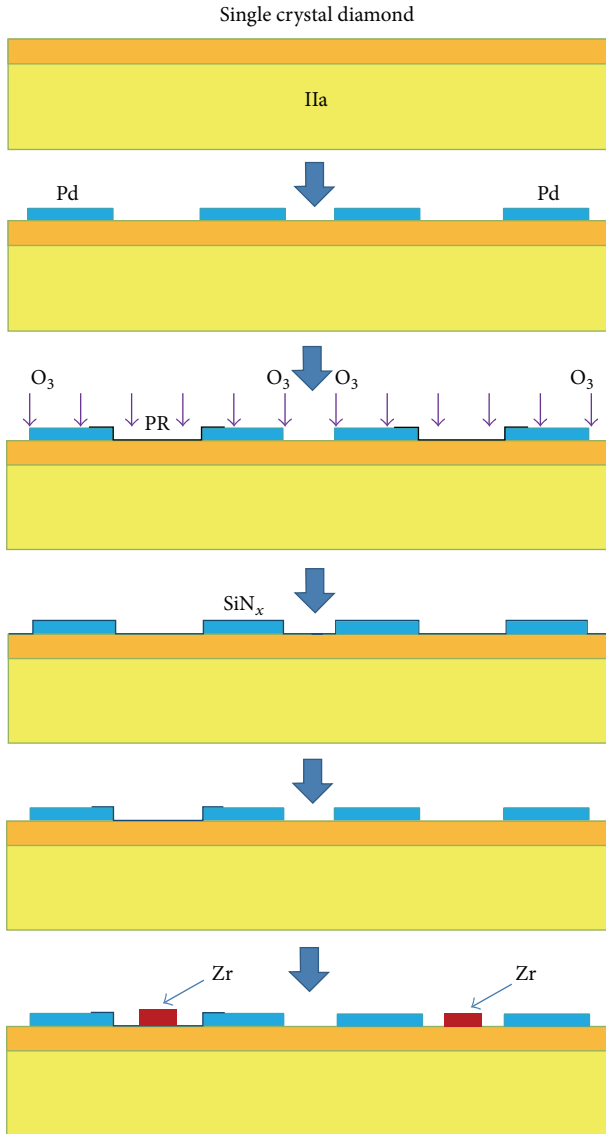


FIGURE 1: The process flow of the device fabrication.

the ratio of CH₄/H₂ was 1%. The process pressure, growth temperature, and microwave power were 100 Torr, 900°C, and 1kW, respectively. After growth, the samples were kept in hydrogen plasma for 1 minute at 900°C to generate a hydrogen-terminated surface.

The fabrication began with a standard lithography to pattern the drain and source electrodes before the metal evaporation. A carbon soluble metal palladium (Pd) was selected as the electrodes because of its good adhesion and relatively low specific contact resistance with the diamond surface [20]. Next, mesa isolation, protected by the photoresist, was performed on the grown diamond film by irradiation of O₃ and UV rays for 15 mins. The SiN_x dielectric layer was then deposited onto the surface at the temperature of 250°C and etched using BOE (6 : 1) solution for the patterns. Some of the device's channels were not covered with SiN_x for comparison. Zirconium (Zr) as the gate metal was finally

sputtered onto the channels. The total fabrication process procedure is shown in Figure 1. The gate length (L_G) and width (W_G) for both of the devices were 3 μm and 90 μm , respectively. The electrical properties of the device with and without SiN_x layers were then investigated.

3. Results and Discussion

The optical microscope and AFM images of as-deposited single crystal diamond epitaxial films are shown in Figure 2. Figure 2(a) presents the full-scale of the growth film with the dimension of 3 \times 3 mm²; no point defect pits and steps are found in the surface, indicating remarkable quality for electronic device fabrication. Figure 2(b) displays the AFM image in the area of 5 \times 5 μm^2 . The root mean square (RMS) roughness was measured to be 0.446 nm, illustrating an adequate morphology for device fabrication.

The room temperature properties of the Zr-gate diamond based field-effect transistors were investigated. The output characteristics are exhibited in Figure 3, where the drain current (I_D) has been normalized with respect to W_G . The blue solid line and the red dash dotted line indicate the FETs with and without SiN_x gate dielectric, respectively. As can be seen in Figure 3, the absolute value of I_D ($|I_D|$) for SD-FET increases with an increasing absolute value of V_{GS} ($|V_{GS}|$), confirming that the channel under SiN_x is p-type with hole-carriers. It is the evidence that the channel at the SiN_x/diamond interface is preserved, which may be related to the C-N bonds [21]. In addition, the device operates in the normally on depletion mode. An obvious typical output characteristic for both of the FETs could be found in the figure. As the $|V_{GS}|$ increases, $|I_D|$ increases linearly in the linear region, and the drain current ($|I_D|$) becomes saturated in the saturation region. Compared with the output characteristic of the SC-FET, the $|I_D|$ of SD-FET is larger when $|V_{GS}| < 5$ V and gets close at $|V_{GS}| = 5$ V. And the max current density is consistent for both kinds of devices. This interesting phenomenon may be in connection with the interface states where the charges are trapped.

As shown in Figure 4, the transfer and transconductance curves of the two kinds of devices are familiar. Based on the G_m - V_G relationship, the threshold voltage is determined to be 0.75 V for SD-FET and 0.65 V for SC-FET. The transconductance characteristics presented in Figure 4 were measured at $V_{DS} = -10$ V. The maximum G_m is 1.19 mS/mm at $V_{GS} = -2.5$ to -3.5 V and 1.22 mS/mm at $V_{GS} = -3.5$ to -5 V for SC-FET and SD-FET, respectively.

The charge carrier profile can be derived from the room temperature capacitance-voltage (CV) measurements. Figure 5 shows the calculated profile of H-terminated diamond surface as a function of the depth from the metal/diamond interface. The 2DHG is clearly identified to be 6.6 nm underneath the surface of diamond, corresponding to a gate-to-channel capacitance of 0.76 $\mu\text{F}/\text{cm}^2$. The sheet charge density was calculated to be $2.03 \times 10^{13} \text{ cm}^{-2}$ according to the integration of the profile as revealed in Figure 5. Using the sheet resistance of 11.0 k Ω measured by TLM method, the hole mobility was derived to be 28.0 $\text{cm}^2 \cdot \text{V}^{-1} \cdot \text{s}^{-1}$.

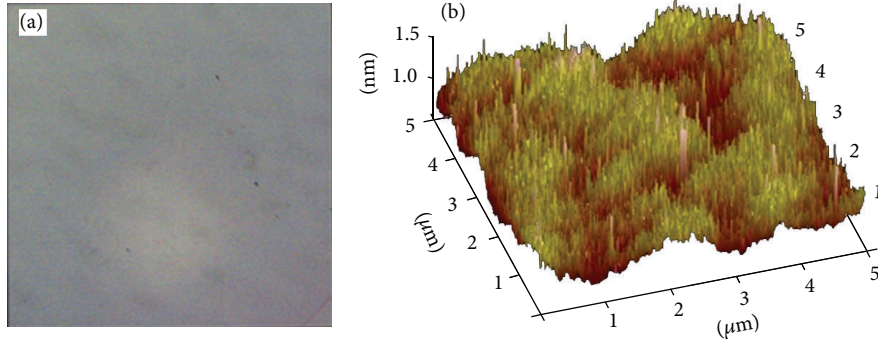


FIGURE 2: The optical microscope image (5x) (a) and AFM photo of MPCVD deposited single crystal diamond epitaxial films.

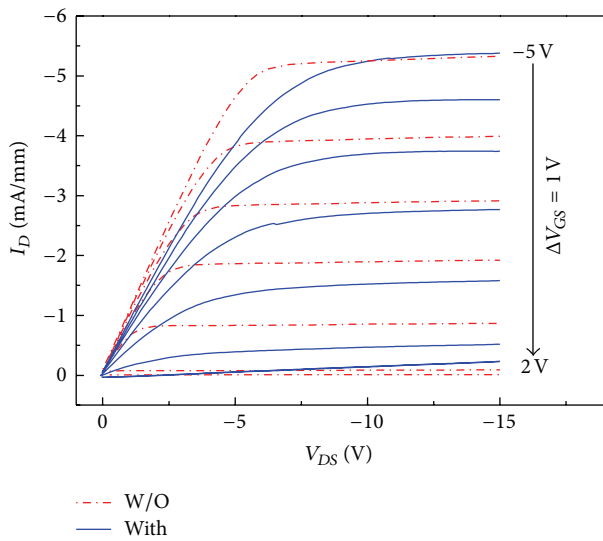


FIGURE 3: FET output characteristics of the Zr-gate diamond based field-effect transistors with and without SiN_x dielectric layers.

Figure 6 exhibits the charge carrier profile of SD-FET with a lower gate-to-channel capacitance of $0.17 \mu\text{F}/\text{cm}^2$, because of the series connection of the intrinsic gate capacitor and the SiN_x gate dielectric capacitor. The permittivity of SiN_x ($\epsilon_{\text{SiN}_x} = 5.0$) and diamond for dielectric layer and gate capacitor were used to evaluate the depth profile. The 2DHG was determined to be 26.2 nm under the interface of $\text{SiN}_x/\text{diamond}$. As the 2DHG of H-terminated diamond located 6.6 nm under the surface, the thickness of SiN_x was estimated to be 19.6 nm , in accordance with nominal thickness of 20 nm . Integration of the charge carrier profile yields a sheet charge concentration of $\rho = 2.17 \times 10^{13} \text{ cm}^{-2}$. Based on sheet resistance of $11.8 \text{ k}\Omega$ and the carrier density, the mobility was extracted to be $24.4 \text{ cm}^2 \cdot \text{V}^{-1} \cdot \text{s}^{-1}$, indicating that it is consistent with that of SC-FET.

The plot of the drain current versus the drain-source voltage up to -200 V is investigated in Figure 7. For SD-FET (Figure 7(a)), $|I_D|$ increases quickly with the voltage increases from 0 V to 50 V and then starts to saturate until the applied voltage gets to -200 V . The max $|I_D|$ was measured to be about

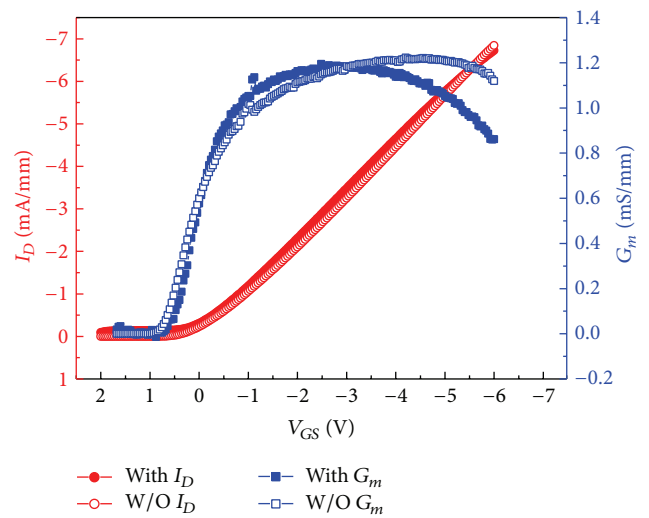


FIGURE 4: The transfer and transconductance of the devices with and without SiN_x layer.

$8 \mu\text{A}$. However, the device does not break down through drain and source; the output and transfer properties are the same as those before applying such high voltage. The relative high drain current may come from the leakage path, which could be related with the defects center at the interface of SiN_x and diamond. The defect centers are something like impurity charges. As the voltage begins to apply, the charges start to move along the direction of the voltage, and the current also increases. When the voltage reaches -50 V , all the charges get involved in the moving, so the current gets saturated. It is worth noting that these charges are out of the control of the gate voltage. The $|I_D|$ of SC-FET (Figure 7(b)) increases slightly with the voltage and gets to 10 nA at -200 V , a very low drain-source leakage, showing a strong control of the Zr-gate metal.

4. Conclusion

In this work, SD-FET has been demonstrated with a 20 nm thick SiN_x dielectric layer on (001) oriented H-termination diamond film. For comparison, a standard SC-FET was also

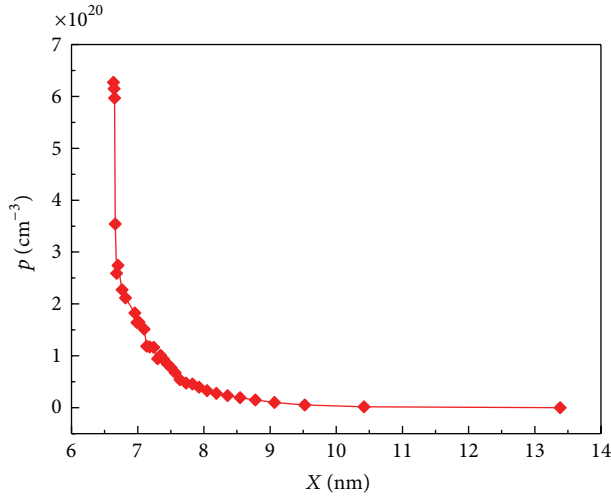


FIGURE 5: Hole-density depth profile in diamond from the H-terminated diamond according to the CGS-VG curve.

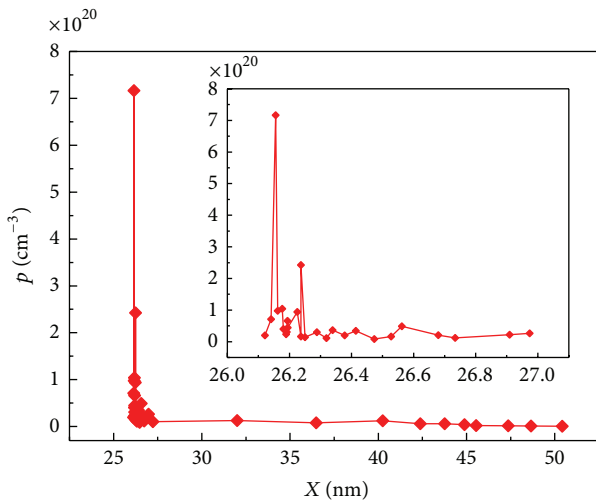
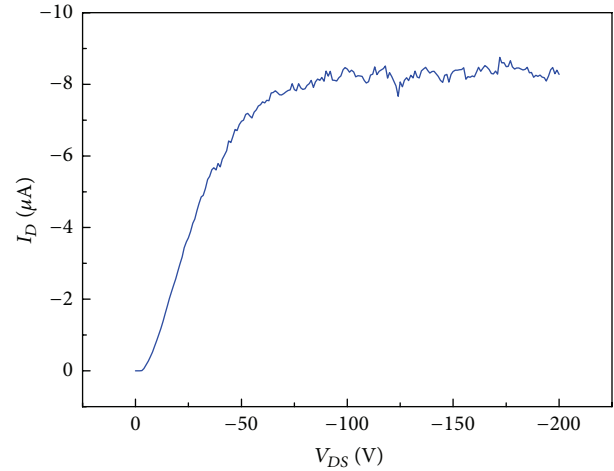


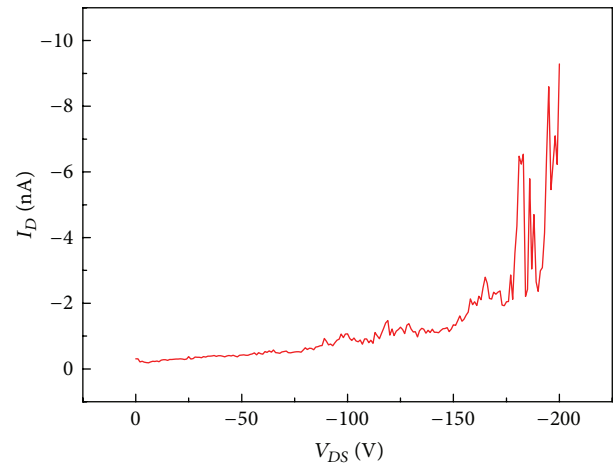
FIGURE 6: Hole-density depth profile in diamond from the SiN_x /diamond interface according to the CGS-VG curve.

fabricated. The transistor output and transfer characteristics of both devices were observed, confirming the presence of the 2DHG at the surface and the interface, respectively. Notably, the maximum drain current of SD-FET was the same compared with SC-FET. The modulated 2DHG sheet charge densities extracted from CV curves were $2.03 \times 10^{13} \text{ cm}^{-2}$ and $2.17 \times 10^{13} \text{ cm}^{-2}$ for SC-FET and SD-FET, respectively. The hole mobility was calculated to be $28 \text{ cm}^2 \cdot \text{V}^{-1} \cdot \text{s}^{-1}$ and $24.4 \text{ cm}^2 \cdot \text{V}^{-1} \cdot \text{s}^{-1}$ for SC-FET and SD-FET, respectively. The cut-off drain current was measured, and no breakdown was presented as the drain-source voltage was applied as high as -200 V . The results indicated that the channels had been preserved after SiN_x deposition. The preserving channel may be related to C-N formation at the SiN_x /diamond interface.



— With SiN_x

(a)



— W/O SiN_x

(b)

FIGURE 7: High voltage of V_{DS} applied on (a) SC-FET and (b) SD-FET at $V_{GS} = 15 \text{ V}$.

Conflict of Interests

The authors declare that there is no conflict of interests regarding the publication of this paper.

References

- [1] S. Koizumi, K. Watanabe, M. Hasegawa, and H. Kanda, "Ultra-violet emission from a diamond pn junction," *Science*, vol. 292, no. 5523, pp. 1899–1901, 2001.
- [2] W. Gajewski, P. Achatz, O. A. Williams et al., "Electronic and optical properties of boron-doped nanocrystalline diamond films," *Physical Review B*, vol. 79, no. 4, Article ID 045206, 2009.
- [3] J. C. Angus and C. C. Hayman, "Low-pressure, metastable growth of diamond and 'diamondlike' phases," *Science*, vol. 241, no. 4868, pp. 913–921, 1988.

- [4] J. Isberg, J. Hammersberg, E. Johansson et al., "High carrier mobility in single-crystal plasma-deposited diamond," *Science*, vol. 297, no. 5587, pp. 1670–1672, 2002.
- [5] J. Walker, "Optical absorption and luminescence in diamond," *Reports on Progress in Physics*, vol. 42, no. 10, pp. 1605–1659, 1979.
- [6] S. A. O. Russell, S. Sharabi, A. Tallaire, and D. A. J. Moran, "Hydrogen-terminated diamond field-effect transistors with cutoff frequency of 53 GHz," *IEEE Electron Device Letters*, vol. 33, no. 10, pp. 1471–1473, 2012.
- [7] K. Ueda, M. Kasu, Y. Yamauchi et al., "Diamond FET using high-quality polycrystalline diamond with f_T of 45 GHz and f_{max} of 120 GHz," *IEEE Electron Device Letters*, vol. 27, no. 7, pp. 570–572, 2006.
- [8] M. Kubovic, M. Kasu, I. Kalfass et al., "Microwave performance evaluation of diamond surface channel FETs," *Diamond and Related Materials*, vol. 13, no. 4–8, pp. 802–807, 2004.
- [9] J. D. Rameau, J. Smedley, E. M. Muller, T. E. Kidd, and P. D. Johnson, "Properties of hydrogen terminated diamond as a photocathode," *Physical Review Letters*, vol. 106, no. 13, Article ID 137602, 2011.
- [10] M. Kasu, K. Ueda, H. Ye, Y. Yamauchi, S. Sasaki, and T. Makimoto, "High RF output power for H-terminated diamond FETs," *Diamond and Related Materials*, vol. 15, no. 4–8, pp. 783–786, 2006.
- [11] K. Hirama, H. Sato, Y. Harada, H. Yamamoto, and M. Kasu, "Diamond field-effect transistors with 1.3 A/mm drain current density by Al_2O_3 passivation layer," *Japanese Journal of Applied Physics*, vol. 51, Article ID 090112, 2012.
- [12] F. Maier, M. Riedel, B. Mantel, J. Ristein, and L. Ley, "Origin of surface conductivity in diamond," *Physical Review Letters*, vol. 85, article 3472, 2000.
- [13] M. W. Geis, "Diamond transistor performance and fabrication," *Proceedings of the IEEE*, vol. 79, no. 5, pp. 669–676, 1991.
- [14] K. Hirama, H. Takayanagi, S. Yamauchi, Y. Jingu, H. Umezawa, and H. Kawarada, "High-performance p-channel diamond MOSFETs with alumina gate insulator," in *Proceedings of the IEEE International Electron Devices Meeting (IEDM '07)*, pp. 873–876, December 2007.
- [15] D. Kueck, P. Leber, A. Schmidt, G. Speranza, and E. Kohn, "AlN as passivation for surface channel FETs on H-terminated diamond," *Diamond and Related Materials*, vol. 19, no. 7–9, pp. 932–935, 2010.
- [16] J. W. Liu, M. Y. Liao, M. Imura, H. Oosato, E. Watanabe, and Y. Koide, "Electrical characteristics of hydrogen-terminated diamond metal-oxide-semiconductor with atomic layer deposited HfO_2 as gate dielectric," *Applied Physics Letters*, vol. 102, no. 11, Article ID 112910, 2013.
- [17] J. W. Liu, M. Y. Liao, M. Imura et al., "Interfacial band configuration and electrical properties of $LaAlO_3/Al_2O_3$ /hydrogenated-diamond metal-oxide-semiconductor field effect transistors," *Journal of Applied Physics*, vol. 114, no. 8, Article ID 084108, 2013.
- [18] J.-W. Liu, M.-Y. Liao, M. Imura, E. Watanabe, H. Oosato, and Y. Koide, "Diamond field effect transistors with a high-dielectric constant Ta_2O_5 as gate material," *Journal of Physics D: Applied Physics*, vol. 47, no. 24, Article ID 245102, 2014.
- [19] J. W. Liu, M. Liao, M. Imura, A. Tanaka, H. Iwai, and Y. Koide, "Low on-resistance diamond field effect transistor with high-k ZrO_2 as dielectric," *Scientific Reports*, vol. 4, article 6395, 2014.
- [20] M. Yokoba, Y. Koide, A. Otsuki, F. Ako, T. Oku, and M. Murakami, "Carrier transport mechanism of Ohmic contact to p-type diamond," *Journal of Applied Physics*, vol. 81, no. 10, pp. 6815–6821, 1997.
- [21] M. Imura, R. Hayakawa, H. Ohsato et al., "Development of AlN/diamond heterojunction field effect transistors," *Diamond and Related Materials*, vol. 24, pp. 206–209, 2012.